

Research

DECOVALEX III/BENCHPAR PROJECTS

**Implications of Thermal-Hydro-Mechanical
Coupling on the Near-Field Safety of
a Nuclear Waste Repository**

Report of BMT1A/WP2

Edited by:

L. Jing

T.S. Nguyen

February 2005

Research

DECOVALEX III/BENCHPAR PROJECTS

Implications of Thermal-Hydro-Mechanical Coupling on the Near-Field Safety of a Nuclear Waste Repository

Report of BMT1A/WP2

Edited by:

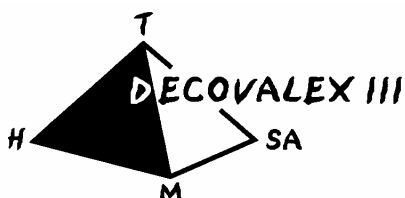
L. Jing¹

T.S. Nguyen²

¹Division of Engineering Geology, Department of Land and Water Resources Engineering, Royal Institute of Technology, Stockholm, Sweden

²Canadian Nuclear Safety Commission, Ottawa, Ontario, Canada

February 2005



SKi

This report concerns a study which has been conducted for the DECOVALEX III/ BENCHPAR Projects. The conclusions and viewpoints presented in the report are those of the author/authors and do not necessarily coincide with those of the SKI.

Foreword

DECOVALEX is an international consortium of governmental agencies associated with the disposal of high-level nuclear waste in a number of countries. The consortium's mission is the DEvelopment of COupled models and their VALidation against EXperiments. Hence the acronym/name DECOVALEX. Currently, agencies from Canada, Finland, France, Germany, Japan, Spain, Switzerland, Sweden, United Kingdom, and the United States are in DECOVALEX. Emplacement of nuclear waste in a repository in geologic media causes a number of physical processes to be intensified in the surrounding rock mass due to the decay heat from the waste. The four main processes of concern are thermal, hydrological, mechanical and chemical. Interactions or coupling between these heat-driven processes must be taken into account in modeling the performance of the repository for such modeling to be meaningful and reliable.

The first DECOVALEX project, begun in 1992 and completed in 1996 was aimed at modeling benchmark problems and validation by laboratory experiments. DECOVALEX II, started in 1996, built on the experience gained in DECOVALEX I by modeling larger tests conducted in the field. DECOVALEX III, started in 1999 following the completion of DECOVALEX II, is organized around four tasks. The FEBEX (Full-scale Engineered Barriers EXperiment) in situ experiment being conducted at the Grimsel site in Switzerland is to be simulated and analyzed in Task 1. Task 2, centered around the Drift Scale Test (DST) at Yucca Mountain in Nevada, USA, has several sub-tasks (Task 2A, Task 2B, Task 2C and Task 2D) to investigate a number of the coupled processes in the DST. Task 3 studies three benchmark problems: a) the effects of thermal-hydrologic-mechanical (THM) coupling on the performance of the near-field of a nuclear waste repository (BMT1); b) the effect of upscaling THM processes on the results of performance assessment (BMT2); and c) the effect of glaciation on rock mass behavior (BMT3). Task 4 is on the direct application of THM coupled process modeling in the performance assessment of nuclear waste repositories in geologic media.

On September 25, 2000 the European Commission (EC) signed a contract of FIKW-CT2000-00066 "BENCHPAR" project with a group of European members of the DECOVALEX III project. The BENCHPAR project stands for 'Benchmark Tests and Guidance on Coupled Processes for Performance Assessment of Nuclear Waste Repositories' and is aimed at improving the understanding to the impact of the thermo-hydro-mechanical (THM) coupled processes on the radioactive waste repository performance and safety assessment. The project has eight principal contractors, all members of the DECOVALEX III project, and four assistant contractors from universities and research organisations. The project is designed to advance the state-of-the-art via five Work Packages (WP). In WP 1 is establishing a technical auditing methodology for overseeing the modeling work. WP's 2-4 are identical with the three bench-mark tests (BMT1 - BMT3) in DECOVALEX III project. A guidance document outlining how to include the THM processes in performance assessment (PA) studies will be developed in WP 5 that explains the issues and the technical methodology, presents the three demonstration PA modeling studies, and provides guidance for inclusion of the THM components in PA modeling.

This report is the final report of the first phase of the BMT1 (called BM1A) of the DECOVALEX III and its counterparts in BENCHPAR, WP2, with studies performed for re-evaluating the numerical modeling of the in-situ THM experiments at the Kamaishi Mine, Japan, during the DECOVALEX II project time, and calibrating the

computer codes applied for the next two phases of BMT1 (called BMT1B and BMT1C, respectively) of the DECOVALEX III and WP2 of BENCHPAR projects.

L. Jing
F. Kautsky
J.-C. Mayor
O. Stephansson
C.-F. Tsang

January 2005

Stockholm, Sweden

Summary

This report presents the works performed for the first phase (BMT1A) of BMT1 of the DECOVALEX III project for the period of 1999-2002.

The works of BMT1 is divided into three phases: BMT1A, BMT1B and BMT1C. The BMT1A concerns with calibration of the computer codes with a reference T-H-M experiment at Kamaishi Mine, Japan. The objective is to validate the numerical approaches, computer codes and material models, so that the teams simulating tools are at a comparable level of maturity and sophistication in order to perform the scoping calculations defined in BMT1B and BMT1C.

Five teams participated in studying BMT1A: CNSC (Canada), JNC (Japan), IRSN/CEA (France), ANDRA/INERIS (France) and SKI/KTH (Sweden), using FEM approach except the INERIS team (Using FDM approach).

A simplified calibration test case of the in-situ experiment was proposed and defined as an axisymmetric model. The case focuses on the THM behaviour along a radial line (with a radial distance r as the coordinate) from the centre of the heater. The desired output parameters are: temperature, radial displacement, pore pressure, water content, the total radial stress and the radial and tangential strains, respectively. Time histories of these output parameters were calculated for both the heating and cooling phases.

A number of improvements to the modelling of the Kamaishi Mine heater test were suggested and tested in this study. Although the model geometry is much simplified compared to the field test conditions, improved simulation of the general THM responses were obtained, as compared with the Task 2C results of DECOVAEX II. The measures taken for improvement were: i) Parameter changes (reduced rock mass permeability and rock mass thermal expansion by the SKI/KTH team, and increased thermal expansion coefficient and reduced swelling pressure constant of the buffer by JNC team); ii) Inclusion of the sealing of rock fractures by penetrating bentonite by the SKI/KTH team, which can explain the uniform (axisymmetric) wetting of the bentonite; iii) An improved swelling/shrinking strain function combined with an increased thermal expansion of the bentonite giving a good match of the mechanical (stress, strain) behavior of the buffer by the KTH/SKI team and iv) Use of higher E (Young's modulus) and ν (Poisson's ratio) of the bentonite near the heater, and use of a "sealed" layer of rock around the bentonite by the CNSC team.

As a results of the above measures, the results from the simplified axisymmetric model used in the re-evaluation of the Kamaishi mine experiment showed general improvement over the original models used in the prediction phase during the DECOVALEX II project. The calculated temperature results agree very well with the experimental values, for all teams. The results of stress and strain behaviour in the bentonite are generally improved, at least qualitatively though, with the measured results. The water content near the heater (at point 1) is relatively well predicted by all teams, although the saturation front at the bentonite/rock interface are still predicted to advance much faster than in reality.

In general, the mechanical behaviour of the buffer is complex with forces contributing from shrinking/swelling in all part of the bentonite, external stress from the thermal expansion of the heater and rock, and internal thermal expansion of the bentonite itself. However, the BMT1A results show that a reasonable prediction of the mechanical behaviour can be done if all relevant bentonite properties are known from laboratory tests.

Content

	<u>Page</u>	
1	Introduction	1
	1.1 Background	1
	1.2 General definition of the problem	2
	1.3 Calibration of the T-H-M experiment	5
	1.4 Scoping calculations for the near-field of a generic repository	8
	1.5 A simplified axisymmetric calibration case of the T-H-M experiment	15
2	Re-evaluation of Kamaishi Mine modelling (by the CNSC team)	17
	2.1 Summary of blind prediction of the Kamaishi THM experiment	17
	2.2 The simplified axisymmetric model	17
	2.3 Summary and conclusions	24
3	Re-evaluation of Kamaishi Mine modelling (by the JNC team)	25
	3.1 Introduction	25
	3.2 Temperature and density dependency of swelling pressure	25
	3.3 Simulation of laboratory experiment by considering The temperature and density dependency	27
	3.4 Re-evaluation of Kamaishi THM experiment	38
	3.5 Summary	45
4	Re-evaluation of Kamaishi Mine modelling (by the KTH team)	46
	4.1 Suggestions for improved modelling of the Kamaishi Mine heater test	46
	4.2 A simplified axisymmetric model of the Kamaishi Mine heater test	50
	4.3 Results of axisymmetric modelling of the heater test	54
	4.4 Comparison of axisymmetric modelling to field observations	55
	4.5 Summary and conclusions of SKI/KTH work	60
5	Evaluation of the Kamaishi Mine modelling by the INERIS team)	62
	5.1 Introduction	62
	5.2 Governing equations	62
	5.3 Results of 1D-axisymmetric model	64
	5.4 Conclusion and remarks	73
6	Evaluation of the Kamaishi Mine modelling (by the CEA team)	74
	6.1 Introduction	74
	6.2 Governing equations	74
	6.3 Modelling data for the BMT1-A exercise	76
	6.4 Results of the axisymmetric modelling of the heater test	80
	6.5 Conclusion	83
7	Comparison and summary of conclusions	84
	7.1 Comparison of results	84
	7.2 Summary of conclusions	87
	References	89

1. Introduction

1.1 Background

The DECOVALEX III project is the third stage of an ongoing international co-operative project to support the development of mathematical models of coupled Thermal (T), Hydrological (H) and Mechanical (M) processes in fractured geological media for potential nuclear fuel waste repositories. During the first stage (May 1992 to March 1995), called DECOVALEX I, the main objective was to develop computer codes for coupled T-H-M processes and their verification against small-scale laboratory or field experiments. In the second stage, called DECOVALEX II, the main objective was to further develop and verify the computer codes developed in DECOVALEX I against two large-scale field tests with multiple prediction-calibration cycles, the pump test at the Sellafield, UK, with a hypothetical shaft excavation and the in-situ THM experiment at the Kamaishi Mine, Japan. The third phase of DECOVALEX project, called DECOVALEX III, is initiated with two main objectives. The first is the further verification of computer codes by simulating two additional large scale in-situ experiments: the FEBEX T-H-M experiment performed in Grimsel, Switzerland, and the drift scale heater test at Yucca Mountain, Nevada, USA. The second objective is to determine the relevance of THM processes on the safety of a repository.

To achieve the second objective of DECOVALEX III project, three benchmark tests (BMT) are proposed to examine the relevance of THM processes to performance and safety assessments: 1) BMT1: the impact of THM processes in the near-field of a hypothetical repository in fractured hard rocks; 2) BMT2: homogenisation and upscaling of hydro-mechanical properties of fractured rocks and their impact on far-field performance and safety assessments; and 3) BMT3: Impact of impact of glaciation process on far-field performance and safety assessments.

On September 25, 2000 the European Commission (EC) signed a contract of FIKW-CT2000-00066 "BENCHPAR" project with a group of European members of the DECOVALEX III project. The BENCHPAR project stands for 'Benchmark Tests and Guidance on Coupled Processes for Performance Assessment of Nuclear Waste Repositories' and is aimed at improving the understanding to the impact of the thermo-hydro-mechanical (THM) coupled processes on the radioactive waste repository performance and safety assessment. The project has eight principal contractors, all members of the DECOVALEX III project, and four assistant contractors from universities and research organisations. Kungl Tekniska Högskolan (KTH) is the coordinator of the BENCHPAR project. The project is designed to advance the state-of-the-art via five Work Packages (WP). In WP 1 is establishing a technical auditing methodology for overseeing the modeling work. WP's 2-4 are identical with the three bench mark tests (BMT1 - BMT3) in DECOVALEX III project. A guidance document outlining how to include the THM processes in performance assessment (PA) studies will be developed in WP 5. The document will explain the issues and the technical methodology, present the three demonstration PA modeling studies, and provide guidance for inclusion of the THM components in PA modeling.

This report is concerned with BMT1 of DECOVALEX III project, which is equivalent to WP2 in BENCHPAR project. In the remaining part of this report, only the name BMT1 is used throughout for simplicity.

In the definition of BMT1, it was proposed that scoping calculations be performed in order to determine how T-H-M processes can influence the flow field, as well as the structural integrity of the geological and engineered barriers in the near-field of a typical repository. To simplify the calculation process and focus on the physics of the problems instead of computational efforts, the geometry of the problem, especially regarding the geometry of the fractures, is greatly simplified to regular fracture geometries. The problem is divided into three phases: BMT1A-calibration of numerical codes and material models according to in-situ heater experiments in Kamaishi Mine, Japan; BMT1B-coping calculations of different coupling mechanisms in continuum rocks, and BMT1C-scoping calculations of different coupling mechanisms with fractured rocks. This report is the final report for BMT1A.

1.2. General definition of the problem

The definition of BMT1 is based on a hypothetical case where one considers the feasibility of constructing a nuclear waste repository in a granitic rock formation at a depth of 1000 m. The problem is not site specific, however, in the definition of the problem, experiences was drawn from the results of in-situ tests performed at real sites, with simplified types of rock and engineered barriers. For example at one experimental site in the Kamaishi Mine, Japan, galleries were excavated down to a depth of 600 m, and a variety of hydraulic and mechanical tests have been performed (see Figure 1.1a). Of particular relevance to the assessment proposed in BMT1 is a T-H-M experiment that replicates the near field behaviour of the rock mass and buffer around a single waste container (Fig. 1.1b). The type of bentonite used in the above experiment and the dimensions of the experimental borehole are comparable with the parameters of the conceptual design.

Assume that the fracture density of the rock mass in this hypothetical case could vary with depth, with a fracture spacing of 0.1 m down to 600 m and 0.5 m at depths greater than 600 m, respectively. Based on the average properties of the rock mass determined from the site investigations, a preliminary design of the repository is proposed as shown in Figure 1.2a (JNC, 2000). The centreline distance between adjacent tunnels is 10 m and the centreline distance between adjacent depository holes for the wastes is 4.44 m. The depth of each depository hole is 4.13 m and the diameter is 2.22 m. The overpack (canister) for radioactive wastes would be emplaced into the depository hole, and a bentonite buffer material would be compacted around the overpack. The details of the depository hole are given in Figure 1.2.b. The tunnels would also be backfilled with a mixture of gravel and clay. The PA analysts may use a Monte Carlo assessment code in order to assess the nuclide transport through the engineered barriers to the surrounding rock and requires feedback on the following key points:

1. What is the temperature evolution in the near-field?
2. How long would it take for the buffer to re-saturate?
3. What are the stresses on the overpack and in the buffer? Will they be structurally

stable?

4. How will the permeability and the flow field of the rock mass in the near-field evolve?
5. Is there a potential for rock mass failure in the near-field?
6. What are the uncertainties related to the answers to the above questions, taking into account the variability in the properties of the rock mass?

In order to address the about points, the research teams will perform T-H-M analyses and adopt the following two-phase strategy, which will contribute to the definition of BMT1:

1. Calibration of the computer codes with a reference T-H-M experiment with realistic rock mass conditions and measured outputs of thermal, hydraulic and mechanical variables: The reference experiment chosen for BMT1 is the Kamaishi in-situ experiment at Kamaishi Mine, Japan, performed at the 550 m-Level gallery at the experimental site, illustrated in Fig.1. The calibration will build confidence in the computer codes. This phase of the study forms the first phase of BMT1, the BMT1A.

2. Use of the calibrated codes to perform scoping calculations of the near-field THM behaviour, of the generic design shown in Fig.2, to calculate specific output data that are relevant to PA/SA analyses (e.g. temperature, stress, permeability change, ...) with sensitivity studies considering mainly the changes of fracture patterns and material properties. These works form the contents of next two phases of BMT1, the BMT1B (without fracture but with changing material properties) and BMT1C (with different fracture patterns, see section 1.4 for more details).

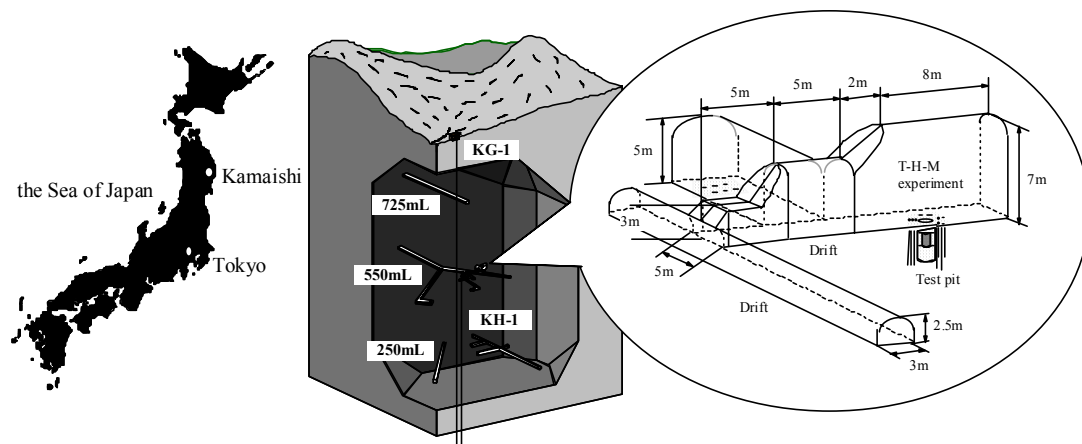
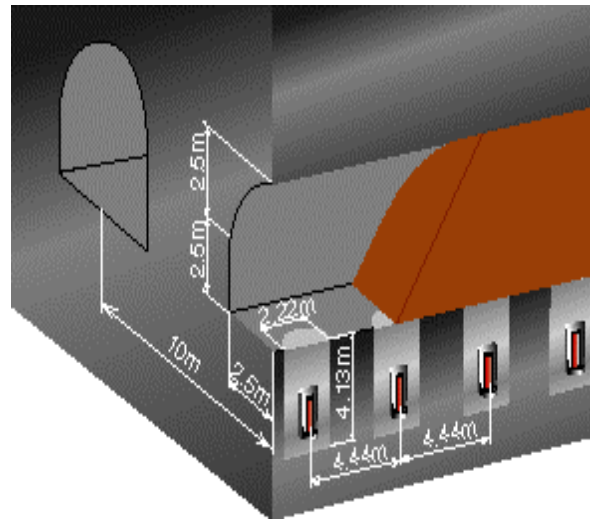
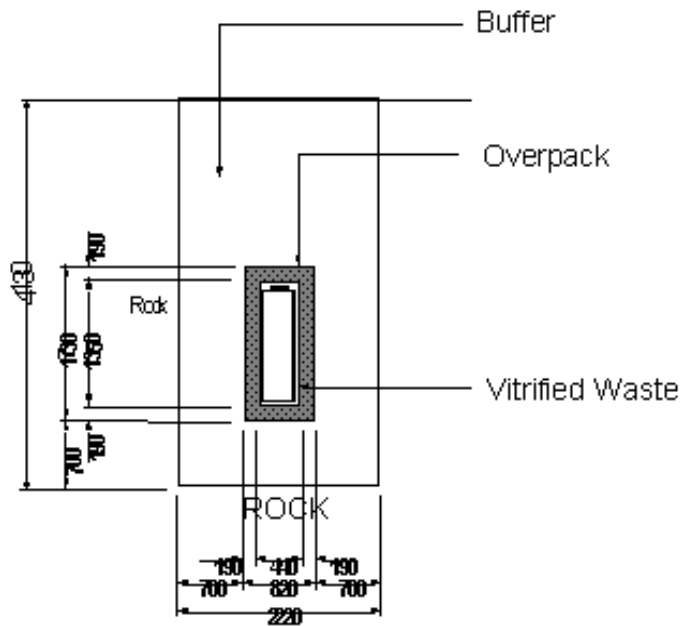


Figure 1.1: Near-field T-H-M experiment with one single heater



a) Typical tunnel-depository hole system



b) Details of borehole

Figure 1.2: Conceptual design of generic nuclear waste repository

1.3. Calibration of T-H-M experiment

1.3.1 General description of the T-H-M experiment

A plan view of the floor of the T-H-M experimental drift in the vicinity of the test hole is shown in Fig. 1.3. A coordinate system has been defined, with the x axis corresponding to the East direction, y axis to the North, and z to the upward vertical direction. The floor is set at $z = -2.357$ m and the coordinates of the centre of the test hole, at the floor elevation, is $(-10.571, -10.356, -2.357)$. Four sets of monitoring boreholes were drilled in the rock mass prior to the excavation of the test hole. Set 1 (KBH1 to KBH6) is used to monitor the pore pressure and temperature in the rock mass; Set 2 (KBM1 to KBM3) is used to monitor strain and temperature in the rock mass; Set 3 (KBM4 and KBM5) is used to monitor deformation of the rock mass; and Set 4 (KBM6 and KBM7) is used to monitor the displacements in the main fractures near and intersecting the test pit.

A granulated bentonite was compacted directly into the borehole, by layers of 10 cm in thickness. The initial water content (by weight) of the bentonite was 15%. A heater was installed in the test pit, within the bentonite. When bentonite was compacted within the last 50 cm of the pit, a concrete lid was installed in the remaining part; this lid was restrained by vertical steel bars connected to the ceiling of the drift, in order to restrict vertical movements. A dam was then built on the floor, and a water pool of 40 cm was created. The temperature of the water pool was maintained at 12.3 °C during the duration of the experiment. The heating phase of the experiment started when the temperature at the centre of the heater was set to 100°C; this heating phase lasted 258 days. The heater was then turned off, and the cooling phase started; measurements from the sensors were recorded during a period of approximately 180 days.

Sensors to measure water content, temperature, pore pressure, stress and strain in the bentonite were installed at 3 sections DDA, BBC and CD (Fig. 1.3).

1.3.2 Properties of the buffer

The basic T-H-M properties of the buffer material are determined by laboratory tests. These properties include: saturated permeability, thermal conductivity, Young's modulus, water retention curves, isothermal infiltration tests, swelling pressure, moisture flow under thermal gradient tests. The details of the tests and the results are given in a separate report. Typical properties are shown in Fig. 1.4 for illustration purposes.

1.3.3 Rock matrix properties

The basic properties of the rock matrix were determined from laboratory tests on intact samples and will be provided in a separate report. Typical values are:

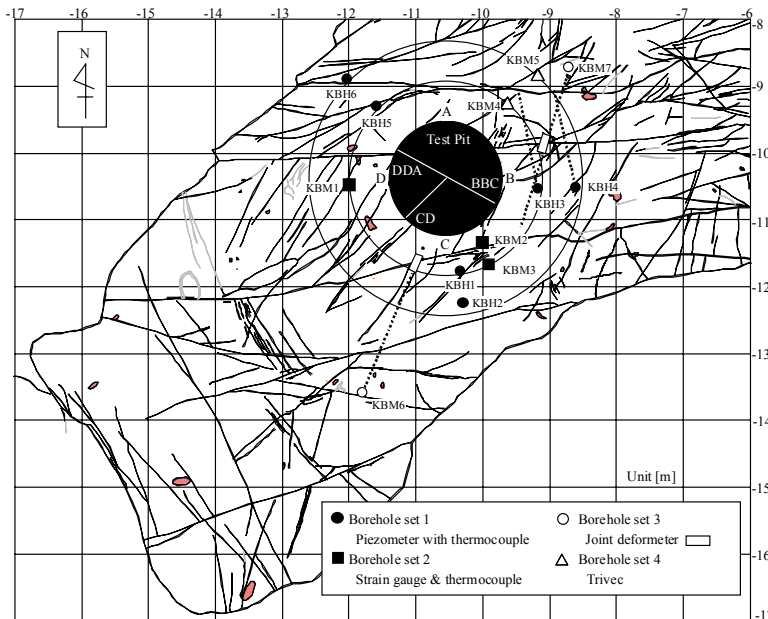


Figure 1.3: Mapped fractures on the floor of the test pit and monitoring boreholes.

Density: $2746 \text{ (kg/m}^3\text{)}$;

Effective porosity: 0.379 (\%) ;

Young's modulus: 61 (GPa) ;

Poisson's ratio: 0.303 ;

Coefficient of linear thermal expansion: $8.21 \times 10^{-6} \text{ (}^\circ\text{C)}$;

Thermal conductivity: $2.54 \text{ to } 2.71 \text{ (W/m}^\circ\text{K)}$ (depends on temperature);

Specific heat: $900 \text{ (J/kg}^\circ\text{K)}$;

hydraulic conductivity: $6.6 \times 10^{-14} \text{ to } 1 \times 10^{-13} \text{ (m/s)}$;

uniaxial compressive strength: 123 (MPa) ;

Tensile strength: 11 (MPa) .

1.3.4 Properties of the heater

The basic properties of the steel overpack are given below:

Density: $7800 \text{ (kg/m}^3\text{)}$;

Young's modulus: 200 (GPa) ;

Poisson's ratio: 0.3 ;

Thermal conductivity: $53 \text{ (W/m}^\circ\text{K)}$;

Specific heat: $0.46 \text{ (kJ/kg}^\circ\text{K)}$;

Coefficient of linear thermal expansion: $(1.64 \times 10^{-6} \text{ }^\circ\text{C}^{-1})$.

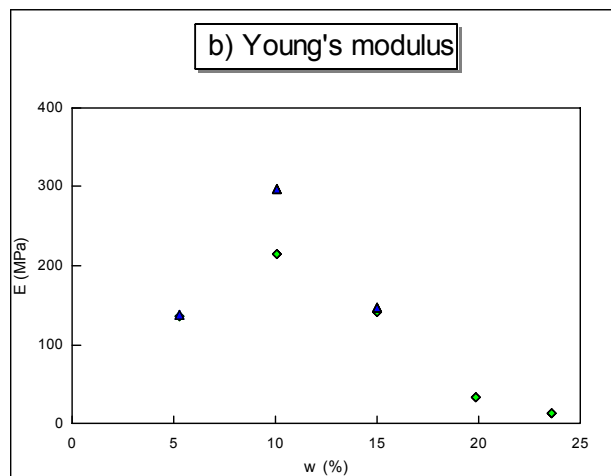
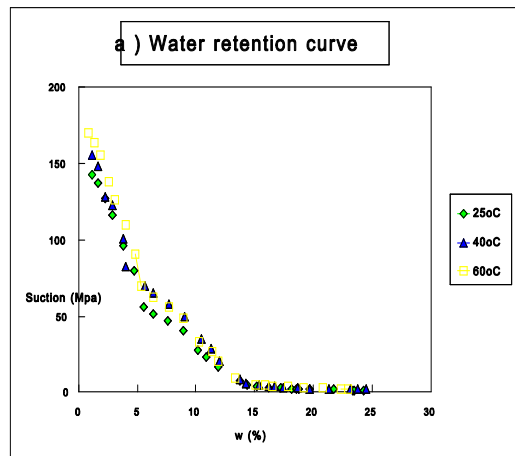
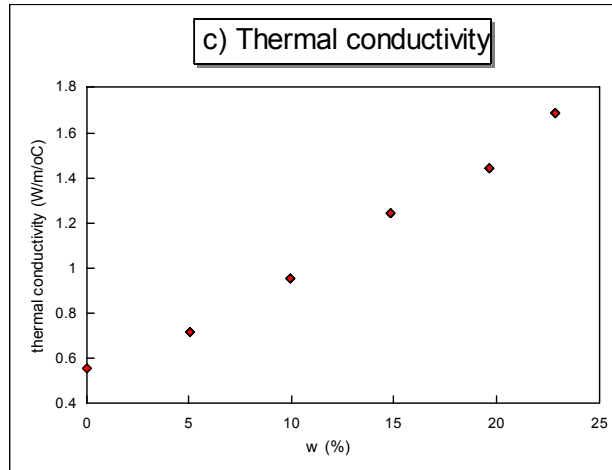


Figure 1.4: Some typical properties of buffer material.

1.3.5 Fracture properties and distribution

Mechanical properties of individual fractures were determined by laboratory tests, on sample of 50 to 95 mm in length. The results, including JRC and JCS, shear strength, shear stiffness are available in a separate report. Typical average values are JRC=8.83; And JCS=105 (MPa).

Detailed mapping of the fractures on the floor and roof of the experimental drift, and on the walls of the test hole is also available, together with the in-situ hydraulic test results in the fractured rock mass. Figure 1.3 also shows the most important fractures on the floor of the experimental area.

1.3.6 Output specifications

The time evolution curves for temperature, displacements, water content, etc. in the buffer and the rock mass at specified monitoring points are requested from each team. The details of the locations of the points with monitoring variables can be seen in Jing et al. (1999). The research teams are required to calibrate their computer codes and computational model with the experimental data. In addition to giving results at the specified points, the results should be evaluated by discussing the following points:

- Specify which input parameters are needed in your model. Determine which ones are available from laboratory and/or field tests, and which ones were assumed, and justify the values actually used in the calibrated model.
- Discuss and justify how the rock-bentonite and bentonite-heater interface was represented
- Discuss how the site of the calibration exercise is applicable to the generic site to be studied in the second phase of BMT1 (e.g. Are the rock mass properties, the degree of fracturing of the rock mass, the bentonite properties, etc. within the range of properties assumed for the generic site?)

1.4 Scoping calculations for the near-field of a generic repository

1.4.1 Model geometry with different fracture systems for scoping calculations

From the conceptual design of the repository (cf. Fig. 1.2), and assuming periodic symmetry, one web of the system, comprising one borehole, and a slice of rock and backfill, is considered. The properties of the rock matrix and overpack are the same as in the calibration exercise. The buffer is a mixture of sand and bentonite; its properties and

the properties of the backfill will be given in separate reports. The model geometry and dimensions are shown in Fig. 1.5a.

The effects of excavation shall be determined by performing a steady-state analysis, with the boundary conditions as illustrated in Figure 1.5b. The output of this analysis consists of contours of temperature, pore pressure, permeability, and factor of safety for rock mass failure at sections $x=0$ and $y=0$.

A transient analysis shall be performed, assuming that the buffer, backfill and heater are emplaced instantaneously at time $t = 0$. The analysis shall be for a period of 200 years. The results from the steady state analysis for excavation effects for temperature, stresses, and pore pressure in the rock mass shall be used as initial conditions. For the buffer and backfill, the initial stresses are assumed to be zero, the initial temperature is 20 °C, and the initial water content is 15 %. The boundary conditions for the transient analysis are shown in Fig. 1.5c.

Parametric studies considering several degree of fracturing of the rock mass are defined by the following scoping fracture models:

- No fracture (Fig. 1.6a) – the BMT1B studies;
- One horizontal fracture in the midplane of the emplacement borehole and one vertical fracture 5 m from the tunnel (Fig. 1.6b)- the BMt1C studies;
- Two sets of regular fractures of spacing of 0.5m (Fig. 1.6c)-optional BMT1C studies.

For BMT1B studies, the following initial rock mass effective permeability will be considered: 10^{-19} , 10^{-18} , 10^{-17} m². The rock mass permeability is assumed to be a function of the effective porosity. This function is derived from experimental data on sparsely fractured rock, with a permeability range of 10^{-19} to 10^{-17} m². The permeability function is shown in Fig. 1.7.

For BMT1C studies, the generation of the fracture will start at position (0,0,0). Each fracture will have the following properties: JRC= 9; JCS = 105 MPa, at a laboratory sample length of 80 mm; initial hydraulic aperture: 10 μm. The rock matrix will have the properties for intact rock defined in section 1.3.3.

The heat output from the waste is shown in Figure 1.8 and given in also tabular form in Appendix 1.

1.4.2 Output specifications for buffer and backfill

Time histories of temperature, water content and stresses in the buffer at the output points shown in Fig. 1.9 and Table 1.1 will be calculated. The time history of the vertical displacement at B1 shall also be calculated.

The contours of temperature and water content in the buffer and backfill, at sections $x=0$ and $y=0$ shall be plotted at times: 1, 2, 4, 8, 16, 32, 64, 128, and 200 years.

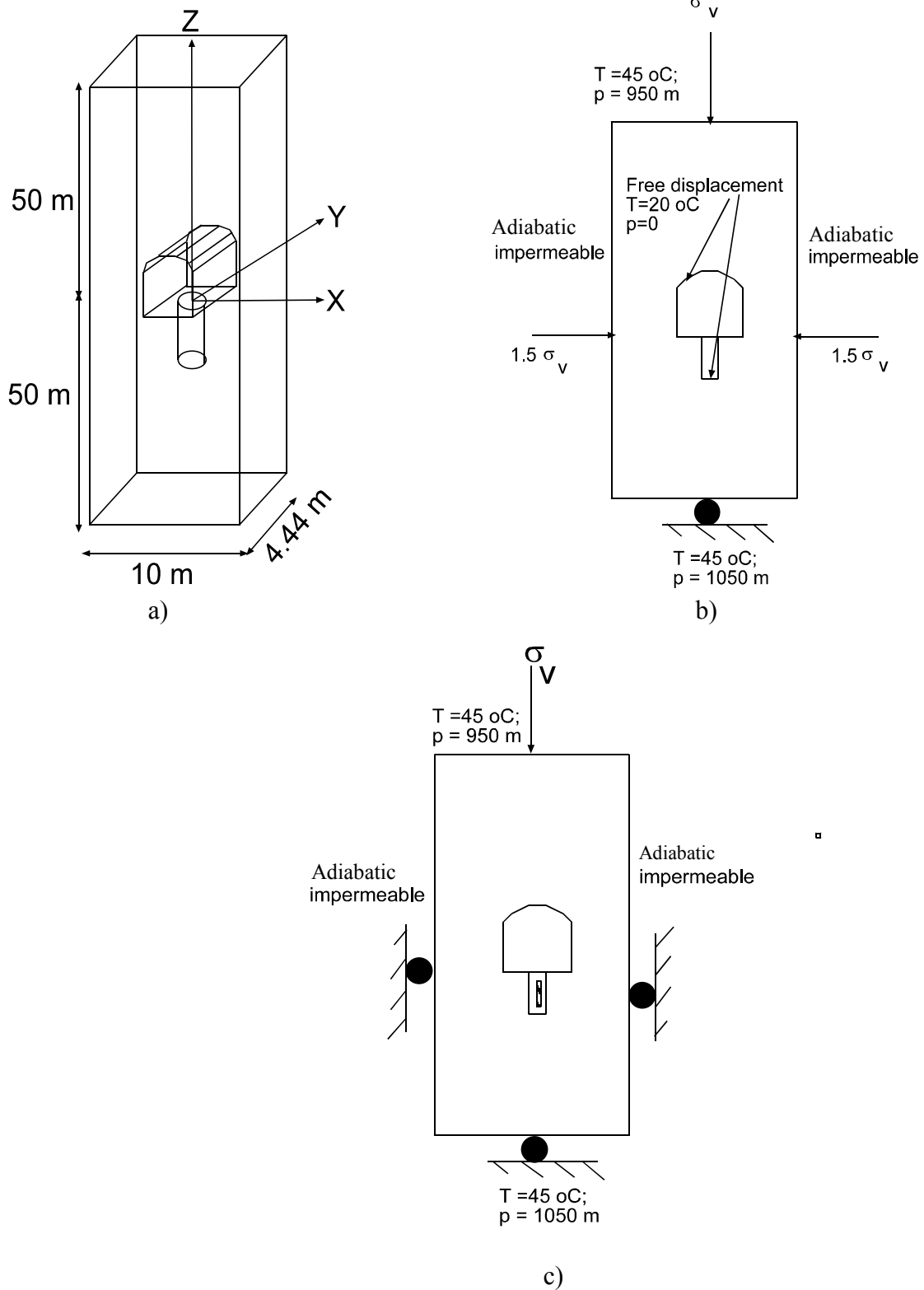


Figure 1.5: Geometry model for near-field scoping calculations a) and boundary conditions for the excavation effect simulation b) and transient analyses c).

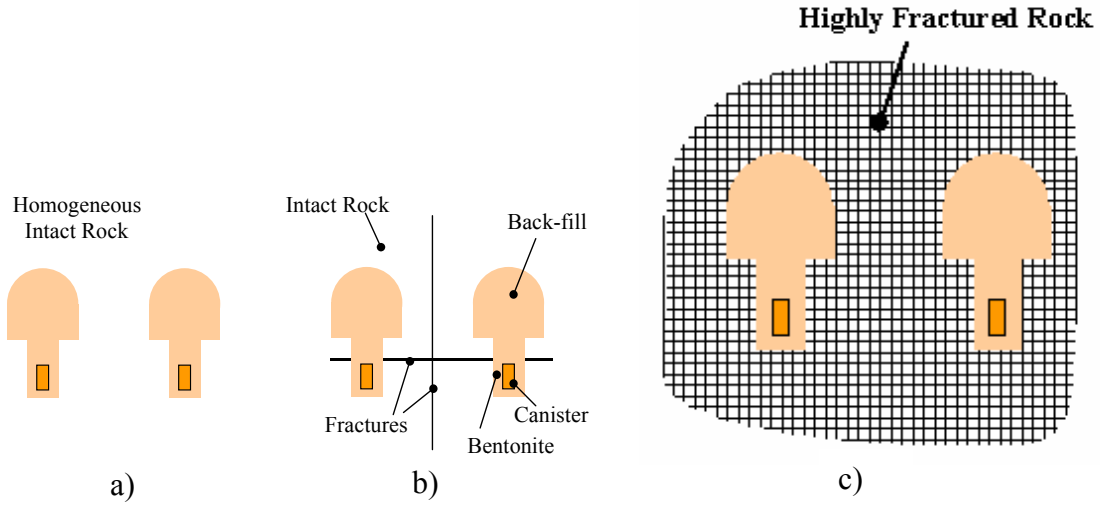


Figure 1.6: Geometry of alternative fracture models.

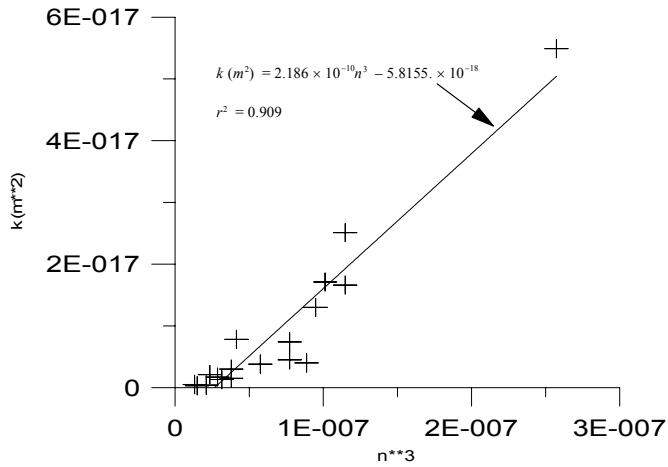


Figure 1.7: Permeability as a function of effective porosity

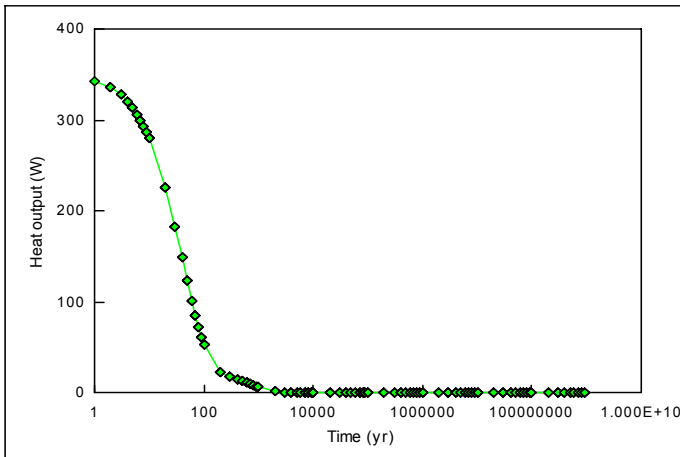


Figure 1.8: Heat output from the waste

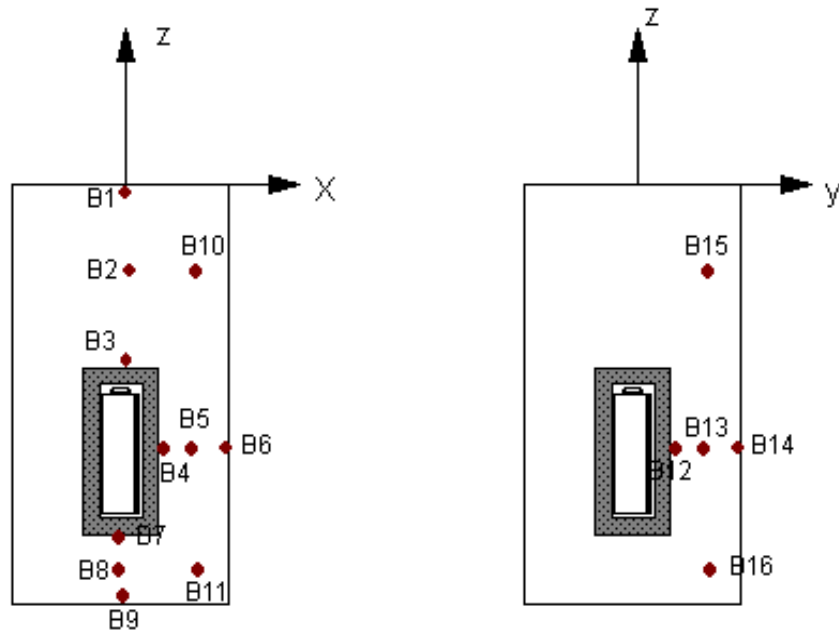


Figure 1.9: Output points for buffer

1.4.3 Output specifications for rock mass

Contours at sections: $x=0$ and $y=0$ and variations along monitoring lines: $x=y=0$; $z=-0.41$ & $x=0$; $z=-0.41$ & $y=0$ will be plotted at times 1, 2, 4, 8, 16, 32, 64, 128, and 200 years for the following output parameters: i) temperature and pore pressure; ii) Factor of safety for rock mass failure; and iii) Permeability.

1.4.4 Evaluation of coupling effects

For both the excavation phase, and the long term phase with emplaced buffer, backfill and heater, the analyses shall be performed with increasing degree of complexity of coupling. A comparison matrix will be established in order to compare the implications of various orders of complexity of the coupling, as shown in Table 1.2.

1.4.5 Rock mass failure criterion

The Hoek-Brown failure criterion is adopted to estimate the rock mass strength behaviour for BMT1, and is expressed in effective stress as

$$\sigma_1' = \sigma_3' + \sqrt{m\sigma_c\sigma_3' + s\sigma_c^2} \quad (1.1)$$

Table 1.1: Output points for buffer

Point	x (m)	y (m)	z (m)	Output values
B1	0	0	0	T, θ , σ_{zz} , u_z
B2	0	0	-0.85	T, θ , σ_{xx} , σ_{zz}
B3	0	0	-1.7	T, θ , σ_{xx} , σ_{zz}
B4	0.41	0	-2.665	T, θ , σ_{xx}
B5	0.76	0	-2.655	T, θ , σ_{xx} , σ_{zz}
B6	1.11	0	-2.655	T, θ , σ_{xx}
B7	0	0	-3.43	T, θ , σ_{zz}
B8	0	0	-3.78	T, θ , σ_{xx} , σ_{zz}
B9	0	0	-4.13	T, θ , σ_{zz}
B10	0.76	0	-0.85	T, θ , σ_{xx} , σ_{zz}
B11	0.76	0	-3.78	T, θ , σ_{xx} , σ_{zz}
B12	0	0.41	-2.665	T, θ , σ_{yy}
B13	0	0.76	-2.655	T, θ , σ_{xx} , σ_{zz}
B14	0	1.11	-2.655	T, θ , σ_{yy}
B15	0	0.76	-0.85	T, θ , σ_{xx} , σ_{zz}
B16	0	0.76	-3.78	T, θ , σ_{xx} , σ_{zz}

Table 1.2: Comparison matrix of for different degree of THM coupling

Output \	T	M	H	H-M	T-H	T-M	T-H-M
T-evolution	Y	N/A	N/A	N/A	Y	Y	Y
σ -evolution	N/A	Y	N/A	Y	N/A	Y	Y
k-evolution	N/A	N/A	N/A	Y	Y	N/A	Y
p-evolution	N/A	N/A	Y	Y	Y	N/A	Y
θ -evolution	N/A	Y	Y	Y	Y	N/A	Y

(T-temperature; σ -stress; k-permeability; p-pressure; and θ -water content).

where σ'_1 and σ'_3 are the major and minor effective principal stresses at failure when equation (1.1) is satisfied, and the effective stress components are defined through

$$\sigma'_{ij} = \sigma_{ij} - p\delta_{ij} \quad (1.2)$$

The symbol σ_c is the uniaxial compressive strength of the rock (=123 MPa), and parameters m and s are the empirical constants, with $m=17.5$ and $s = 0.19$, respectively.

1.4.6 Interfaces between buffer/rock mass, backfill/rock mass and overpack/buffer

It is difficult to provide standard models for the interfaces between buffer and rock, between backfill and rock and between overpack(heater) and rock, mainly due to lack of existing models and available supporting data. The research teams shall therefore define their own assumptions for the nature of these interfaces, from the experience gained in the calibration of the T-H-M test previously discussed.

1.4.7 Uncertainty evaluation

Since the buffer and backfill are man-made materials, it is assumed in this exercise that their properties could be considered constant. The most important degree of uncertainty would be related to the characteristics of the rock mass, e.g. the matrix permeability, the rock mass equivalent permeability, the fracture density and possibly orientation. It is hoped that the consideration of different cases in this exercise (BMT1B and BMT1C) would serve to span a wide span of rock mass characteristics. For example, F0 would constitute a case where no distinctive fracture need to be explicitly included, and the rock mass could be considered as an equivalent porous medium with a range of permeability from 10^{-19} to 10^{-17} m². F1 would constitute a scenario where one important fracture crosses the borehole, and F2 and F3 would constitute the scenario with ubiquitous fractures. The last task of this BMT1 would be a synthesis of all output results from F1 to F4, where the RTs should compare safety features (i.e. temperature field, time for resaturation, stress field, permeability change, potential for rock mass failure) between cases F0 to F5. The other source of uncertainty might be the way the interfaces between the buffer/rock mass, backfill/rockmass and overpack/buffer are considered in the model. The RTs should discuss the influence of these interfaces on their results.

1.5 A Simplified axisymmetric calibration case of the T-H-M in-situ experiment at Kamaishi Mine – case definition of BMT1A

Previous experiences with Task 2 in DECOVALEX II shows that the physics in BMT1 is quite complex and a simple calibration test case with a much simplified problem geometry, but including all relevant physical processes might be helpful to understand the interactions between physical processes, especially the effects of mechanical deformation. For this purpose, a simplified calibration test case was proposed and defined below. The case focuses on the THM behaviour of one radial line from the centre of the heater, with the axisymmetric geometry shown in Fig. 1.10.

The desired output at 5 points, shown in the figure is detailed in Table 1.3. Time histories of these output parameters are requested for a heating period of 258 days followed by a cooling period of 180 days.

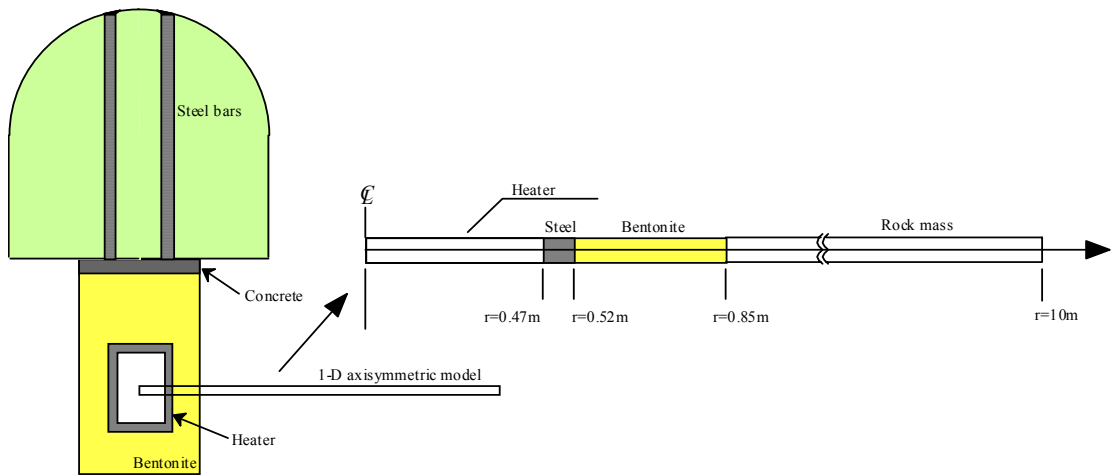


Figure 1.10: Geometry of the simplified axisymmetric model.

Table 1.3: Output variables and locations for the simplified axisymmetric model

Point	r (m)	Output
1	0.52	$T, u, \sigma, \epsilon_r, w$
2	0.685	$T, u, \sigma, \epsilon_r, w$
3	0.85	$T, u, \sigma, \epsilon_r, w$
4	1.45	$T, u, p, \epsilon_r, \epsilon_t$
5	3.	T, u, p

The units of the variables are: T- temperature ($^{\circ}\text{C}$), u- radial displacement (m), p- pore pressure (Pa), w- water content by weight (%), σ - radial total stress (Pa) and ε_r , ε_t - radial and tangential strain (non-dimensional).

The boundary conditions are as follows:

At $r = 0.47$ m:

- $T=100$ $^{\circ}\text{C}$ (during heating) and free temperature (during cooling)
- Free displacement
- Impermeable

At $r = 10$ m:

- $T = 12$ $^{\circ}\text{C}$
- $u=0$
- $p=3.9$ kPa (equivalent to 0.4 m of water)

The initial conditions are as follows:

- $T = 12$ $^{\circ}\text{C}$ everywhere
- The displacements and stresses are zero everywhere
- $p = 3.9$ kPa in the rock; $w = 15\%$ in the bentonite

The basic T-H-M properties of the bentonite are determined by laboratory tests by JNC (1997). Depending on the models, input properties additional to the ones determined in the laboratory might be needed. These additional properties were determined by performing calibration of laboratory tests performed in Task 2C, of DECOVALEX II (Jing et al., 1999). For this test case, the input properties should be selected from these two sources, especially the Table 5.1 in Jing et al. (1999), which summarizes the most important input parameters and should be used as a starting point.

The following experimental values should be used as calibration targets: temperature and water content at points 1, 2 and 3; radial stresses at points 1 and 3; radial strain at point 2 and radial and tangential strain at point 4. These experimental data came from the recorded results of different sensors at the same radial distance, but at different tangential angles. In addition, tensile stress measurements may or may not be reliable and care should be taken in using them.

This report presents the works performed for BMT1-A. The authors of the chapters are: T. S. Nguyen (Chapter 2), M. Chijimatsu and Y. Sugita (Chapter 3), J. Rutqvist (Chapter 4), A. Thoraval, M. Souley and A. Giraud (Chapter 5), A. Millard and A. Rejeb (Chapter 6), T. S. Nguyen and L. Jing (Chapters 1 and 7).

2. Re-evaluation of the Kamaishi mine modelling- The CNSC team studies

In this chapter, the works performed by the CNSC (formerly AECB) team on the first phase of BMT1 is presented. The objective of this first phase is to increase the confidence in the modelling tool, the FRACON finite element code. The FRACON code will be also be used for scoping calculations latter phases of BMT1, looking at safety issues related to THM processes in the near-field. The strategy to increase this confidence is to obtain a better understanding of the physical processes that actually prevailed during the in-situ THM experiment performed a the Kamaishi mine in Japan. Blind prediction of the experiment was performed by the CNSC team (Nguyen, 1999; Nguyen, 2000 a and b) during DECOVALEX II. The chapter will first summarize the results of the former work, pointing out the agreement, or lack of it, between predictions and experimental results; discuss possible explanations for the disagreements; and finally present the results of a new analysis in an attempt to reconcile the differences.

2.1 Summary of blind prediction of the Kamaishi THM experiment

As part of DECOVALEX II project, the FRACON code was used to perform blind predictions of the experiment. An axisymmetric model was used in DECOVALEX II (Fig. 2.1). The degree of agreement between the predictions and the experimental results could be summarized as follows:

- Temperatures are very well predicted in both the bentonite and the rock mass (Fig. 2.2)
- The water content in the bentonite are well predicted (Fig. 2.3). At the rock/bentonite interface, the model predicts a faster resaturation than the experimental data. It was believed that this is due swelling of the bentonite that in turns creates a sealing effect at the interface.
- The total stresses in the bentonite are well predicted at the rock/bentonite interface; these stresses were overpredicted near the heater (Fig. 2.4). It was believed then that this overprediction is due to the assumption of an infinitely rigid heater.
- The displacements in the rock were reasonably well predicted (Fig. 2.5).
- The pore pressure in the rock mass, induced by the thermal pulse, was predicted to be insignificant. The experimental data did show some small effects. It was believed that this is due to the coarseness of the mesh used in the finite element model.

2.2 The simplified axi-symmetric model

In order to test the adequacy of the hypotheses formulated in section 2.1, with respect to the lack of agreement between predicted and experimental results, a re-evaluated

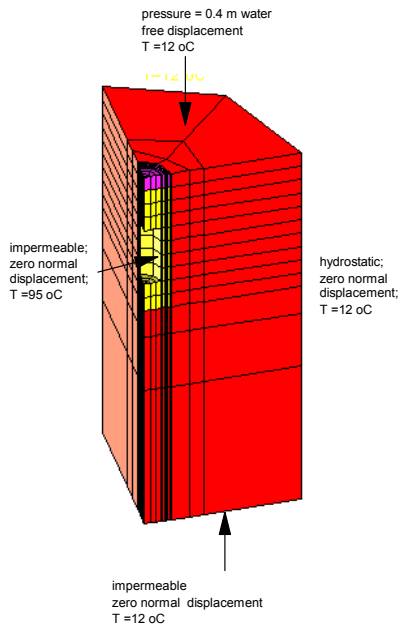
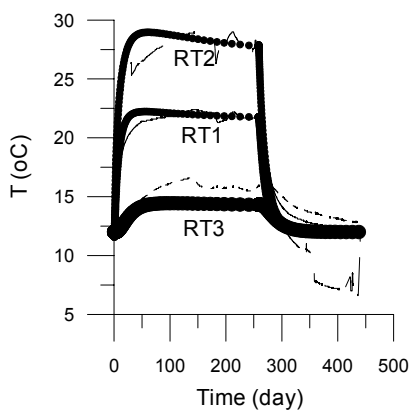
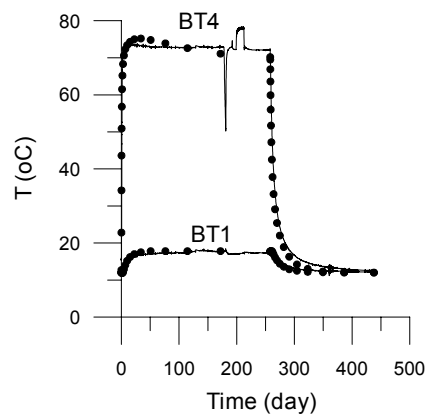


Figure 2.1: CNSC (formerly AECB) finite element model for prediction of Kamaishi Mine THM experiment in DECOVALEX II

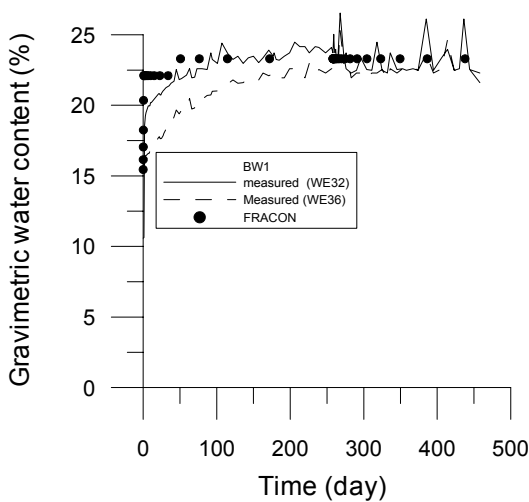


a) temperature in bentonite

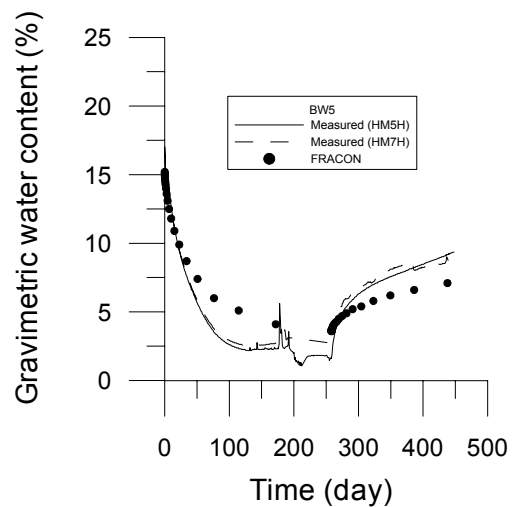


b) temperature in rock

Figure 2.2: Temperature evolution (dots are predicted values) - DECOVALEX II

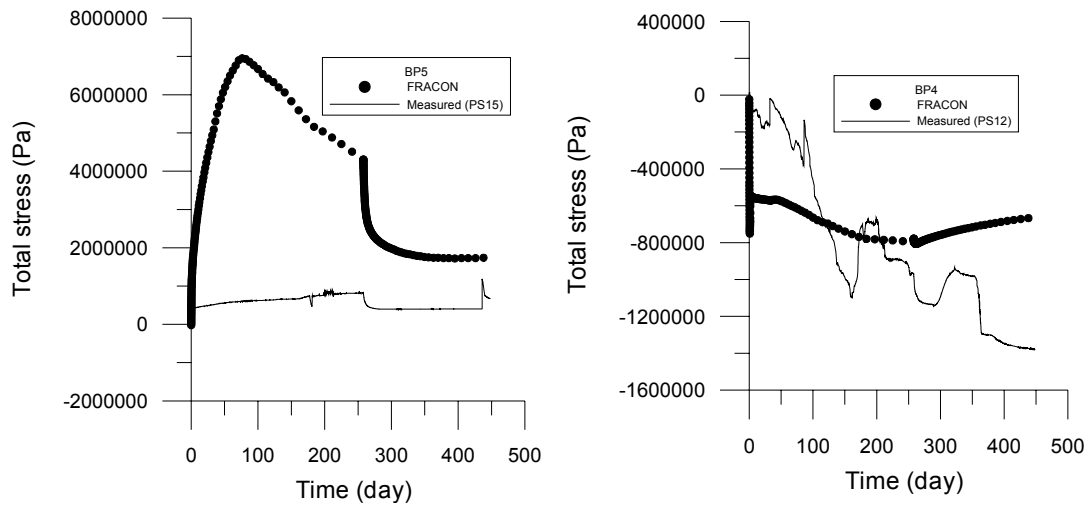


a) Water content near heater



b) water content at bentonite/rock interface

Figure 2.3: Water content evolution (dots are predicted values) - DECOVALEX II



a) stresses at buffer/rock interface b) stresses near heater
Figure 2.4: Evolution of total stress in bentonite - DECOVALEX II

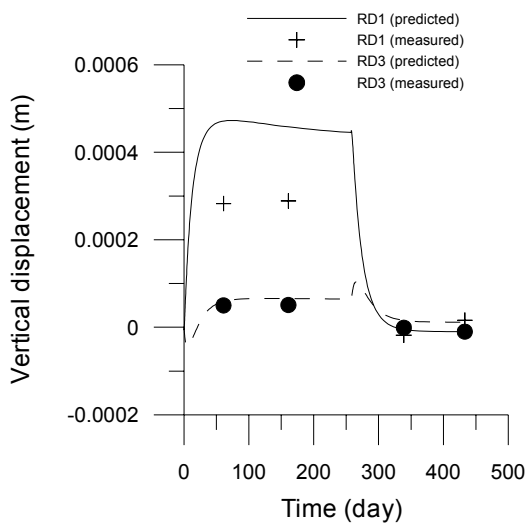


Figure 2.5: Displacement in rock mass - DECOVALEX II

conceptual model was formulated by the CNSC team, as the simplified axisymmetric model defined in Chapter 1. The attention is focussed on one line of radial symmetry running through the centre of the heater (cf. Fig. 1.11); consequently a thin layer of material running through this line is considered in the finite element model (Fig. 2.6). The finite element model is actually a quarter of a thin cylinder. Using symmetry arguments, the bottom, top, $x=0$ and $y=0$ boundaries are assumed to be adiabatic, impermeable and with zero normal displacements. A constant temperature of $100\text{ }^{\circ}\text{C}$ was imposed on the left boundary, as dictated by the set temperature in the centre of the heater, during the heating phase of 258 days. The above thermal constraints were released during the subsequent cooling period of 180 days. A constant water pressure of 3.9 KPa (corresponding to a height of 0.4 m of water imposed on the floor of the experimental drift) was imposed on the right boundary, situated at a radial distance of 3 m. Zero normal displacement was also imposed at the right boundary. The whole system

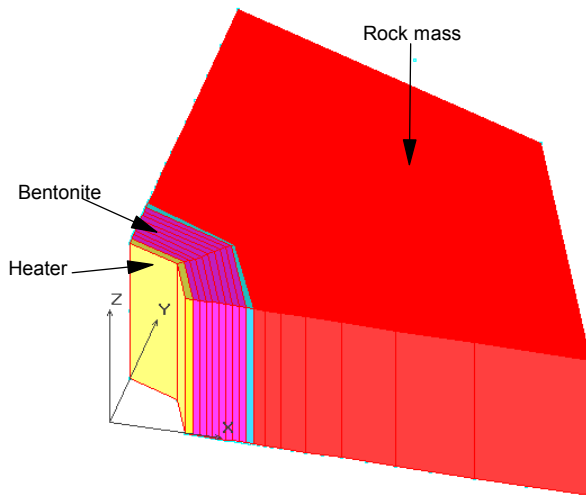


Figure 2.6: Finite element for the simplified axisymmetric model

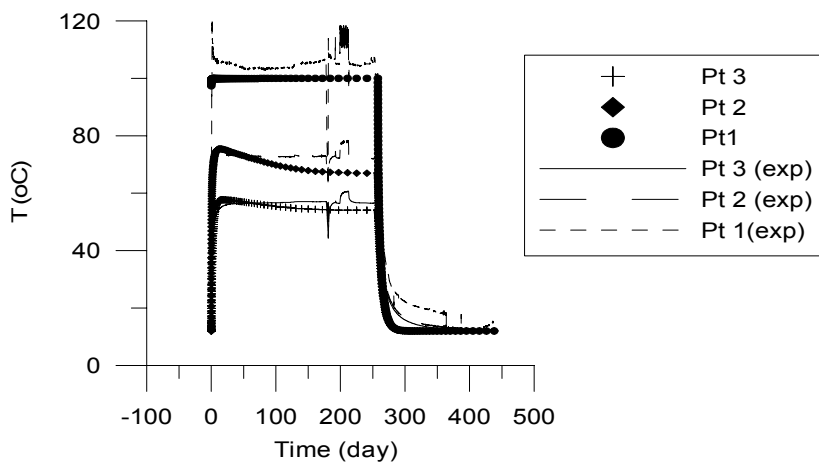


Figure 2.7: Temperature in bentonite.

was initially set at a temperature of 12 °C. In order to match the measured temperature, it was assumed that all nodes from a radial distance of 2.27 m to 3 m remained at a constant temperature of 12 °C.

The input properties of the bentonite and the rock mass remains the same, except for the following:

- A “stiffer” bentonite with a Young’s modulus of 150 MPa as compared to 50 MPa. Near the heater, within an annulus of 4 cm in thickness, the Poisson’s ratio was also increased from 0.4 to 0.484. This adjustment was necessary in order to decrease the predicted value of the stresses to levels consistent with the measured values.
- The heater was included in the model, with the following input properties: Young’s modulus 200 GPa and Poisson’s ratio: 0.4.

The results for temperature in the bentonite are shown in Fig. 2.7. Except for some numerical dispersion in the calculated values (existence of an artificial peak temperature during the heating phase), very good agreement is obtained between calculated and measured temperatures.

The water content evolution in the bentonite is shown in Fig. 2.8. Good agreement is

obtained near the heater. Reasonably good agreement is obtained at the rock/bentonite interface. The resaturation predicted by FRACON occurs much faster (4 days) than indicated by the measured data (100 days), even with the introduction of a thin layer of rock (2 cm), with permeability values which are intermediate between the bentonite and the remaining rock mass. It is possible that the rock was initially unsaturated. The calculated water content does not compare well with the measured values for point 2; this might be due to the inability of the FRACON code to take into account condensation/evaporation processes.

The total radial stress at point 1, near the heater, is shown in Fig. 2.9. Good agreement is also obtained between calculated and measured results. Stresses are shown to be mostly compressive (positive values).

The evolution of total radial stress at point 3, at the bentonite/rock interface is shown in Fig. 2.10. Reasonably good agreement is obtained; the stresses seem to be mostly tensile (negative values). At cooling, the calculated stress shows a reversal in the variation trends while this was not evident from the experimental results.

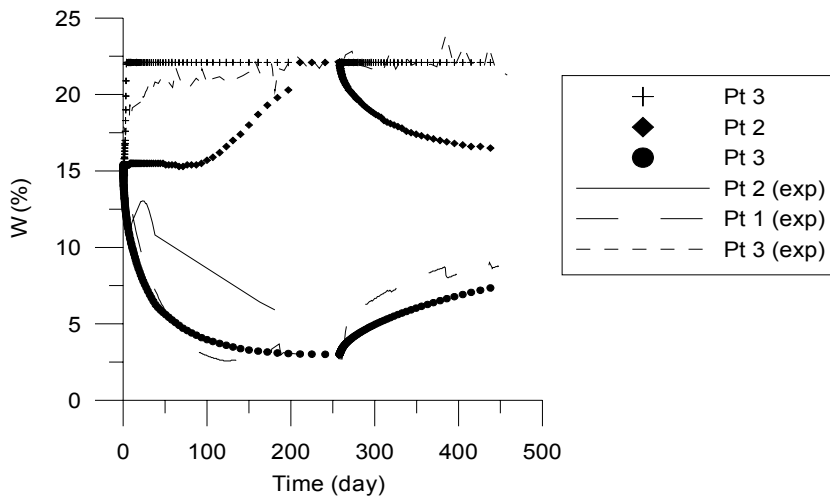


Figure 2.8:
Evolution of
water content
in bentonite

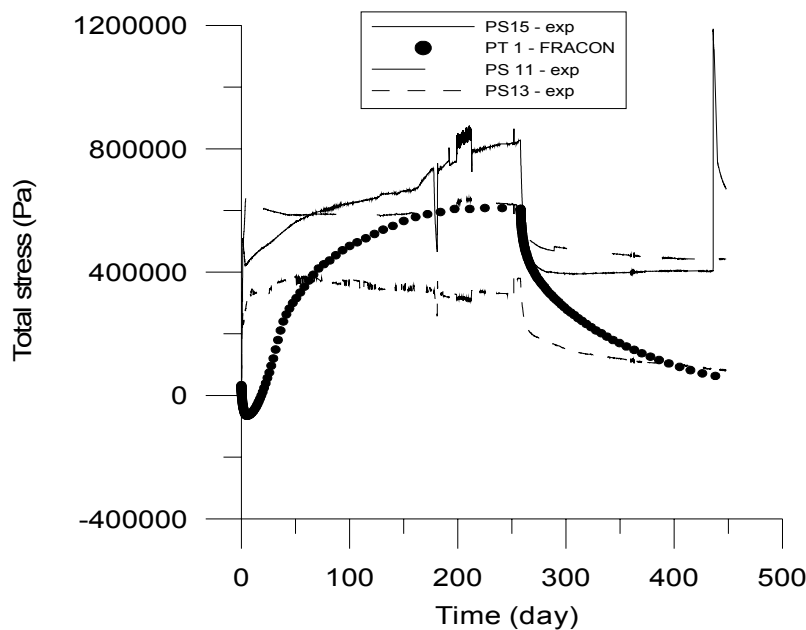


Figure 2.9:
Total radial
stress at
point 1,
near heater

The evolution of radial strain at point 2 in the bentonite, midway between the heater and the rock, is shown in Fig. 2.11. Tensile strain (negative values) are predicted. The predicted values agree well with the measured ones, if a sign reversal is brought to the latter (according to JNC, the measured strain are compressive). The calculated radial displacements at points 1, 2 and 3 in the bentonite are shown in Fig. 2.12, where positive values denote outward movements. Points 1 and 3 are predicted to move outward due to thermal expansion, while point 2 would move inward, due to swelling of the bentonite caused by wetting (increase in water content).

The temperature, radial displacement, pore pressure, and strain at point 4 in the rock are shown in Figs. 2.13 - 2.16, respectively. In Fig. 2.15, a thermally induced pressure pulse is predicted by the FRACON code. This pulse is of very short duration, since the rock is relatively permeable. The axial strain are calculated to be tensile and follows the same trends as the measured strain; however the calculated axial strain is about one order of magnitude lower than the measured strain. The calculated tangential strain, contrarily to the measured strain, is also tensile. These discrepancies are likely due to the prescribed fixed boundary condition at a radius of 3 m; the right boundary of the finite element model (cf. Fig. 2.6) should be extended to farther distances.

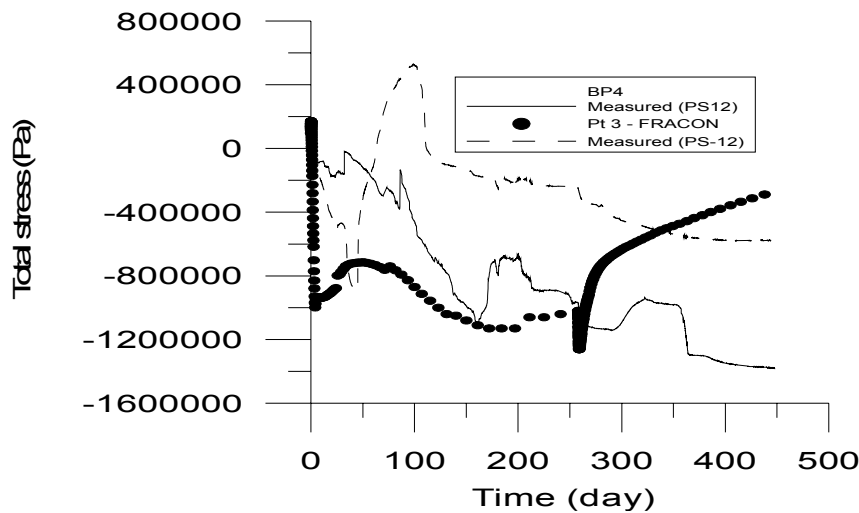


Figure 2.10:
Evolution of
total radial
stress at
point 3
(bentonite/ro
ck interface)

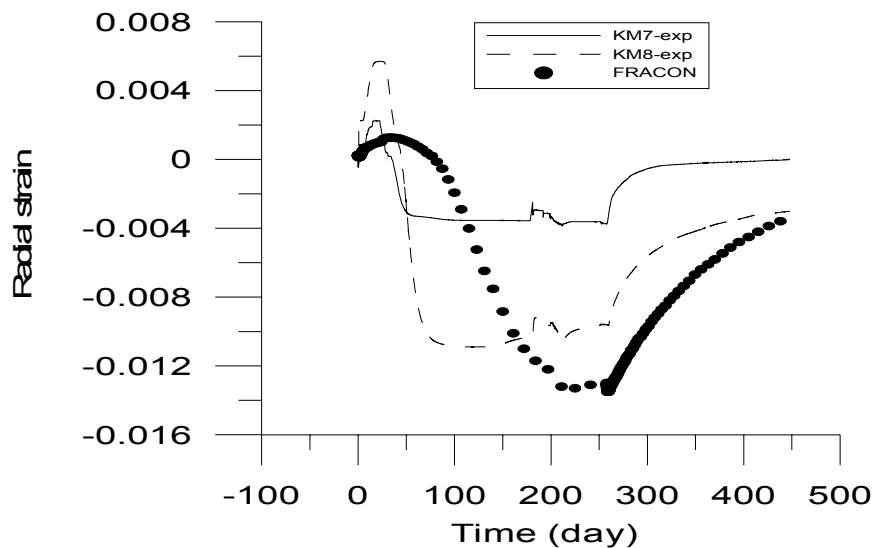


Figure 2.11:
Evolution of
radial strain
in buffer at
point 2
(midway
between
heater and
rock)

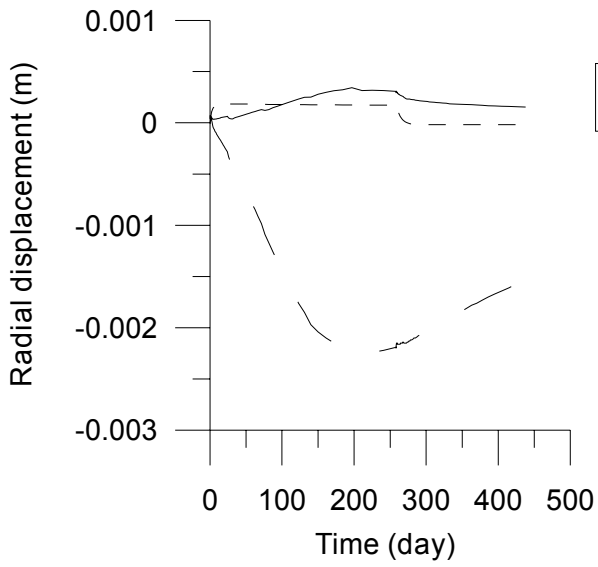


Figure 2.12: Radial displacement in bentonite.

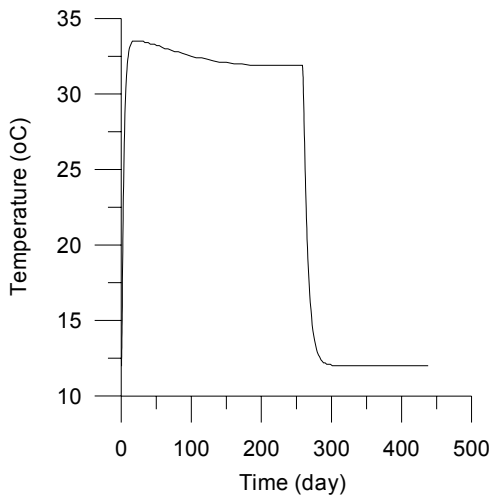


Figure 2.13: Calculated temperature at point 4 in rock mass

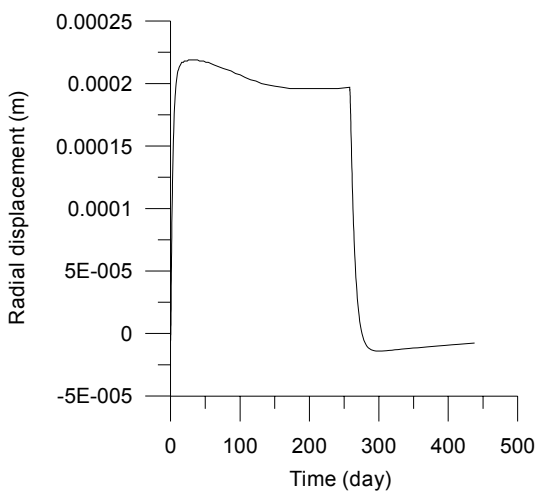
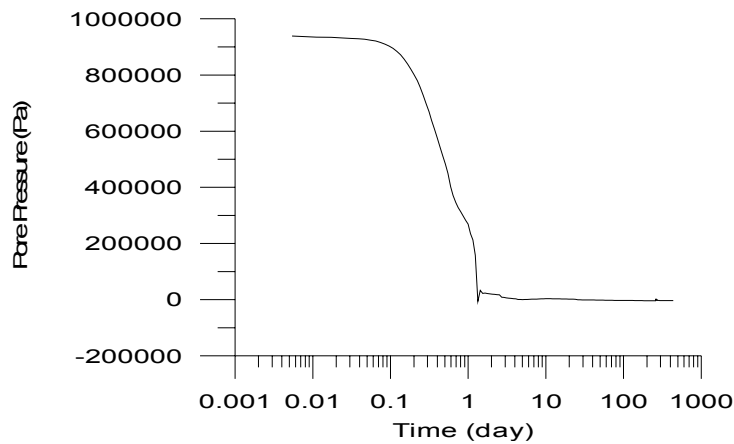
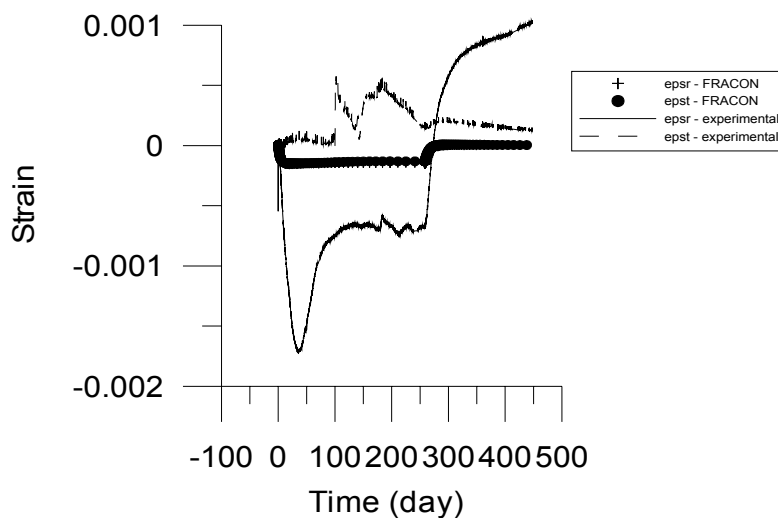


Figure 2.14: Calculated radial displacement in rock mass



*Figure 2.15:
Calculated
pore
pressure at
point 4 in
rock mass*



*Figure 2.16
Strain at point
4 in rock mass*

2.3 Summary and conclusion

The results from the “one-dimensional” axisymmetric model used in the re-evaluation of the Kamaishi mine experiment showed general improvement over the “2-dimensional” axisymmetric model used in the prediction phase:

- ❑ As before, calculated values of temperature agree very well with the experimental values
- ❑ By defining a “stiffer” bentonite, the calculated stress and strain in the bentonite agree well with the experimental values.
- ❑ The water content near the heater are well predicted. The saturation front at the bentonite/rock interface are still predicted to advance much faster than in reality, even with the use of a low permeability rock layer at this interface. It is possible that an unsaturated rock layer exists around the bentonite. The calculated water content in the bentonite does not agree well with the experimental data and the FRACON code needs to be modified to include condensation and evaporation.
- ❑ The strain in the rock is underpredicted; this is probably due to the fixed boundary condition imposed at too short a radial distance (3 m) from the centre of the heater.

3. Re-evaluation of Kamaishi mine modeling- The JNC/KIPH team studies

3.1 Introduction

This section presents the work conducted by the JNC/KIPH Research team on the first phase of BMT1. The objective is to re-evaluate the modeling of the Kamaishi Mine heater test (Chijimatsu et al., 1999). In order to carry out the re-evaluation, the modeling of swelling pressure buffer material considering both the temperature and the density dependencies based on the laboratory experiment results, carried out by Japan Nuclear Cycle Development Institute, is performed at first. Then validation of this model was conducted by using the laboratory test and re-evaluation of Kamaishi heater test was carried out by an simplified axisymmetric model.

3.2 Temperature and density dependency of swelling pressure

3.2.1 Temperature dependency

Figure 3.1 shows the swelling pressure measurement results (Suzuki and Fujita, 1999). Material of the specimen was sand mixture bentonite (B:S=7:3, Dry density is 1.6 g/cm³). During the swelling pressure measurement, temperature increased step by step as shown Figure 3.1. Table 3.1 shows the final swelling pressure value of each temperature condition. Figure 3.2 shows the relationship between final swelling pressure value and temperature. In these figures, swelling pressure at 60°C is higher than that at 25°C in this experiment. However it is assumed that swelling pressure decreases with increases in temperature linearly as shown Figure 3.2 because swelling pressure at 90°C is lower than that at 25°C. The function of swelling pressure σ and temperature T is given by.

$$\sigma = 0.44 - 0.001T \quad (3.1)$$

From this equation, the swelling pressure at 25°C is calculated to be 0.415 MPa.

3.2.2 Density dependency

Figure 3.3 shows the relationship between the swelling pressure and the effective density of the buffer. This relationship is expressed by equation (3.2) (Japan Nuclear Cycle Development Institute, 2000), using the effective density calculated by equation (3.3). From equation (3.2), in the case of sand mixture bentonite (B:S=7:3) at a dry density of 1.6g/cm³, the effective density is 1.368g/cm³ and the swelling pressure was calculated to be 0.48 MPa. The density of the soil particles is assumed to be 2.65g/cm³.

$$\sigma = \exp(3.85\rho_e^2 - 7.33\rho_e + 2.09) \quad (3.2)$$

$$\rho_e = \rho_d(100 - Rs) / (100 - \rho_d Rs / \rho_s) \quad (3.3)$$

where, ρ_e is effective density (g/cm^3), ρ_d is dry density (g/cm^3), Rs is mixing ratio at dry weight of sand (%) and ρ_s is the density of the soil particles (g/cm^3), respectively.

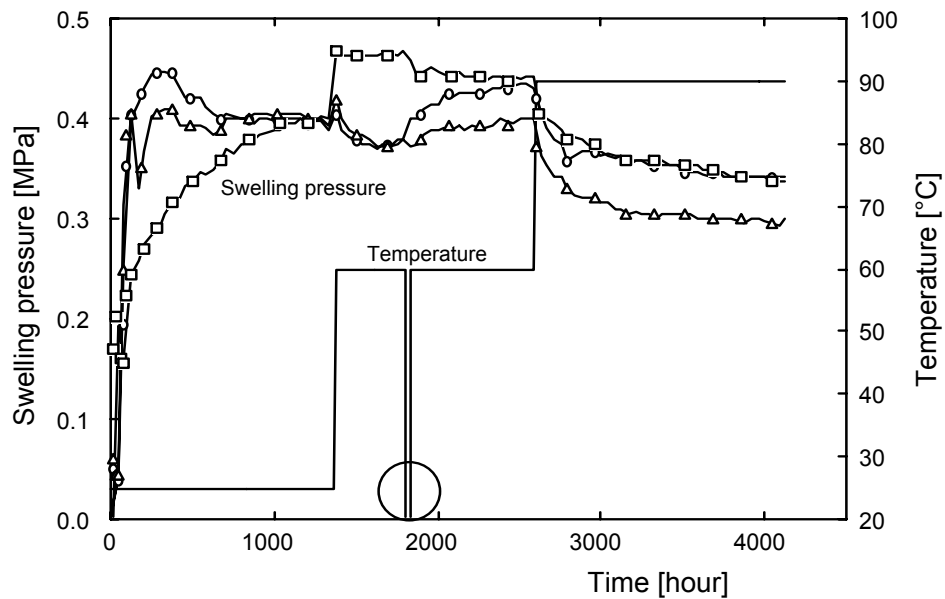


Figure 3.1: Measurement results of swelling pressure with time

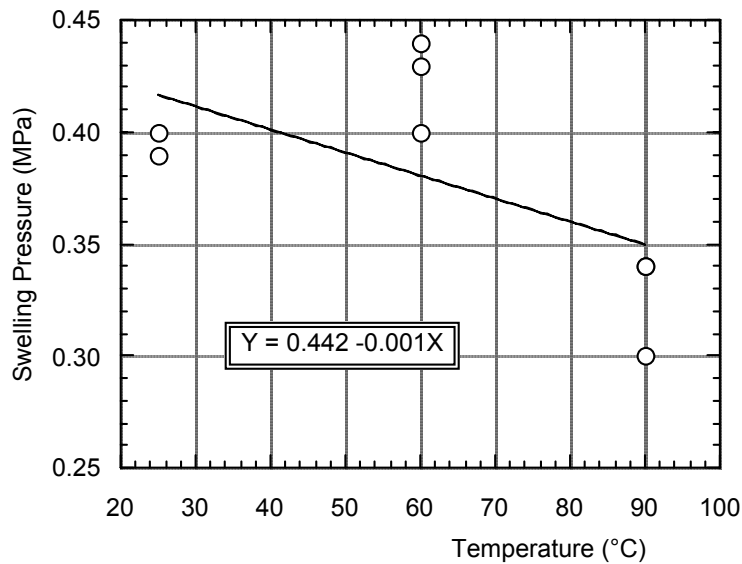


Figure 3.2: Relationship between swelling pressure and temperature

Table 3.1: Measurement results of swelling pressure (MPa)

Temperature	25°C	60°C	90°C
Swelling pressure	0.39	0.43	0.34
	0.40	0.40	0.30
	0.40	0.44	0.34

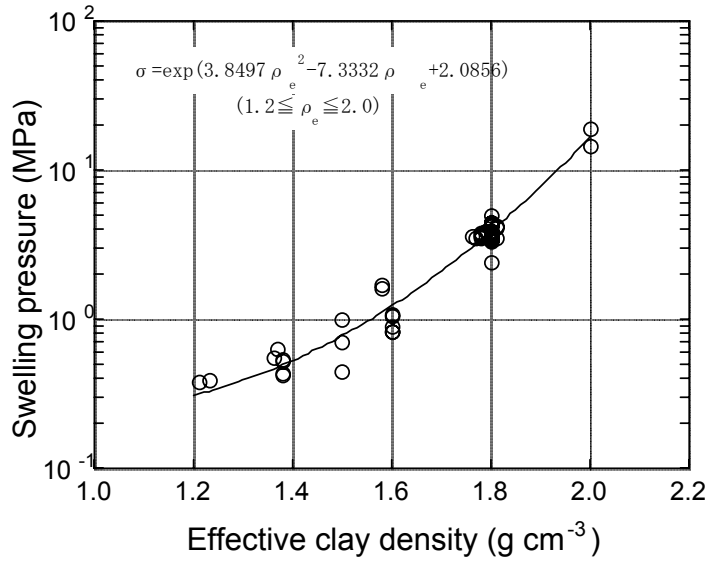


Figure 3.3: Relationship between effective clay density and swelling pressure

3.2.3 Modeling of swelling pressure

From the above results, it is assumed that swelling pressure is a function of temperature and effective density as shown in equation (3.4). In the THM simulation, the swelling pressure is modeled as a function of water potential as shown in equation (3.5), in which the coefficient F is estimated by back analysis of laboratory test. Therefore, the estimated coefficient value from the swelling pressure at temperature 25°C, dry density 1.6 g/cm³, sand mixing ratio 30% is to be F_o and the THM simulation is conducted by using F value shown in equation (3.6).

$$\sigma = \exp(3.85\rho_e^2 - 7.33\rho_e + 2.09) - 0.001T \quad (3.4)$$

$$\sigma = F\Delta\psi \quad (3.5)$$

$$F = F_o \times \left\{ \frac{\exp(3.85\rho_e^2 - 7.33\rho_e + 2.09) - 0.001T}{\exp(3.85\rho_{eo}^2 - 7.33\rho_{eo} + 2.09) - 0.001T_o} \right\} \quad (3.6)$$

where $T_o = 25^\circ\text{C}$ and $\rho_{eo} = 1.368\text{g/cm}^3$

3.3 Simulation of laboratory experiment by considering temperature and density dependencies

3.3.1 Simulation of swelling pressure tests

The simulation of swelling pressure tests at each temperature was conducted and compared with measurement results. The simulation was carried out with an axisymmetric model as shown in Figure 3.4. The material is sand mixture bentonite with dry density 1.6 g/cm³. Temperature is 25°C, 60°C and 90°C. Figures 3.5 and 3.6

show the water diffusivity and water retention curves, respectively. For the simulation, the experimental function (3.7) is adopted for water diffusivity and the van Genuchten model (3.8) is adopted for water retention curve. Table 3.2 shows the coefficients for equations (3.7) and (3.8). Table 3.3 shows the other parameters of sand mixture bentonite.

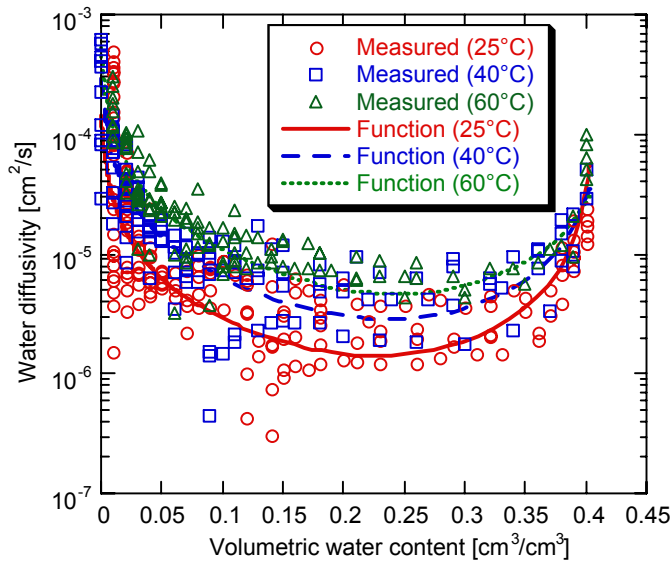
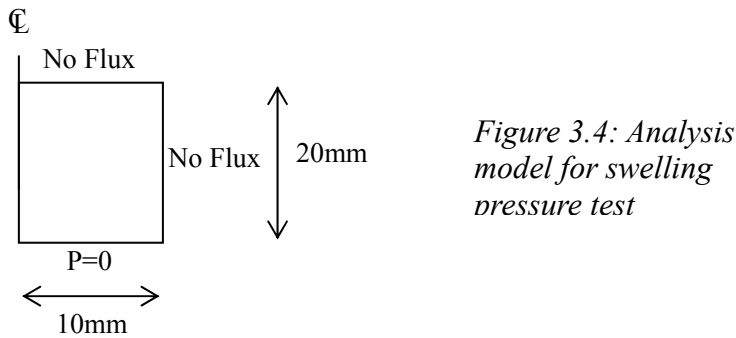


Figure 3.5: Water diffusivity of sand mixture bentonite

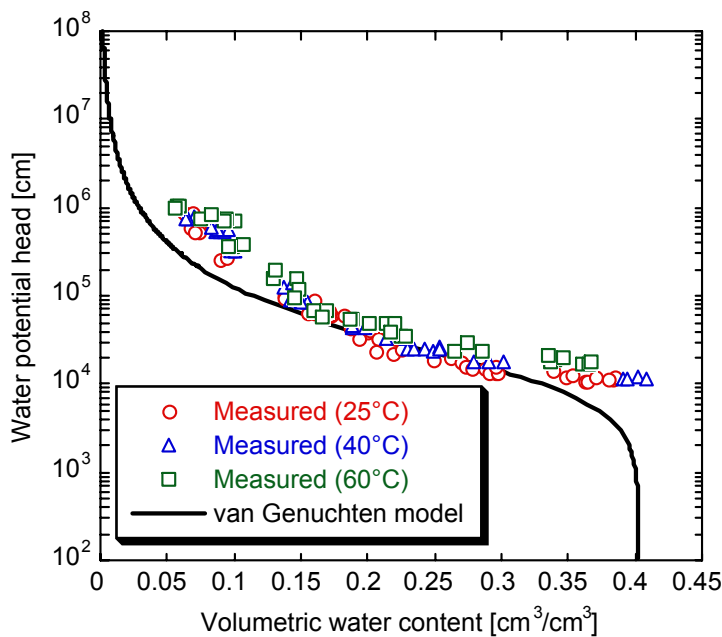


Figure 3.6: Water retention curve of sand mixture bentonite

$$D_{\theta} = \frac{a_1(\theta - \theta_s)}{(\theta - b_1)(b_1 - \theta_s)} + \frac{a_2\theta}{b_2(\theta - b_2)} \quad (3.7)$$

$$\frac{\theta - \theta_r}{\theta_s - \theta_r} = \left\{ 1 + |\alpha\psi|^n \right\}^{\left(1 - \frac{1}{n}\right)} \quad (3.8)$$

Table 3.2: Coefficients for equations (3.7) and (3.8)

Coefficient	Value
a_1	$2.99 \cdot 10^{-8}T - 3.74 \cdot 10^{-7}$
a_2	$-1.50 \cdot 10^{-8}T + 1.49 \cdot 10^{-7}$
b_1	$-2.49 \cdot 10^{-3}$
b_2	$5.59 \cdot 10^{-4}T + 3.93 \cdot 10^{-1}$
θ_s	0.403
θ_r	0.000
α	$8.0 \cdot 10^{-5}$
n	1.6

Table 3.3: Other parameters

Parameter	Value
Young's modulus (MPa)	50.0
Poisson's ratio	0.3
Intrinsic permeability (m ²)	$4.0 \cdot 10^{-20}$
Thermal conductivity (W/m/K)	$4.44 \cdot 10^{-1} + 1.38 \cdot 10^{-2}\omega$ $+ 6.14 \cdot 10^{-3}\omega^2 - 1.69 \cdot 10^{-4}\omega^3$
Specific heat (kJ/kg/K)	$(34.1 + 4.18\omega)/(100 + \omega)$
Thermal expansion coefficient (1/K)	$1.0 \cdot 10^{-5}$
Thermal water diffusivity (m ² /s/K)	$7.0 \cdot 10^{-12}$

Figure 3.7 shows the time history of the water potential in each section in the specimen. The legend in the figure shows the distance from the bottom of specimen, i.e. the distance from the seepage surface. Figure 3.8 shows the time history of water content in each section, which is higher close to the seepage surface. The specimen became saturated after approximately 300 hours. Figure 3.9 shows the time history of total pressure at each section. Because of the swelling pressure generated by the change of water potential, as used in the model, the tendency of swelling pressure generation is similar with the water potential change. Furthermore, swelling pressure became constant when the change of water potential was stopped. The swelling pressure value at the seepage side was lower than that at the opposite side, but the difference is small. Figure 3.10 shows the time history of strain at each section in the specimen. Positive values show compressive strain and negative values show tensile strain. Tensile strain occurred near the seepage surface and compressive strain occurred at the opposite side. Both tensile and compressive strains decreased with saturation of the specimen, and became zero when the specimen was fully saturated. Figure 3.11 shows the time history of dry density at each section of the specimen, which decreased at the bottom side due to the generation of the tensile strain at the early time. At the upper side it increased. The change of dry density disappeared when swelling pressure became constant, and afterwards the dry density in the specimen became uniform. Figure 3.12 shows the comparison of swelling pressures between calculated and measured results. Experiments were carried out five times and the results show the different swelling pressure values. The coefficient F_o was estimated to simulate the average swelling pressure value in the measured data (Fig. 3.12).

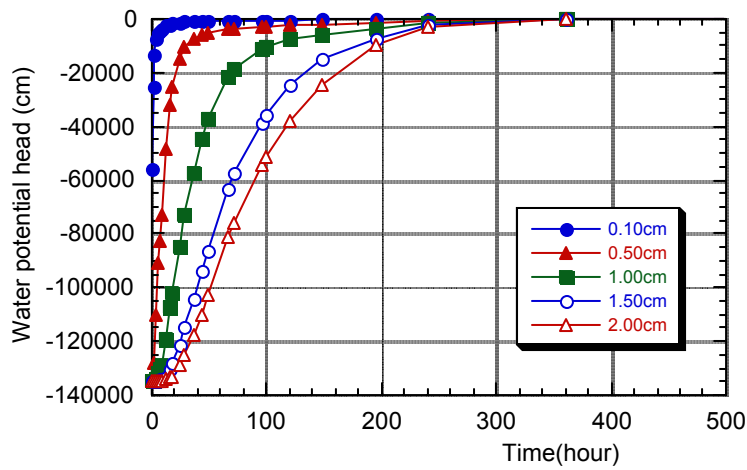


Figure 3.7: Time history of water potential in each section (Temperature is 25°C)

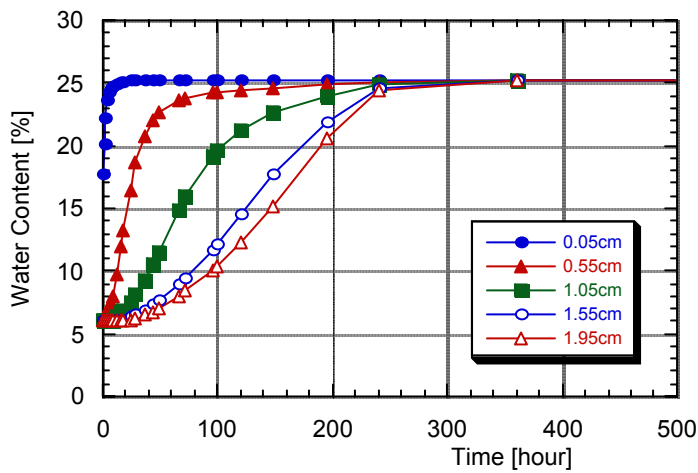


Figure 3.8: Time history of water content in each section (Temperature is 25°C)

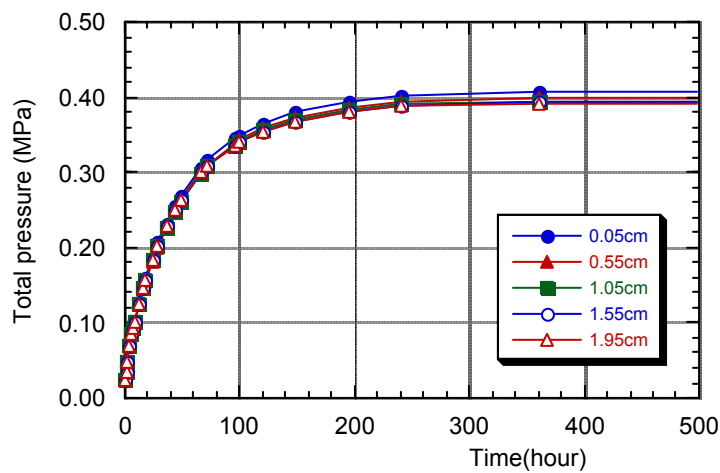


Figure 3.9: Time history of total pressure in each section (Temperature is 25°C)

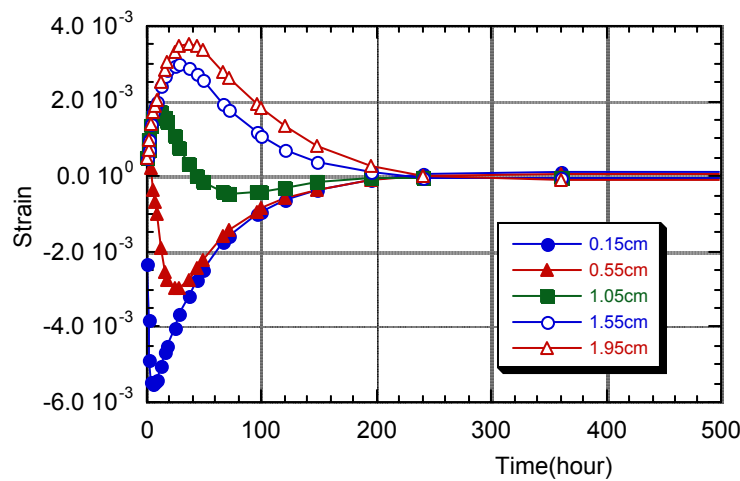


Figure 3.10: Time history of strain in each section (Temperature is 25°C)

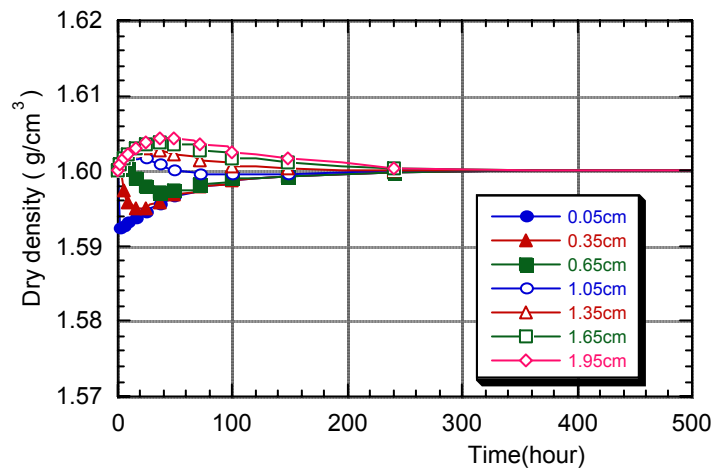


Figure 3.11: Time history of dry density in each section (Temperature is 25°C)

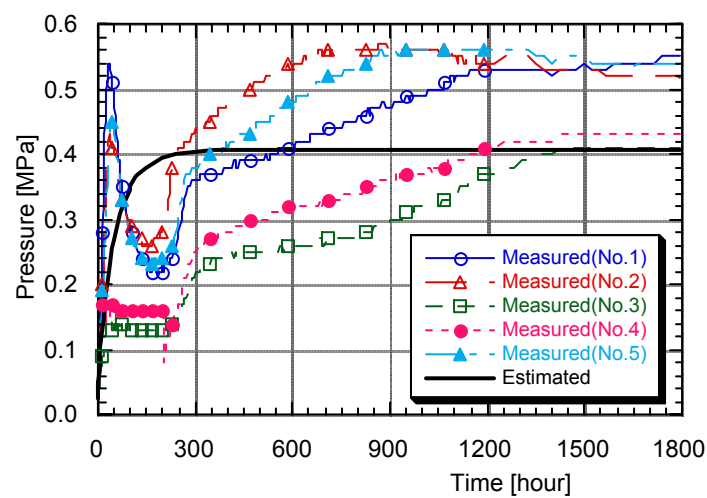


Figure 3.12: Comparison of pressure between analytical and measurement result

Figure 3.13 and Figure 3.14 shows the time history of water content and total pressure at each section in the specimen when the temperature is 60°C, respectively. Figure 3.15 and Figure 3.16 also show the time history of water content and total pressure at each section in the specimen when the temperature is 90°C. The time needed for the specimen becoming fully saturated decreases with increasing temperature and the time needed for the swelling pressure becoming constant also decreases. Furthermore, the swelling pressure value decreases with increasing temperature.

3.3.2 Simulation of the coupled test in laboratory

3.3.2.1 Outline of coupled test

Figure 3.17 shows the test apparatus used for the coupling test, which consists of the water movement under a thermal gradient and water injection (Suzuki et al., 1999). The test apparatus is composed of a specimen, a main unit of 50-mm in diameter and 100-mm in height, a heating chamber, a copper plate, a thermostat with a circulation system, thermocouples, load cells, and a data logger. During the test, the temperature of the thermostat connected to the heating chambers above and below the specimen is controlled at specified temperature. Furthermore, water is injected from the upper side of the specimen at water head of 100cm. Measurement items are total infiltration quantity into the specimen, temperature and swelling pressure. Temperature is measured by thermocouple at locations 0.2, 2.0, 4.0, 6.0, 8.0, 9.8cm from the bottom of the specimen, respectively, with the data logger. Swelling pressure is measured by load cell at locations 1.0, 3.0, 5.0, 7.0, 9.0cm from the bottom of the specimen, respectively, with the data logger. Swelling pressure is also measured at the upper surface of the specimen. The water distribution is obtained by measuring the water content by the oven-dry method after dividing the specimen in the apparatus when test is finished.

3.3.2.2 Measurement result

Figure 3.18 shows the time history of infiltration quantity into the specimen. 65cc of water injected into the specimen and injection was stopped after 7000 hours. Theoretical maximum infiltration quantity is approximately 60cc. The reason for less measured infiltration quantity than the theoretical one was considered to be the influence of evaporation of water. Figure 3.19 shows the time history of the swelling pressure. The swelling pressure also becomes constant after 7000 hours and this agrees with the change in infiltration quantity. The value of the swelling pressure is approximately 0.4 MPa at the upper side of specimen and approximately 0.2MPa at the lower side of specimen. That means that the swelling pressure at the upper side is higher than that at the lower side. The upper side is the infiltration side with lower temperature under a thermal gradient. After the coupled test was finished, the water content distribution was measured and Table 3.4 shows the results. The theoretical saturated water content of this specimen is approximately 25% and it is judged that the specimen after coupled test was almost saturated. From Table 3.4, it is shown that the water content at the infiltration side and center part of the specimen is higher than other part.

The reason of the high water content at the infiltration side is due to the swelling at the early stage of coupled test. The reason of high water content at the center part is due to the low dry density of this part due to difficulty of uniform manufacturing.

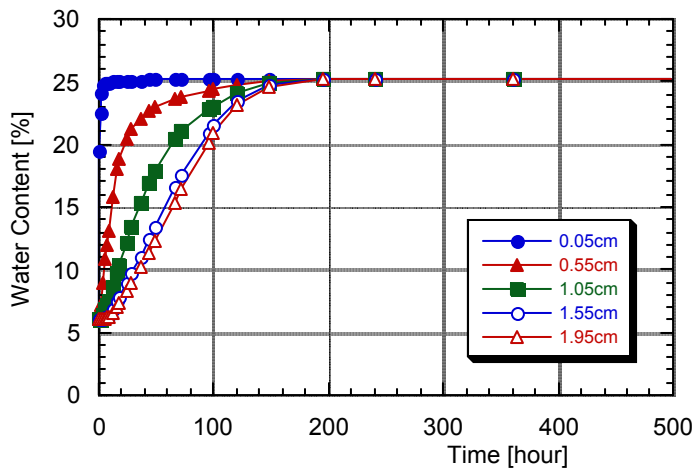


Figure 3.13: Time history of water content in each section (Temperature is 60°C)

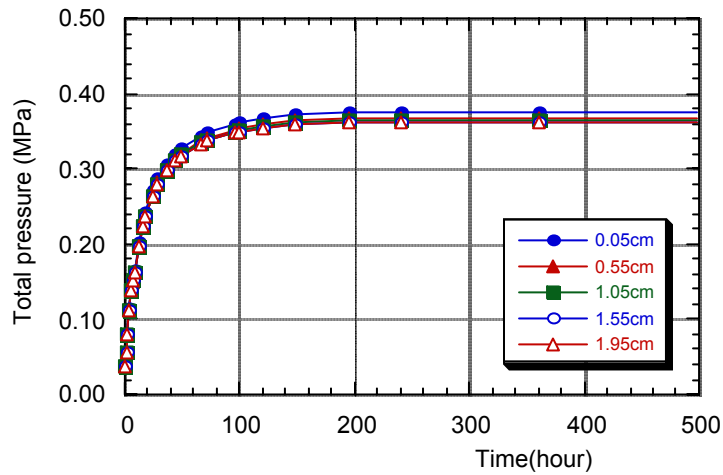


Figure 3.14: Time history of total pressure in each section (Temperature is 60°C)

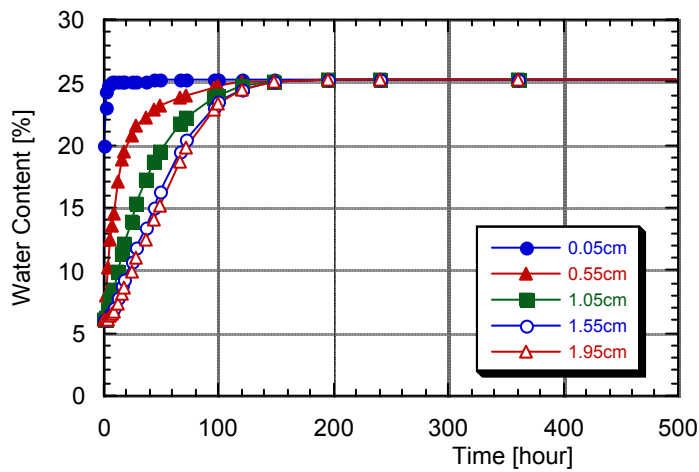


Figure 3.15: Time history of water content in each section (Temperature is 90°C)

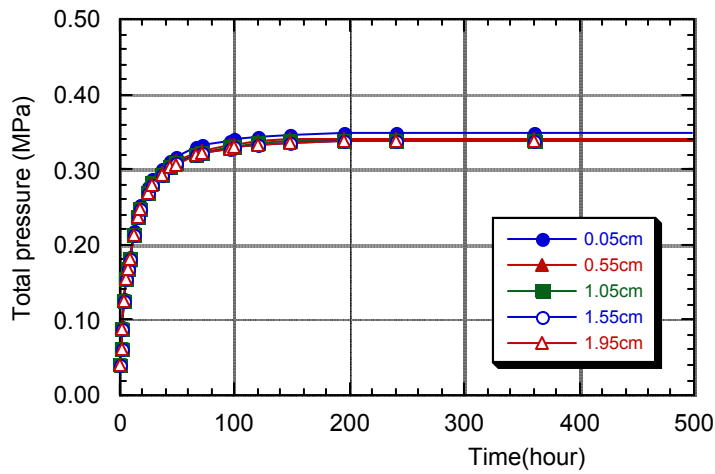


Figure 3.16: Time history of total pressure in each section (Temperature is 90°C)

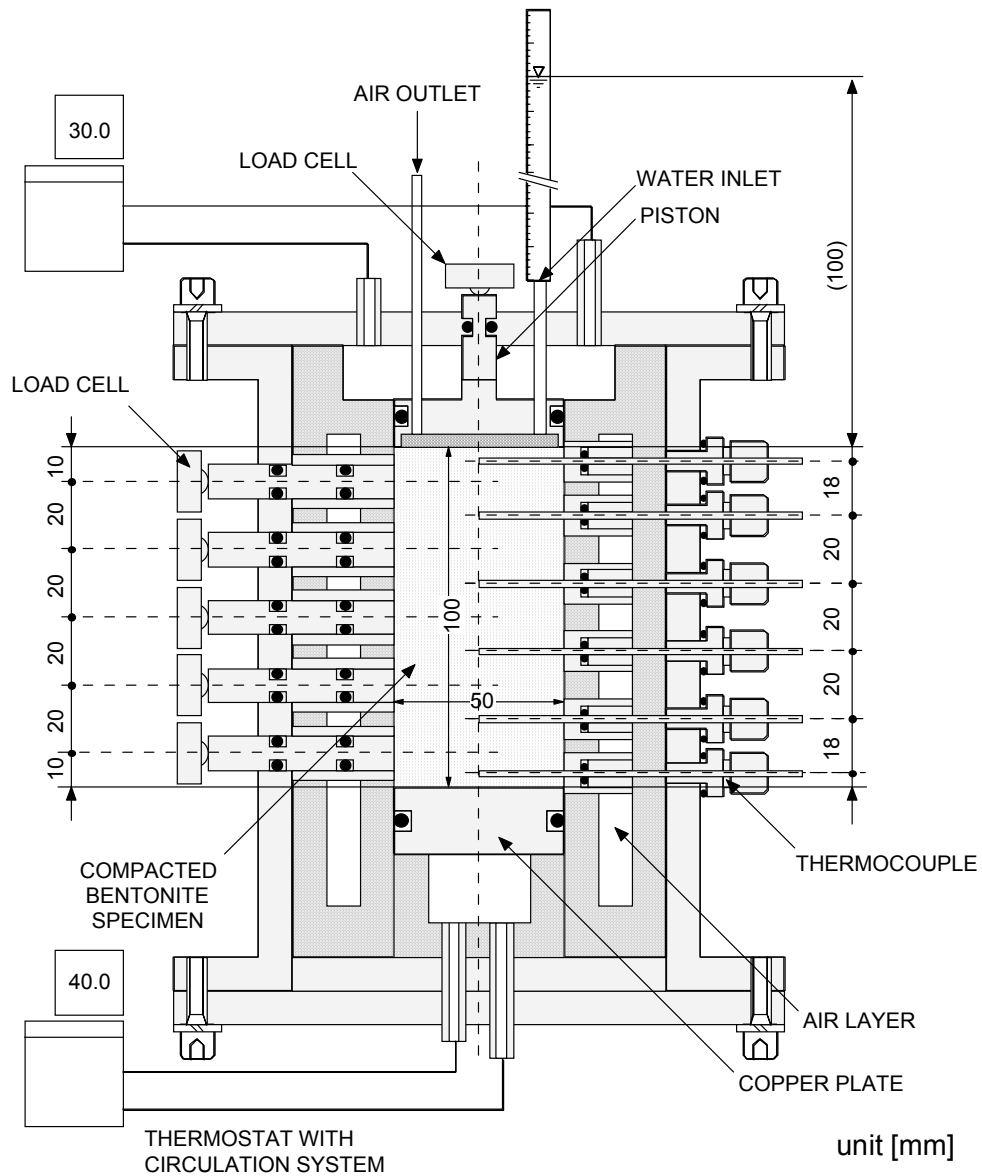


Figure 3.17: Test apparatus for coupled test

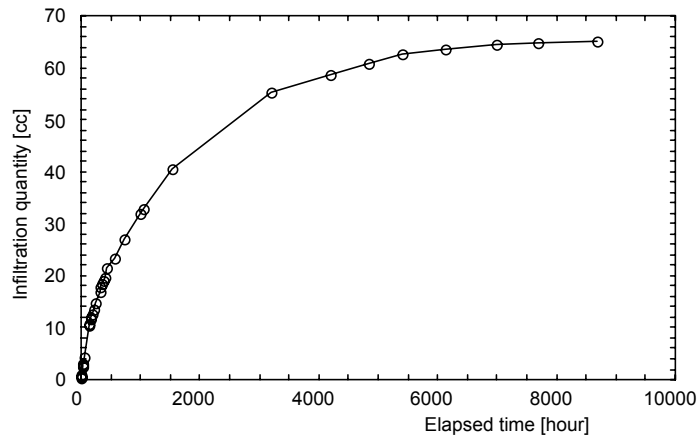


Figure 3.18: Measured infiltration quantity into the specimen

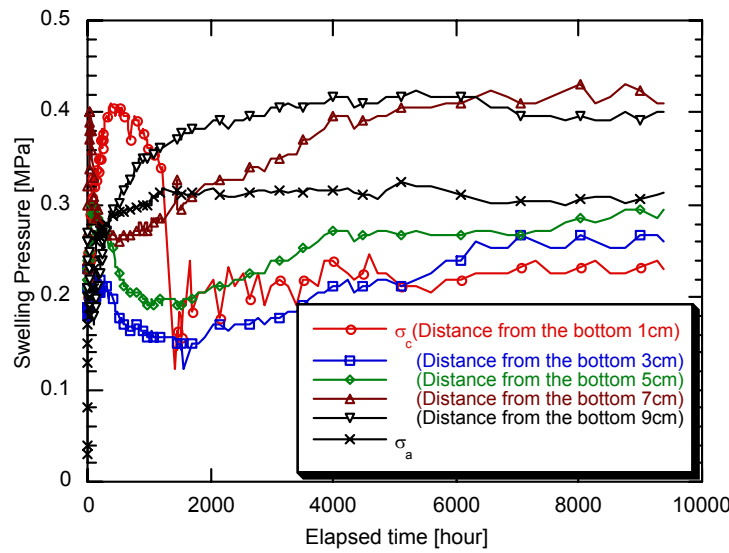


Figure 3.19: Measured swelling pressure

Table 3.4: Measured water content distribution

Distance from the infiltration surface (cm)	Water content (%)
0.5	27.68
1.5	25.27
2.5	25.18
3.5	25.44
4.5	26.20
5.5	26.43
6.5	25.57
7.5	25.63
8.5	24.77
9.5	24.67
Average	25.68

3.3.2.3 Analysis model

The analysis was carried out with an axisymmetric model (Fig. 3.20). For the thermal boundary conditions, the upper surface was fixed with a temperature of 30°C and the bottom surface with 39°C. The side of the model was adiabatic. For the hydraulic

boundary conditions, the upper surface was fixed with a water head of 100-cm and other surfaces were no flow boundaries. The initial water content was 6.0%. Mechanically all surfaces were fixed with a zero normal displacement.

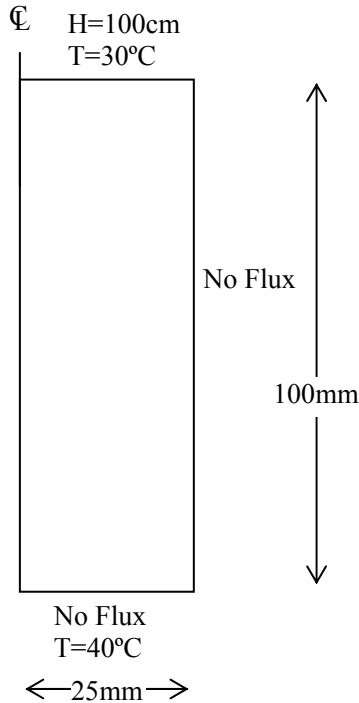


Figure 3.20: Analysis model for coupled test

3.3.2.4 Analysis results

Figure 3.21 shows the time history of water content in the bentonite. Legend X expresses the distance from the bottom surface of the specimen. That is, X=0 cm is the high temperature surface and X=10 cm is the low temperature surface. It shows that the low temperature side (the infiltration side) became saturated earlier than the opposite side (the higher temperature side). Water content at the high temperature side decreased at first, however the influence of temperature was small and water content increased latter. After 8000 hours from the start, water content change became steady, and at the upper side it was approximately 25%, indicating that the upper side was saturated. The water content at the lower side was smaller than that at the upper side.

Figure 3.22 shows the time history of dry density. It shows that the dry density near the infiltration side became low at the early time of experiment due to swelling. However, the dry density at the high temperature side also became low finally. From this result, it was expected that the saturated water content at the high temperature side should become higher than 25%. However, as a result of the simulation, the water content at the high temperature side became lower than 25%, i.e. not saturated. Figure 3.23 compares the water infiltration quantity between calculated and measured results, with good agreement in general tendency, but different final values. The estimated water infiltration quantity was less than 60cc because the theoretical maximum value of water infiltration quantity was approximately 60cc.

Figure 3.24 shows the time history of total pressure in each section. As a result of simulation, total pressure at the high temperature side was lower than that at the low temperature side and this tendency is similar to the measured result.

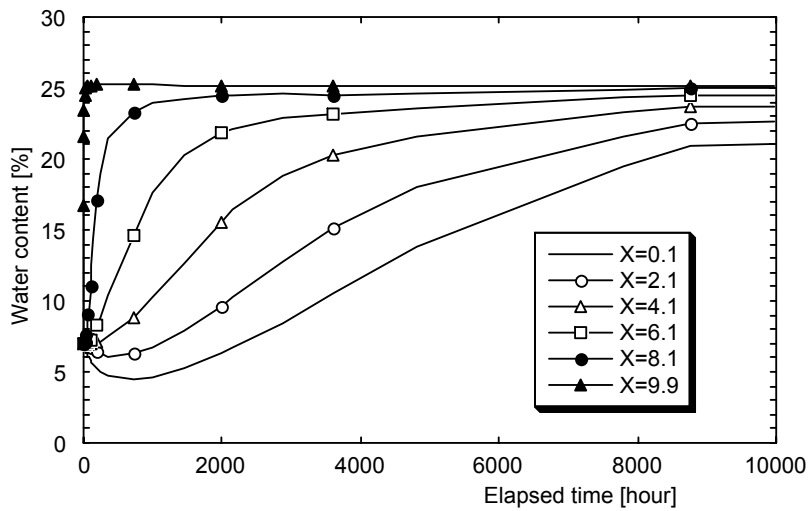


Figure 3.21: Time history of water content by simulation

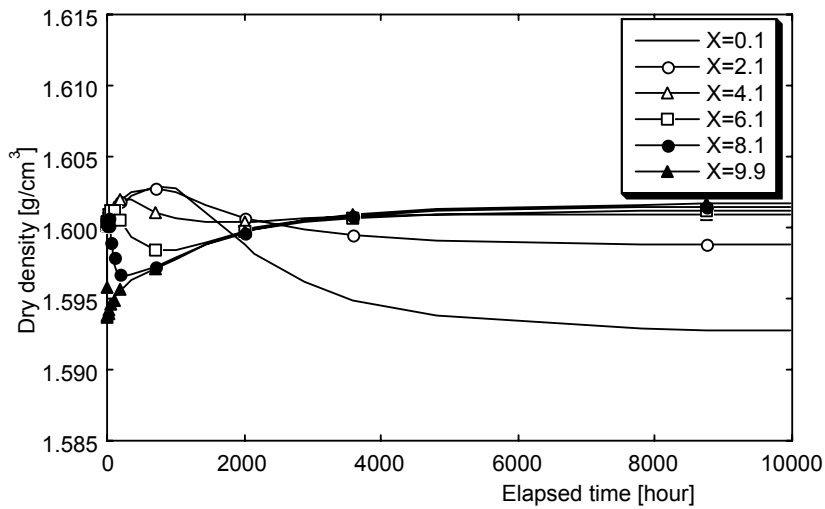


Figure 3.22: Time history of dry density by simulation

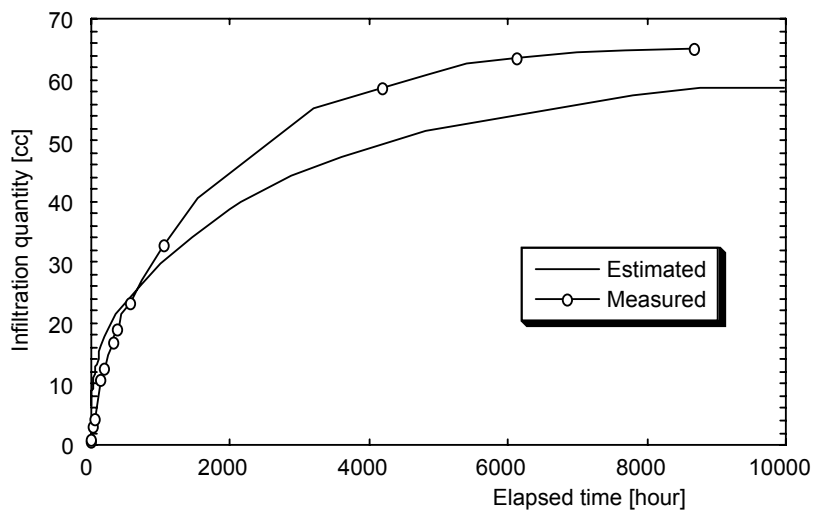


Figure 3.23: Comparison of water infiltration quantity between estimated and measured results

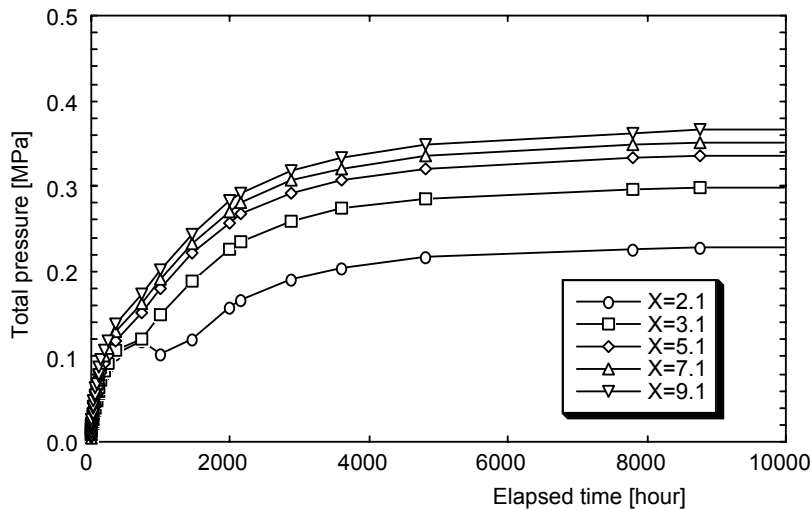


Figure 3.24: Time history of total pressure by simulation

3.4 Re-evaluation of Kamaishi THM experiment

3.4.1 Analysis model

In this section, the re-evaluation of the Kamaishi THM experiment is presented by using a simplified axisymmetric model (cf. Fig. 1.12), with the boundary conditions and locations of output points shown in Fig. 3.25. Simulation was performed both in the heating phase (258 days) and the cooling phase (180 days).

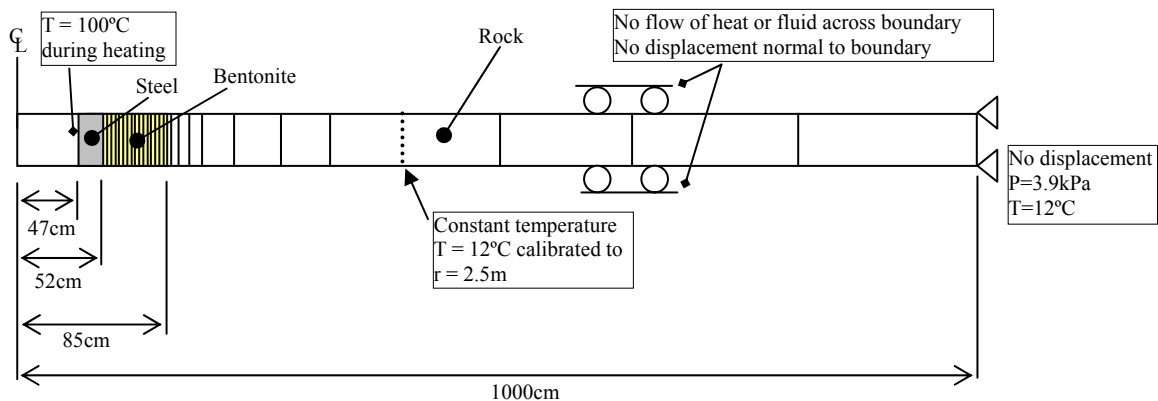


Figure 3.25: Model geometry and boundary conditions

3.4.2 Parameters for simulation

Many parameters of bentonite were obtained by laboratory tests directly (Fujita et al., 1997). The water diffusivity is a function of volumetric water content and temperature. The water potential is a function of volumetric water content. These relationships were determined by laboratory tests. The thermal water diffusivity and parameters for swelling pressure were determined by back analysis of laboratory test. Furthermore, the thermal expansion coefficient is newly calibrated.

3.4.2.1 Water diffusivity and water retention curve

The intrinsic permeability K [m^2] and the water diffusivity D_d [cm^2/s] of bentonite are shown in equations (3.9) and (3.10). The intrinsic permeability was obtained by permeability test and water diffusivity was obtained by infiltration test directly. The water diffusivity was assumed to be the sum of vapor diffusivity D_{θ_v} and liquid diffusivity D_{θ_l} , and the functional equation is shown in equation (3.10). Figure 3.26 shows the measured water diffusivity value and the function value.

$$K = 2.00 \times 10^{-20} \quad (3.9)$$

$$D_{\theta} = D_{\theta_v} + D_{\theta_l} = \frac{(3.68 \times 10^{-8} T - 2.08 \times 10^{-7})(\theta - \theta_s)}{(\theta + 1.00 \times 10^{-3})(-1.00 \times 10^{-3} - \theta_s)} + \frac{\theta(-3.58 \times 10^{-9} T - 2.19 \times 10^{-7})}{0.41(\theta - 0.41)} \quad (3.10)$$

where, θ_s is a saturated volumetric water content.

The water potential is measured by thermocouple psychrometer. The relation between the water potential and the water content is called the water retention curve. This relation is very important for the simulation of unsaturated flow. In this simulation, the real experimental values were used as tabular data except at full saturation where the water potential was set to 0. Figure 3.27 shows the measured water potential and water retention curve that was used for simulation.

3.4.2.2 Thermal water diffusivity

The thermal water diffusivity D_T [$\text{cm}^2/\text{s}^\circ\text{K}$] is assumed to be a function of temperature as shown in equation (3.11).

$$D_T = D_{T_o} \exp\left(\alpha_T \frac{T - T_o}{T_o}\right) \quad (3.11)$$

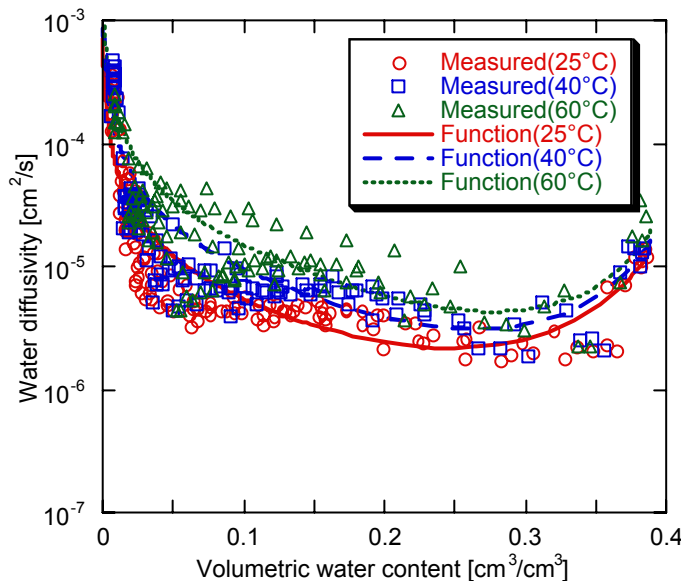


Figure 3.26: Measured and functional water diffusivity

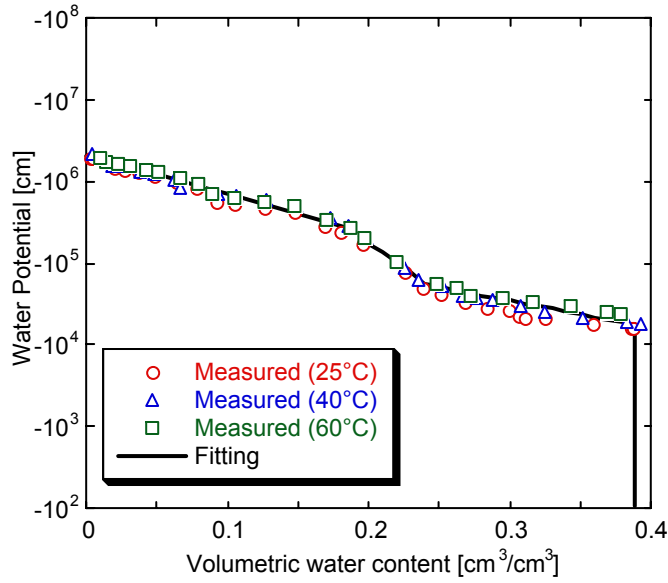


Figure 3.27: Water retention curve for simulation

where, D_{T_0} is a thermal water diffusivity at the reference temperature T_0 , α_T is a coefficient. These parameters were obtained by back analysis of laboratory test. As a result of back analysis, following parameters were determined.

$$D_{T_0} = 1.0 \cdot 10^{-7} \quad (3.12)$$

$$\alpha_T = 0.1 \quad (3.13)$$

$$T_0 = 10 \text{ }^\circ\text{C} \quad (3.14)$$

3.4.2.3 Parameter for swelling pressure

Parameters for swelling pressure F were calibrated by the results of the Kamaishi THM experiment, together with the thermal expansion coefficient α [1/K] of bentonite. As a result of calibration by in-situ THM experiment, the thermal expansion coefficient α of bentonite was increased from $1.0 \cdot 10^{-6}$ (Rutqvist et al., 2001b) to $1.0 \cdot 10^{-5}$, and swelling pressure parameter F was decreased from 0.190 to 0.010.

3.4.2.4 Other parameters

Table 3.6 shows the other parameters. Three materials (steel (heater), bentonite and rock mass) were considered. The young's modulus E , the specific heat c and the thermal conductivity λ of bentonite are the function of water content ω .

$$E = 254.9 - 8.854\omega \quad (3.15)$$

$$c = \frac{42.6 + 4.18\omega}{100 + \omega} \quad (3.16)$$

$$\lambda = 0.050\omega + 0.503 \quad (3.17)$$

Table 3.6: Parameters for simulation

Parameter	Heater	Bentonite	Rock mass
Young's modulus [MPa]	$2.0 \cdot 10^5$	Equation (3.17)	$2.81 \cdot 10^4$
Poisson's ratio [-]	0.3	0.3	0.3
Density [g/cm ³]	7.80	2.04	2.75
Intrinsic permeability [m ²]	$1.0 \cdot 10^{-27}$	$2.0 \cdot 10^{-20}$	$1.98 \cdot 10^{-16}$
Specific heat [kJ/kg/K]	0.46	Equation (3.18)	0.833
Thermal conductivity [W/m/K]	53.0	Equation (3.19)	2.71
Thermal expansion coefficient [1/K]	$1.64 \cdot 10^{-6}$	Equation (3.16)	$1.0 \cdot 10^{-6}$

3.4.3 Analysis result

Figures 3.28- 3.31 show the analysis results. Figure 3.28 shows the time history of temperature at each output point. The outer thermal boundary of the model was defined to be located at 10m. However, in order to match the observed temperature, the constant temperature boundary had to be applied closer to the heat source. As a result, the constant temperature boundary was calibrated to be located at a radius of 2.5m. During the heating phase, the temperatures at all output points increased rapidly and became constant at an early time. The decrease of temperature in the cooling phase was also rapid and these become constant immediately. Figure 3.29 and 3.30 show the time histories of water content and stress in the bentonite. The stresses during the heating phase increased at all output points. The largest stress occurred at point 1, which decreased suddenly just after the heater was turned off. However, it increases gradually with increasing water content in the bentonite. The stresses at the points 2 and 3 increased continuously even after the heater was turned off. Figure 3.31 shows the time history of strain both in the bentonite and rock mass. Positive values indicate tension and negative values indicate compression. Compressive strain occurred in the bentonite just after the start of experiment and tensile strain occurred in the rock mass. When the heater was turned off, magnitudes of strains decreased.

Figure 3.32 to Figure 3.36 show the comparison between calculated and measured results. Figure 3.32 shows the comparison of temperature and Figure 3.33 shows the comparison of water content, respectively. Calculated temperature agrees well with measured ones. Calculated water content has also good agreement with measured ones except at point 2. Figure 3.34 shows the time history of stress at the point 1 near the heater. Measured values are different in magnitudes but show the same tendency, i.e. the stress increased during the heating phase and decreased when the heater was turned off. The calculated result shows the same tendency and agrees fairly well with the results measured at BBC section. Figures 3.35 and 3.36 show the comparison of strain in the bentonite and rock mass. Measured values show high tensile strains just after the experiment started but this did not appear in the simulation. However, the tendency of variation after that is almost similar, even though the absolute values are different. Furthermore, in the rock mass, compressive strain was measured just after the heater was turned off, but it did not occur in the simulation. The reasons may be that the mechanical constitutive law is inappropriate and unsuitable properties were used about the bentonite and rock mass.

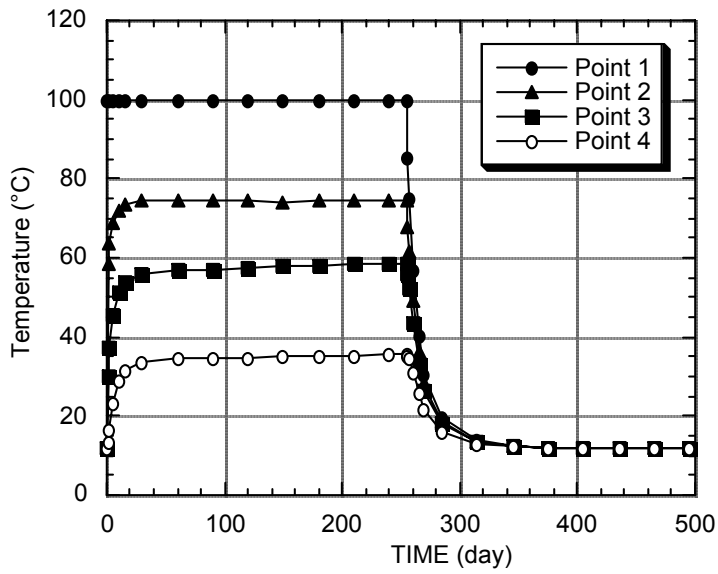


Figure 3.28: Time history of temperature at each point by simulation

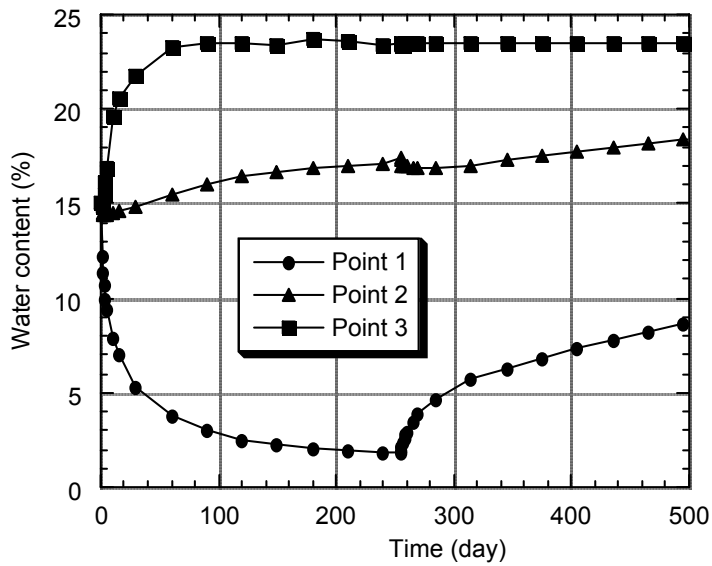


Figure 3.29: Time history of water content at each point by simulation

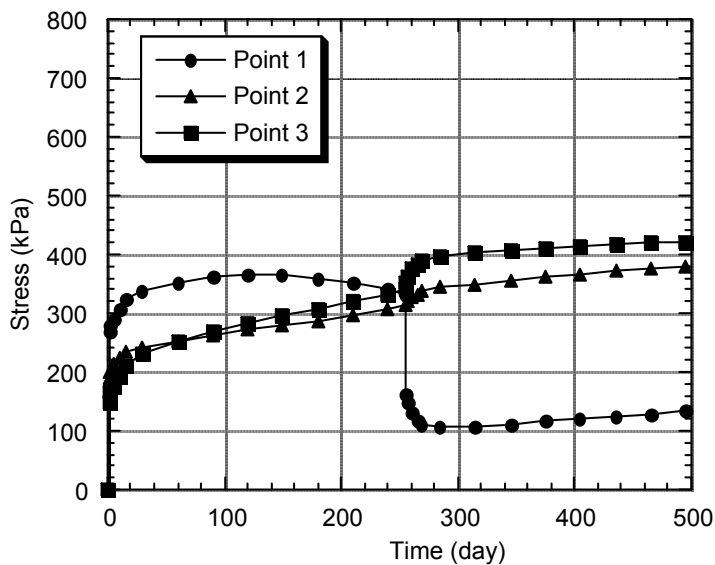


Figure 3.30: Time history of stress at each point by simulation

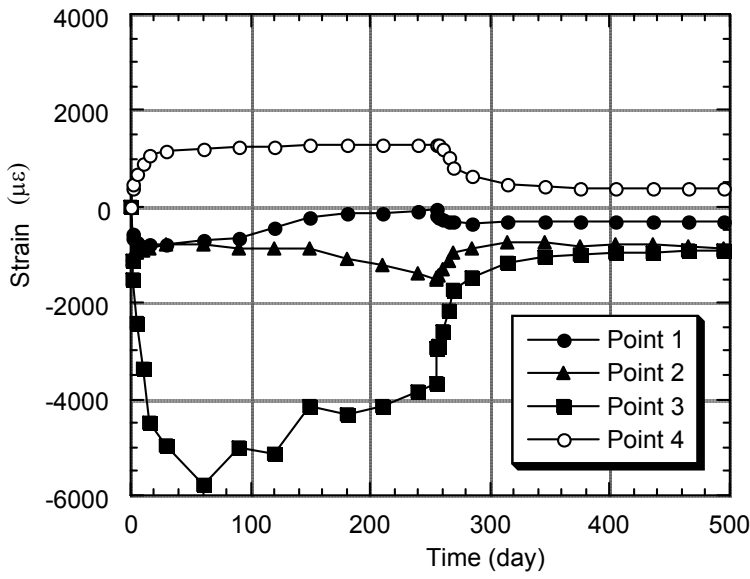


Figure 3.31: Time history of strain at each point by simulation

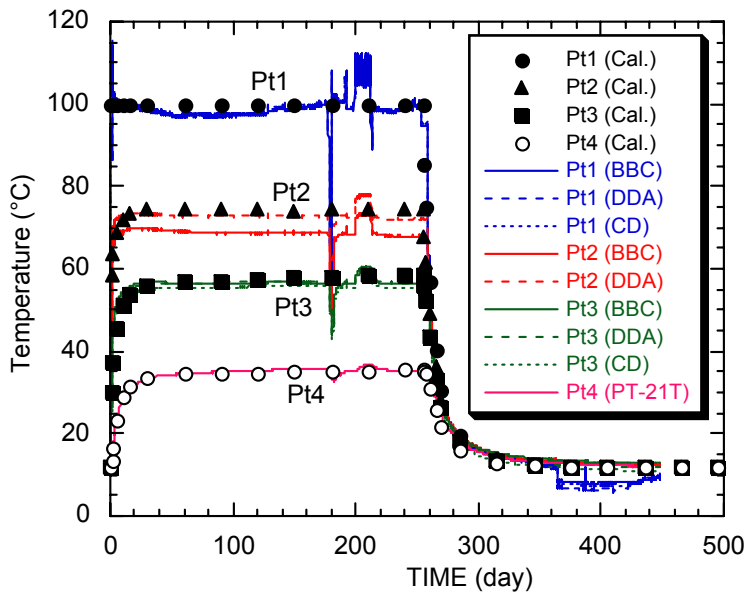


Figure 3.32: Comparison of temperature between measured and calculated results

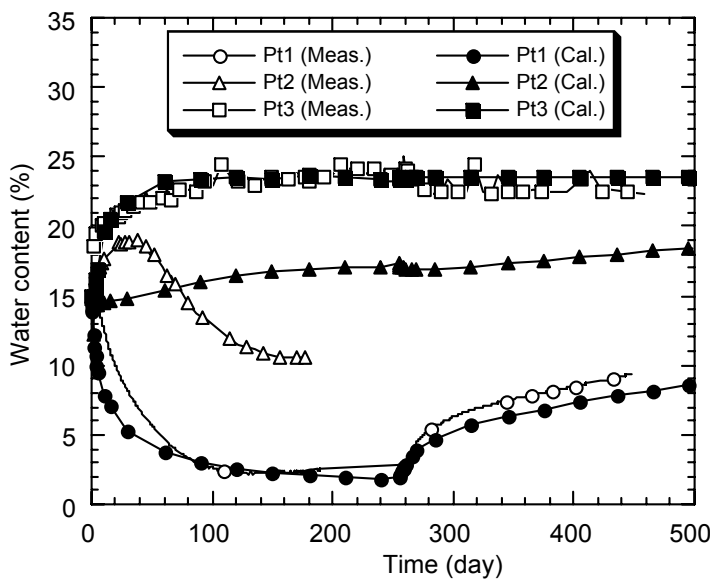


Figure 3.33: Comparison of water content between measured and calculated results

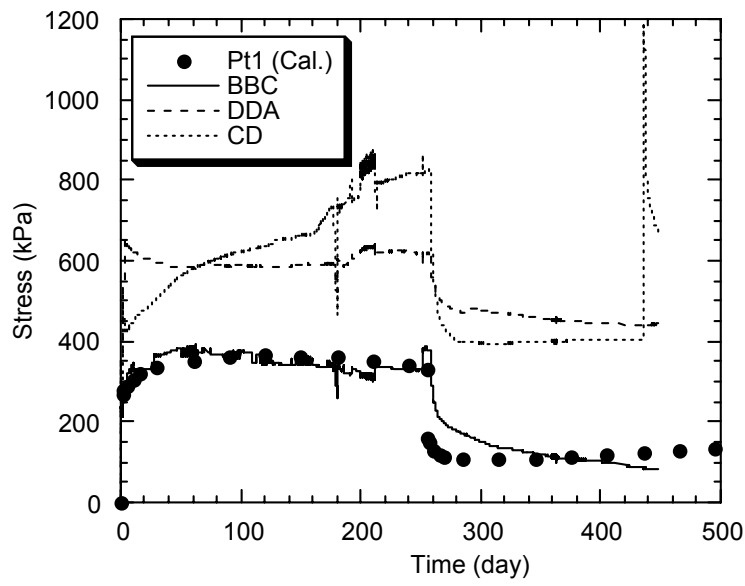


Figure 3.34:
Comparison of stress
between measured
and calculated
results

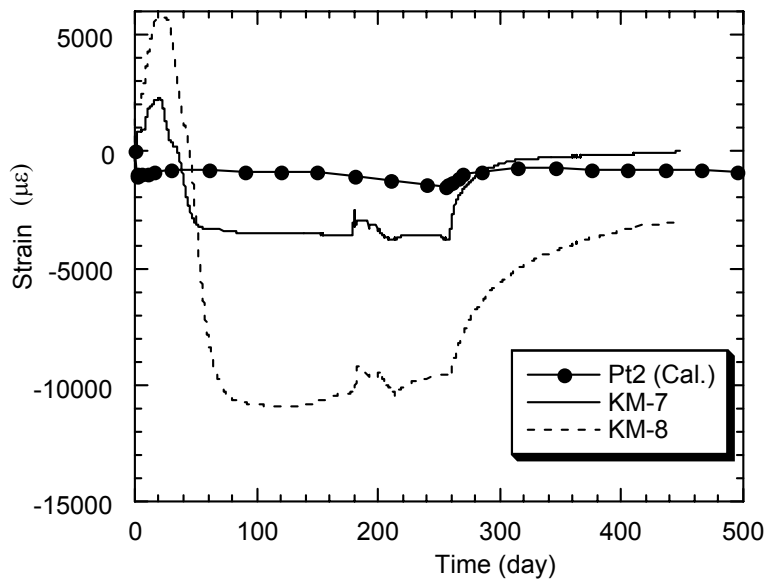


Figure 3.35:
Comparison of
strain in the buffer
between measured
and calculated
results

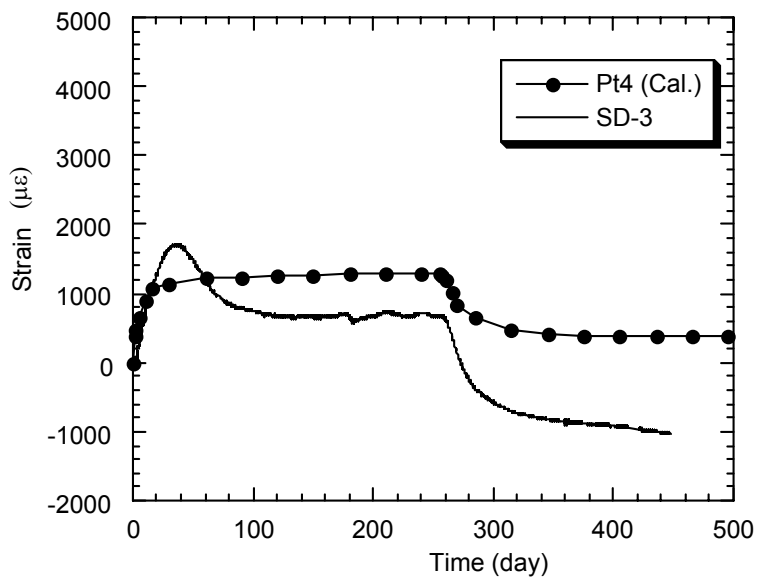


Figure 3.36:
Comparison of strain
in the rock mass
between measured
and calculated
results

3.5 Summary

In this section, modeling of swelling pressure that took into account the temperature and the density dependency was presented. This model was validated using the laboratory-scale coupled test and shows good agreement with measured data. Using this model, re-calibration of Kamaishi THM experiment was performed. Although the model geometry is simplified compared with the field test environment, the simulation results show the similar tendency with the measured results. In this re-evaluation, the mechanical behavior was the main focus for simulation. In order to capture the observed mechanical behavior in simulation, thermal expansion coefficient and swelling pressure parameter were calibrated from the in-situ measurement results. As the results, the swelling pressure parameter was decreased from its former value that was obtained by back analysis of laboratory test. The decreased swelling pressure parameter and the increased thermal expansion coefficient of the bentonite gave a good agreement with the observed mechanical behavior of the bentonite. From these results, it is suggested that a reasonable prediction of the mechanical behavior is possible if bentonite parameters are properly obtained by the laboratory tests. Furthermore, more reasonable constitutive law of the unsaturated bentonite is needed to evaluate the mechanical behavior more properly.

4. Re-evaluation of Kamaishi mine modeling-The SKI/KTH team studies

This section presents the work conducted by the KTH/SKI team on the first phase of BMT1. The objective is to re-evaluate the modeling of the Kamaishi Mine heater test to possible obtain a better understanding of physical processes and to improve the confidence in the numerical model that will be used for the modeling of BMT1.

4.1 Suggestions for improved modeling of the Kamaishi Mine Heater Test

As a part of the previous DECOVALEX II project, the Kamaishi Mine heater experiment was modeled using the finite element code ROCMAS (Rutqvist et al., 1999). The most significant part was to predict THM responses in the bentonite and the near-field rock during the 8.5-month heating and 6-month cooling periods of the heater test. The results showed that, in general, the predicted and observed responses matched well or satisfactory regarding temperature, water content and fluid pressure (Rutqvist et al., 1999 and 2001b). The predictions were less satisfactory regarding the mechanical behavior of the buffer (swelling stress). For example, the modeling predicted that tensile stress would develop near the heater while the observed stress was compressive. Rutqvist et al., (1999) presented a few possible improvements to the modeling of the Kamaishi Mine. They are summarized in Table 4.1 and briefly discussed below.

Table 4.1: Modeling of Kamaishi Mine Heater Test in DECOVALEX II: Summary of Agreement Between Observations and Predictions using ROCMAS and Suggestions for Possible Improvements of the Modeling.

Process	Agreement	Possible Improvements
Temperature in buffer and rock	Very good	
Water content in buffer	Good general response	Reduce infiltration from rock by lowering rock permeability and considering sealing of rock fractures with bentonite material
Fluid pressure in rock	Satisfactory	
Swelling pressure in buffer	Both model and field \Rightarrow low swelling stress (<0.5 MPa). Uncertain at low saturation	An improved mechanical model (i.e. no tension material). Model calibration against a shrinking test at low saturation. Increased thermal expansion coefficient of the benonite
Displacement in rock	Satisfactory for the limited data available. Small displacements	Need more displacement measurements. A reduced thermal expansion of the rock mass compared to intact rock.

In the modeling of the Kamaishi Mine heater test, the predicted responses of water content in the buffer was satisfactory except at the rock/bentonite interface in areas above and below the heater. As an example, Fig. 4.1 presents the predicted and measured evolution of water content in point BW1, which is located in the bentonite about 1 centimeter from the rock wall (Rutqvist et al, 2001a). The figure indicates that a correct rate of infiltration would be achieved for a rock permeability of between $1 \cdot 10^{-16}$ and $1 \cdot 10^{-20} \text{ m}^2$. The CLAY team used a rock permeability of $1 \cdot 10^{-20} \text{ m}^2$ which is roughly equal to the intact rock permeability. However, there are two more complicating features that should be recognized in this context:

- 1) Some of the monitoring points showing a delayed rock water infiltration (for example BW3) were located right next to highly conductive fractures (Fig. 4.2). Near BW3, the rock permeability is comparatively high and intuitively the bentonite at this location should be wetted rapidly (Fig. 4.2b).
- 2) The field measurements indicate that the wetting of the bentonite is uniform (axisymmetric) with no visible effect of the high permeability fractures in the otherwise low permeable rock (Fig. 4.2a). Again, intuitively one would expect a more rapid wetting of the buffer near a high permeability fracture (Fig. 4.2b).

Figures 4.3 and 4.4 present a few possible scenarios that could lead to a delayed and uniform infiltration from the rock into the bentonite. Following the arguments given in these figures it appears that the most likely scenario is that the rock permeability in the near field is small and that high permeability fractures have been sealed with bentonite material. The physical aperture of the main fractures are in the orders of a millimeter (Fujita et al., 1996). Bentonite could penetrate during the compaction of the buffer and later swell in contact with water. This would effectively seal-off fractures for water flow.

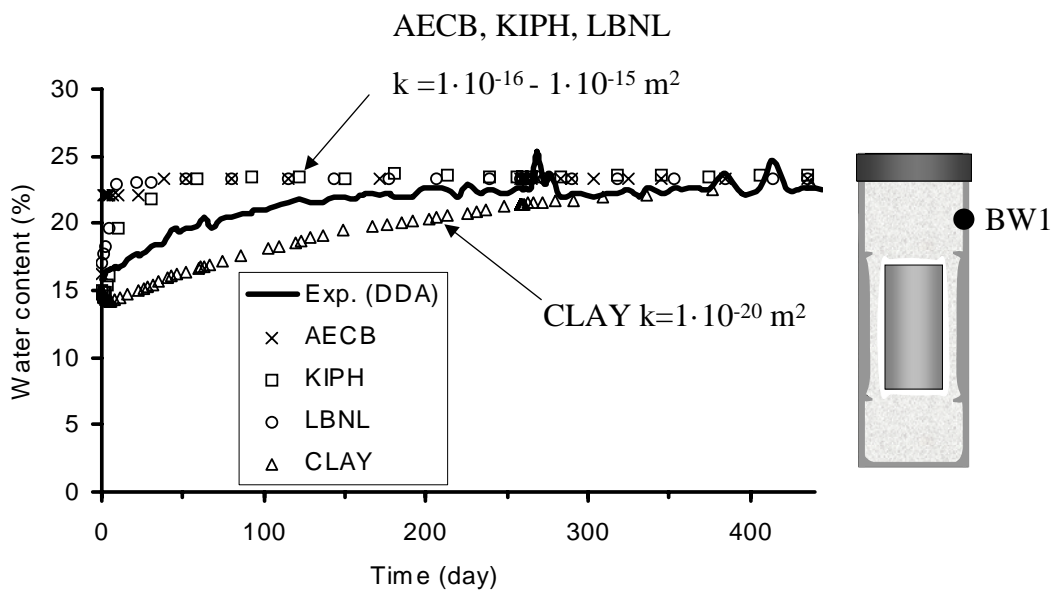


Figure 4.1: Result of previous modeling of the Kamaishi Mine heater test. Predicted (symbols) and observed (line) evolutions of the water content at the rock/buffer interface.

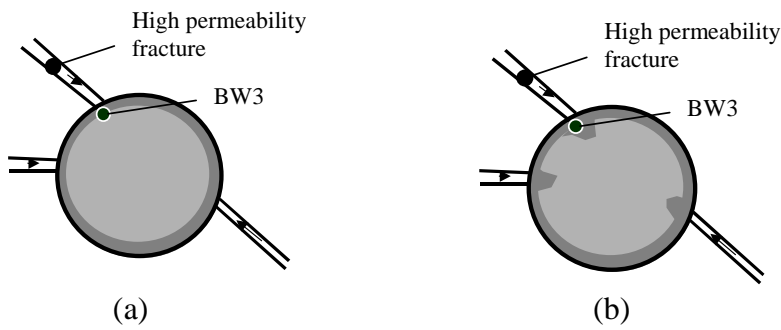


Figure 4.2: (a) Observed uniformly axisymmetric wetting of the bentonite with no influence of high permeability fractures and (b) intuitively more rapid wetting at high permeability fractures.

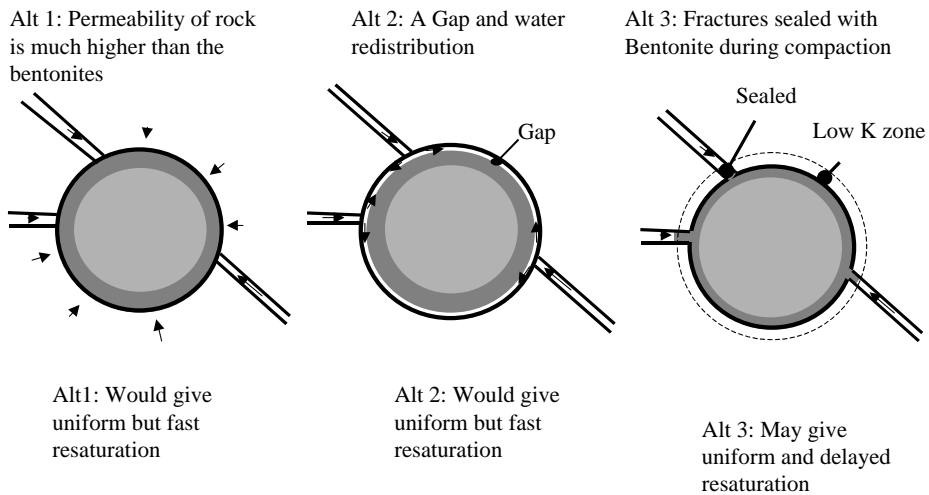


Figure 4.3: Three possible scenarios leading to a uniform (axisymmetric) wetting of the bentonite.

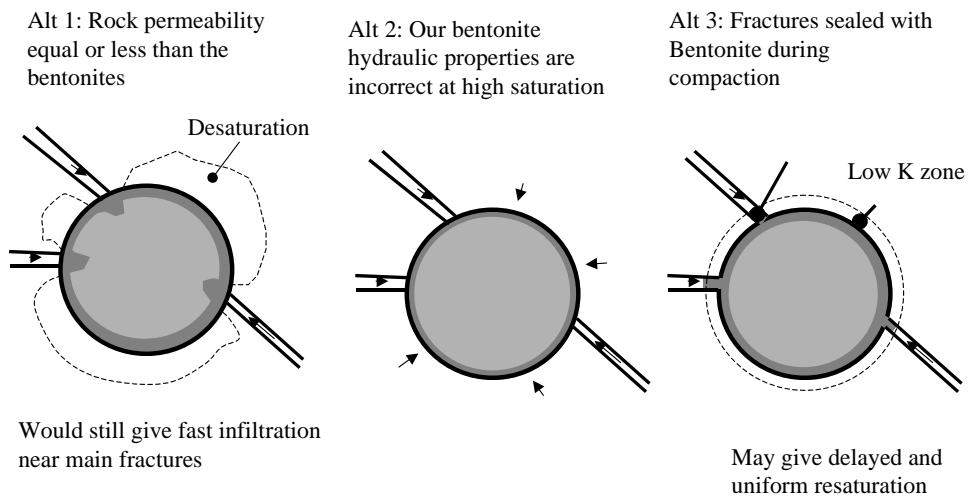


Figure 4.4: Three possible scenarios leading to a delayed wetting of the bentonite.

At the Kamaishi Mine heater test, the most obvious mismatch between predicted and observed responses is in the mechanical behavior of the buffer (Rutqvist et al., 1999 and 2001b). Although, both modeling and field results indicated a small swelling pressure, the prediction of tensile stresses near the heater is not satisfactory (Fig. 4.5). In the field experiment, the swelling pressure varies substantially depending on the location. However, the buffer appears to be in compression. Even in the dried part of the buffer, near the heater, the radial stress remains compressive.

In general, the stress in the buffer is a result of contributions from both hydromechanical and thermomechanical processes (Fig. 4.6). In the modeling of the Kamaishi Mine heater test, there were considerable uncertainties in the hydromechanical and thermo-mechanical properties of the bentonite. Therefore, the cause of the discrepancy in Fig. 4.5 could be sought in these properties. An improved hydromechanical relationship (swelling strain and swelling pressure) can be obtained from a shrinking laboratory test, which was not utilized during DECOLALEX II. Furthermore, the thermal expansion coefficient of the bentonite was not determined by an independent measurement, but was assumed to be $1 \cdot 10^{-6} \text{ }^\circ\text{C}^{-1}$, a value that appears to be low for this type of material. An increased thermal expansion coefficient would increase compressive stresses in the buffer during heating.

At the Kamaishi Mine heater test, the near field rock is highly fractured and at a low in situ stress. This leads to a very complex displacement and strain pattern in the rock, which could not be predicted in every point. However, both modeling and field experiments show that the displacement of the rock mass was small (less than 1 mm). Furthermore, the general thermal expansion of the rock was predicted reasonably well with the ROCMAS code (Figure 4.7). The slight over-estimation of the simulated thermal expansion can be explained by the fact that the thermal expansion coefficient of the rock mass was taken to be equal to its values for an intact rock material. Considering that the rock mass contains fractures, the thermal expansion coefficient should be reduced. The results in Figure 4.7 indicate that a thermal expansion coefficient of about 60% of the intact value would be appropriate.

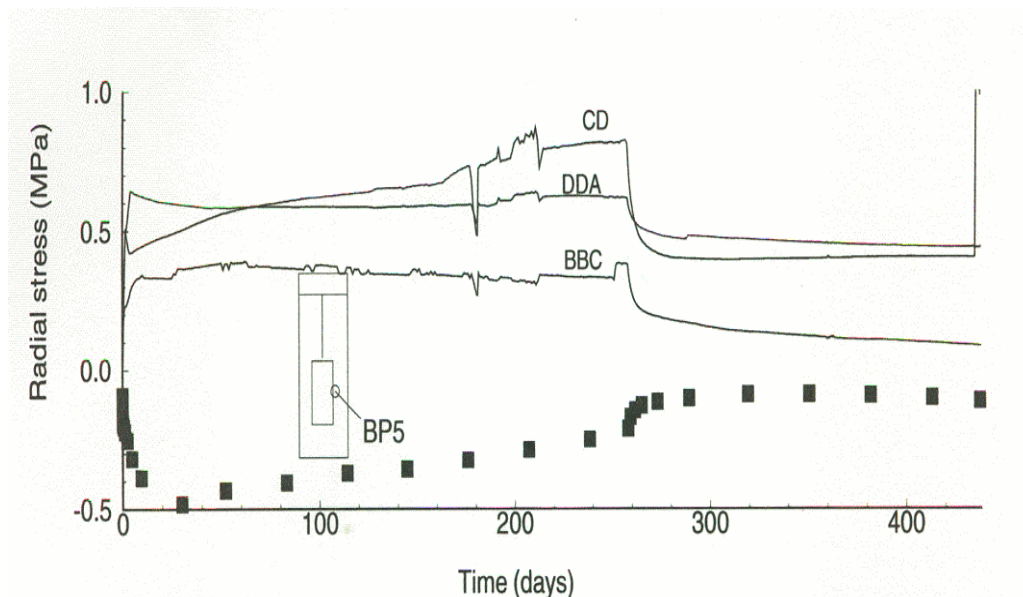


Figure 4.5: Result of previous modeling of the Kamaishi Mine heater test. Predicted (symbols) and observed (line) radial stresses in the buffer at the heater surface. Compressive stress is positive.

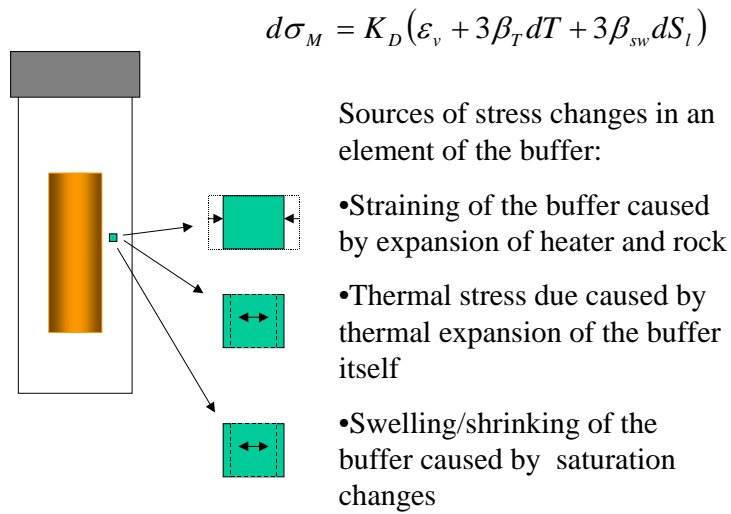


Figure 4.6: Different sources of causing a stress change in the buffer during the Kamaishi Mine heater test.

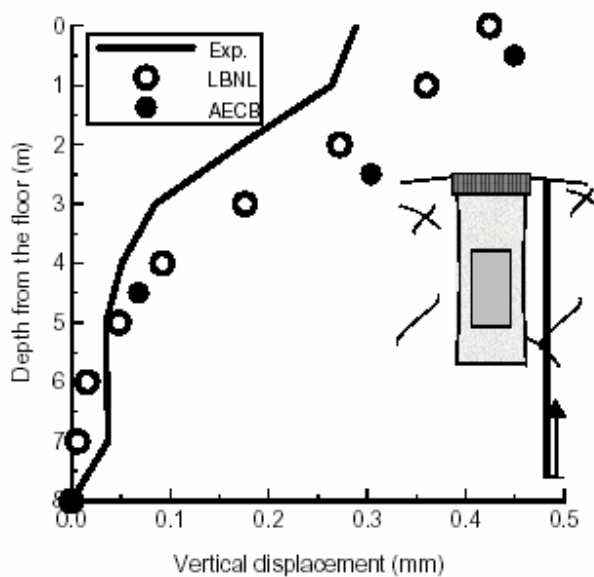
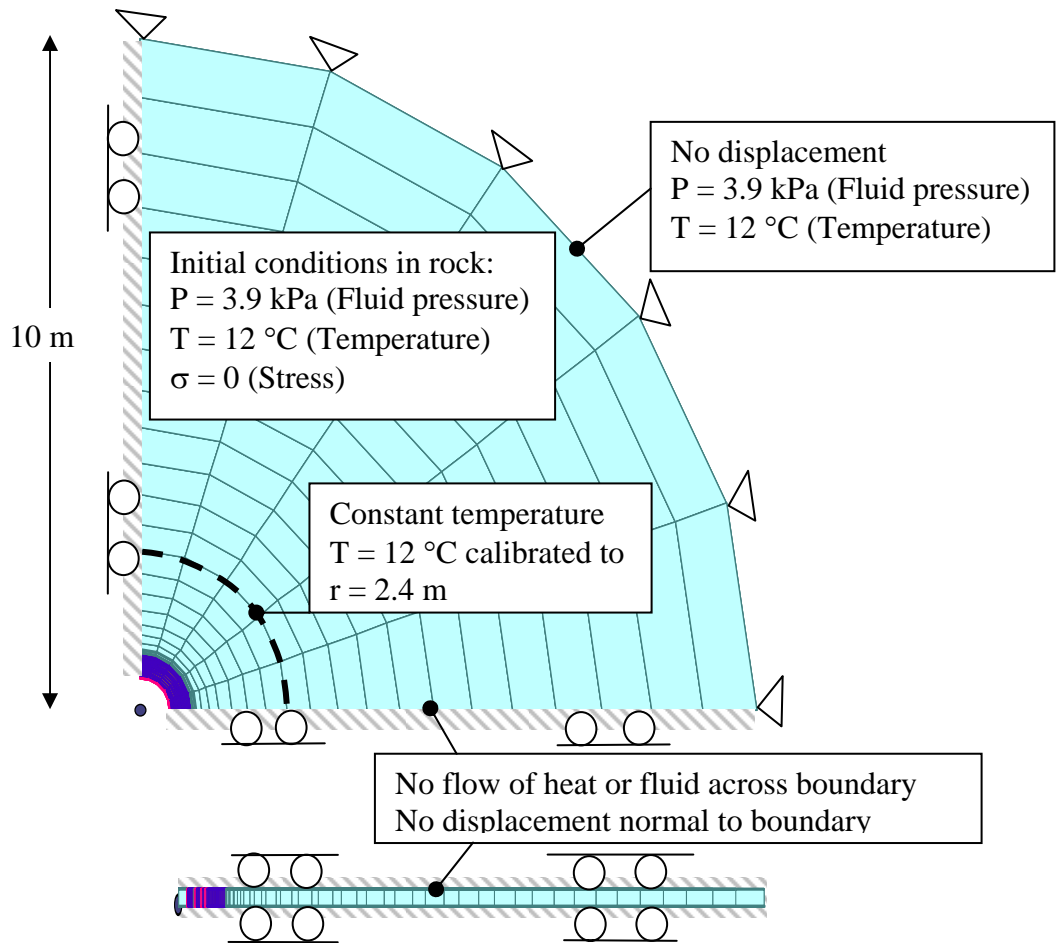


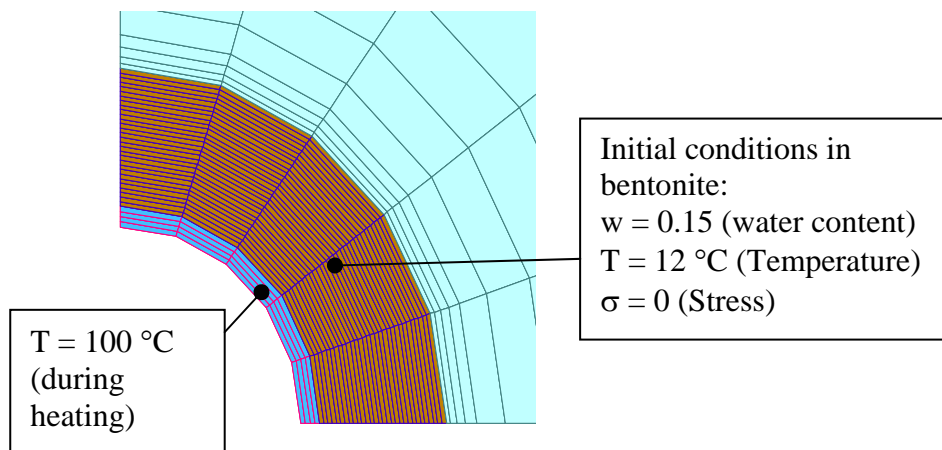
Figure 4.7: Result of previous modeling of the Kamaishi Mine heater test. Predicted (symbols) and observed (line) vertical displacement caused by the thermal expansion of the rock mass.

4.2 A simplified axisymmetric model of the Kamaishi Mine heater test

A simplified axisymmetric model is defined for a detailed study of the THM behavior along one radial line at mid elevation of the heater (cf. Fig. 1.18). The simulated results are compared to observation made at four points—three in the bentonite and one in the rock—located at different radial distances. The axisymmetric geometry is discretized into a three-dimensional symmetric finite element model for analysis with the ROCMAS code (Fig. 4.8). The ROCMAS code and its fundamental equations are described in Rutqvist et al (1999 and 2001b).



(a) Horizontal and vertical sections of the entire model



(b) Detail of heater and bentonite

Figure 4.8: Geometry, Boundary and initial conditions of the finite element model for analysis of the axisymmetric problem with ROCMAS.

In DECOVALEX II, the material properties for the bentonite, rock and heater at the Kamaishi Mine heater test were determined from various laboratory tests and model calibrations. The material properties that were used in the final prediction of the heater test in DECOVALEX II are given in Tables 4.2 and 4.3.

For the present axisymmetric model, the same properties are used with a few exceptions. The exceptions are:

Table 4.2: Material Properties of the Bentonite-Water System Determined from Laboratory Experiments and Used for Modeling of the Kamaishi Mine Heater Test.

Material	Parameter	Value	Source
Bentonite	Dry density, ρ_d [kg/m ³]	1.6·10 ³	Direct lab test ¹
	Saturated permeability, k_{wS} [m ²]	1.6·10 ⁻²⁰	Direct lab test ¹
	Relative permeability, k_r [-]	(Figure 9)	Modeling lab test ²
	Porosity, ϕ [-]	0.389	Direct lab test ¹
	Biot's effective stress parameter, α [-]	0.0	Modeling lab test ²
	Moisture swelling coefficient, ξ [-]	0.011	Modeling lab test ²
	Thermal expansion, β [1/°C]	1.0·10 ⁻⁶	Direct lab test ¹
	Young's Modulus, E [Gpa]	0.1	Direct lab test ¹
	Poisson ratio, ν [-]	0.3	PNC ³
	Dry specific heat, C_{vs} [J/kg·°C]	426	PNC ³
	Thermal conductivity, $K_m + LD_{Tv}$ [W/m·°C]	0.5+1.2·S	Direct lab test ¹
Fluid	Thermal expansion coefficient, β_T [1/°C]	4.0·10 ⁻⁴	Standard table ⁴
	Specific heat, C_{vw} [J/kg·°C]	4180	Standard table ⁴
	Viscosity, η_w [Ns/m ²] (at 25 °C)	1.070·10 ³	Standard table ⁴
	Compressibility, β_p [1/Pa]	4.4·10 ⁻¹⁰	Standard table ⁴
	Density, ρ_{w0} [kg/m ³] (at 25 °C)	997.0	Standard table ⁴
Vapor-air	Mass flow times tortousity factors, $\nu_v \times \tau_v$ [-]	0.67	Modeling lab test ²
	Thermal diffusion enhancement factor, f_{Tv} [-]	1.0	Modeling lab test ²
	Vapor specific heat, C_{vS} [J/kg·°C]	1900	Standard table ⁴
	Latent heat of vaporization, L_0 [J/kg]	2.4·10 ⁶	Standard table ⁴
	Specific gas constant of water vapor, R [J/kg°C]	461.5	Standard table ⁴

- 1) The parameter has been directly measured in a laboratory experiment and is reported in Fujita et al (1997) and Chijimatsu et al. (1996).
- 2) The parameter has been determined by modeling (using ROCMAS) of a laboratory experiment reported in Fujita et al., 1997.
- 3) The parameter has been given by PNC but has not been determined by the laboratory experiments reported in Fujita et al. (1997) and Chijimatsu et al. (1996).
- 4) The parameter is obtained from standard thermodynamic or thermophysical tables.

Table 4.3: Properties of Additional Materials for Modeling of the Kamaishi Mine Heater Test.

Material	Parameter	Value	Source
Rock	Density, ρ_s [kg/m ³]	2700	Direct lab test ¹
	Porosity, ϕ [-]	0.03	Direct lab test ¹
	Biot's effective stress parameter, α [-]	1.0	Assumed ²
	Wet specific heat, C_v [J/kg·°C]	833	Direct lab test ¹
	Thermal conductivity, K_m [W/m·°C]	2.7	Direct lab test ¹
	Thermal expansion, β [1/°C]	$8.21 \cdot 10^{-6}$	Direct lab test ¹
	Hydraulic permeability, k [m ²]	$1.0 \cdot 10^{-17}$	Modeling field test ⁴
Heater and heater guide	Density, ρ_s [kg/m ³]	7800	PNC ³
	Hydraulic permeability, k_w [m ²]	$1.0 \cdot 10^{-27}$	PNC ³
	Porosity, ϕ [-]	$1.0 \cdot 10^{-4}$	PNC ³
	Young's modulus, E [GPa]	200	PNC ³
	Poisson's ratio, ν [-]	0.3	PNC ³
	Biot's effective stress parameter, α [-]	1.0	Assumed ²
	Wet specific heat, C_v [J/kg·°C]	750	PNC ³
	Thermal conductivity, K_m [W/m·°C]	100.0	PNC ³
	Thermal expansion coefficient, β [1/°C]	$1.64 \cdot 10^{-6}$	PNC ³

- 1) The parameter has been directly measured in a laboratory experiment and is reported in Fujita et al (1997) and Chijimatsu *et al.* (1996).
- 2) The parameter has been assumed to a reasonable value.
- 3) The parameter has been given by PNC but has not been determined by the laboratory experiments reported in Fujita *et al.* (1997) and Chijimatsu *et al.* (1996).
- 4) The parameter was determined by a model calibration against field data Rutqvist *et al.*, (1999).

- The coefficient of swelling in the bentonite is changed to an improved bi-linear function obtained from a shrinking test of a bentonite sample (Fig. 4.9).
- The coefficient of linear thermal expansion of the bentonite is increased from $1.0 \cdot 10^{-6}$ to $3.0 \cdot 10^{-5} \text{ } ^\circ\text{C}^{-1}$.
- The hydraulic permeability of the rock mass is decreased by one order of magnitude to reduce the rate of infiltration from the rock mass into the bentonite.

The thermal expansion coefficient of the Kamaishi Mine bentonite (denoted OT-9607) was not independently determined in a laboratory experiment. In the previous modeling, it was assumed to be $1.0 \cdot 10^{-6} \text{ } ^\circ\text{C}^{-1}$, a value that appears to be low for this type of material. The new value of $3.0 \cdot 10^{-5} \text{ } ^\circ\text{C}^{-1}$ used in this simulation is obtained by a model calibration with matching to observed buffer stress and strain.

A hydraulic permeability of the rock mass of $5 \cdot 10^{-19} \text{ m}^2$ was first determined by a calibration of the evolution of the water content in monitoring point BW1 (Fig. 4.10). However, for the modeling of the heater test, a rock permeability of $1 \cdot 10^{-18} \text{ m}^2$ (or higher) matches the evolution of the water content at the rock interface on the mid heater level section. That is, the new rock permeability is decreased about 1 order of magnitude.

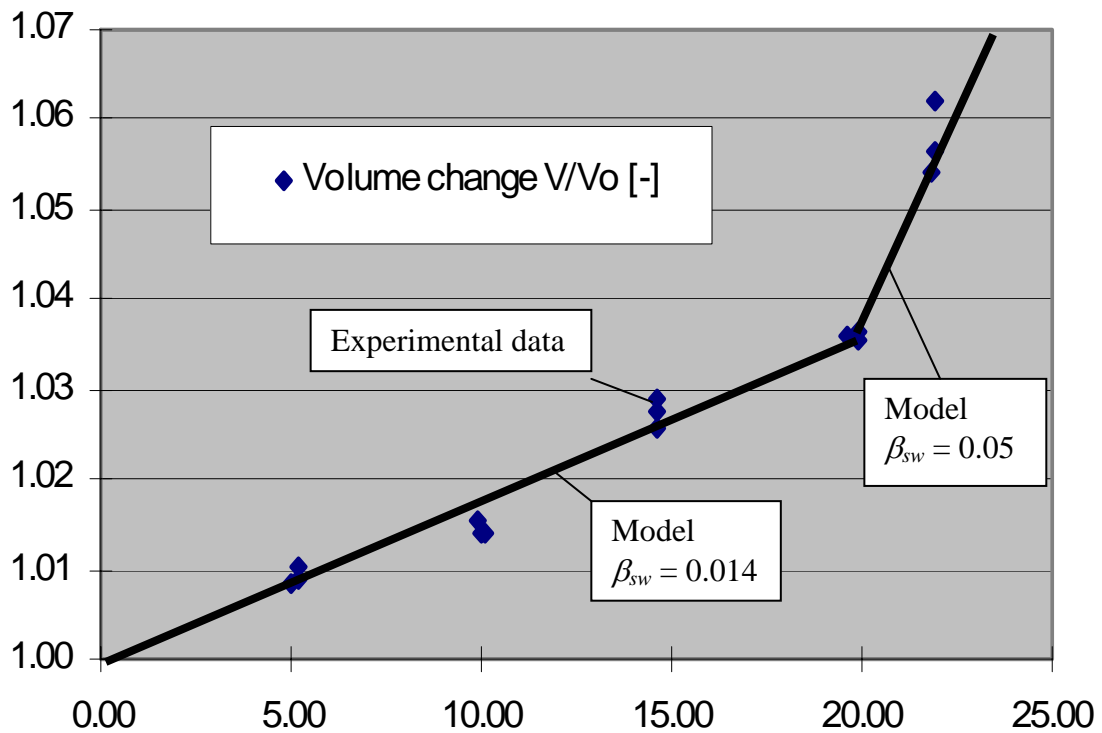


Figure 4.9: Experimental data of a shrinking test on OT-9697 bentonite mix and a new bi-linear relationship with two different coefficients of swelling.

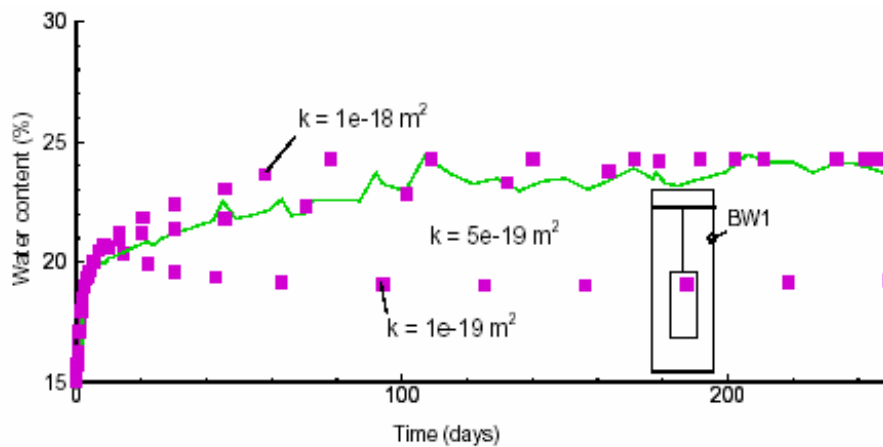


Figure 4.10: Results of a model calibration to match the observed response of water content in the buffer at monitoring point BW1.

4.3 Results of axisymmetric modeling of the heater test

The heater test is simulated in the axisymmetric model by applying the constant temperature of 100 °C at the inner surface of the steel heater for 8.5 month. After 8.5 month, the constant temperature boundary constraint on the heater is released and the temperature can fall freely. The outer boundary of the model is defined to be located at 10 meters (cf. Fig. 4.7). However, in order to match the observed temperature field, the

constant temperature boundary had to be applied considerable closer to the heat source. The reason for the close constant temperature boundary is that the temperature in the field is affected by the nearby constant temperature at the water pool on the floor of the test drift. In this model the constant temperature boundary was calibrated to be located at a radius of 2.4 meters (cf. Fig. 4.8).

Figures 4.11 to 4.13 present results from simulation in a profile along the radial distance from the center of the axisymmetric model. Fig. 4.11 shows that the temperature rises quickly and becomes almost steady within 10 days. Thereafter, between 10 days and 8.5 month, the temperature decreases slightly because the bentonite's thermal conductivity depends on its water content. Near the heater, the high temperature gives rise to evaporation of liquid into vapor and accompanying drying of the bentonite. This vapor is transported along the thermal gradient towards cooler regions where it is condensed into liquid water again. At the rock/bentonite interface, the water content rises quickly to full saturation and the bentonite is gradually wetted from the rock mass. During cooling, the thermal gradient force on the vapor flow is lost. Consequently, the water content rebounds in the dry areas near the heater by a liquid flow from the wet outer areas.

Figure 4.12 presents the total stress in the tangential and radial direction. After 1 day, there is a general compressive stress increases, which is caused by thermal expansion of the bentonite. After 10 days, the compressive stress has been increased further in response to the increased temperature. At the same time, the effects of drying and wetting can be seen at both ends of the curves (at 1 and 10 days in Fig. 4.12). In general, the tangential stress is correlated to the water content in Fig. 4.12, with increased compressive stress in the wetted areas and reduced compressive stresses and some tensile stresses in the dried areas. While the tangential stress varies from high compression at the rock wall to tension at the heater, the radial stress tends to be more uniformly distributed and stays compressive all time.

Figure 4.13 shows a general pattern with an expanding bentonite in the outer wetted areas and a shrinking bentonite in the inner dried areas. Because the bentonite is partially constrained (fully constrained in the tangential direction and partially constrained in the radial direction) it is prevented to fully expand and contract. Such constraint is leading the increases compressive stress in wetted areas and induced tension in dried areas.

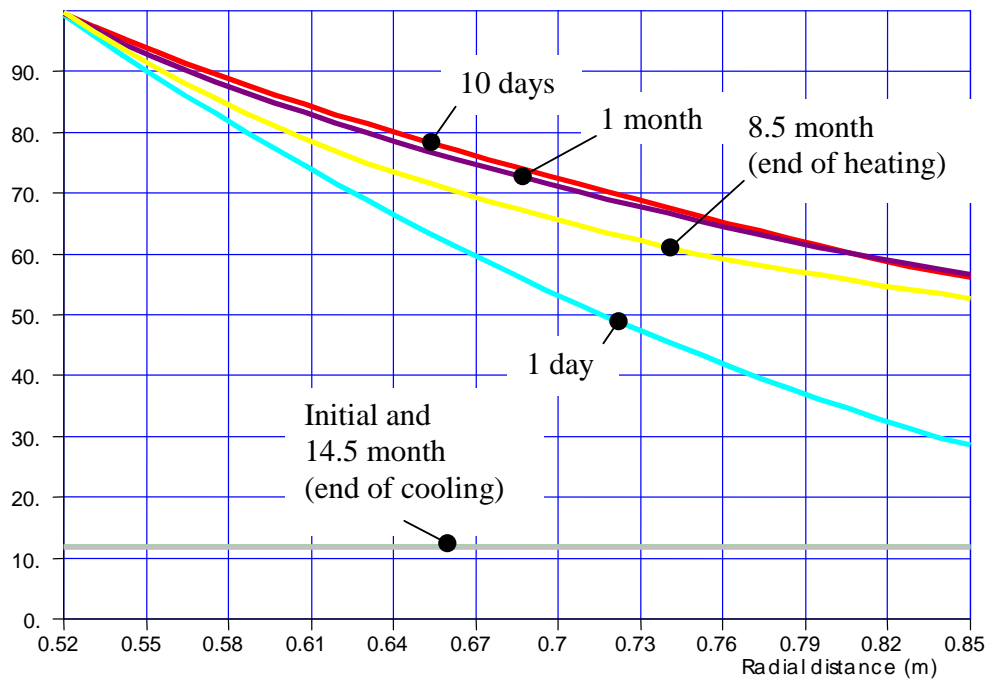
4.4 Comparison of axisymmetric modeling to field observations

The simulated and observed temperatures at the four output points are compared in Figure 4.14. In general, the temperature matches well except during initiation of heating and cooling phases. The temperature responds much faster in the model than in the field. Such discrepancy did not occur in DECOVALEX II were the problem was simulated using a full three-dimensional model. Thus, it appears that the rapid temperature increases is caused by the geometrical simplification of the problem, which apparently leads to a smaller mass of heat capacity.

The simulated water content matched the observed one reasonable well (Fig. 4.15) and the general responses are similar to those obtained with the full three-dimensional modeling in DECOVALEX II. Near the heater (PT1), the bentonite is dried during heating down to water content of a few percent. During the cooling the water content in PT1 recovers partially. However, still after six months of cooling, the water content is

lower than its initial value. At mid distance between the heat and the rock (PT2), the bentonite is temporarily wetted during the first few month. This temporal wetting was also observed in the modeling with ROCMAS code in DECOVALEX II and is due to condensation of vapor that have been transported from the inner hot regions of the bentonite buffer.

Temperature °C



Saturation

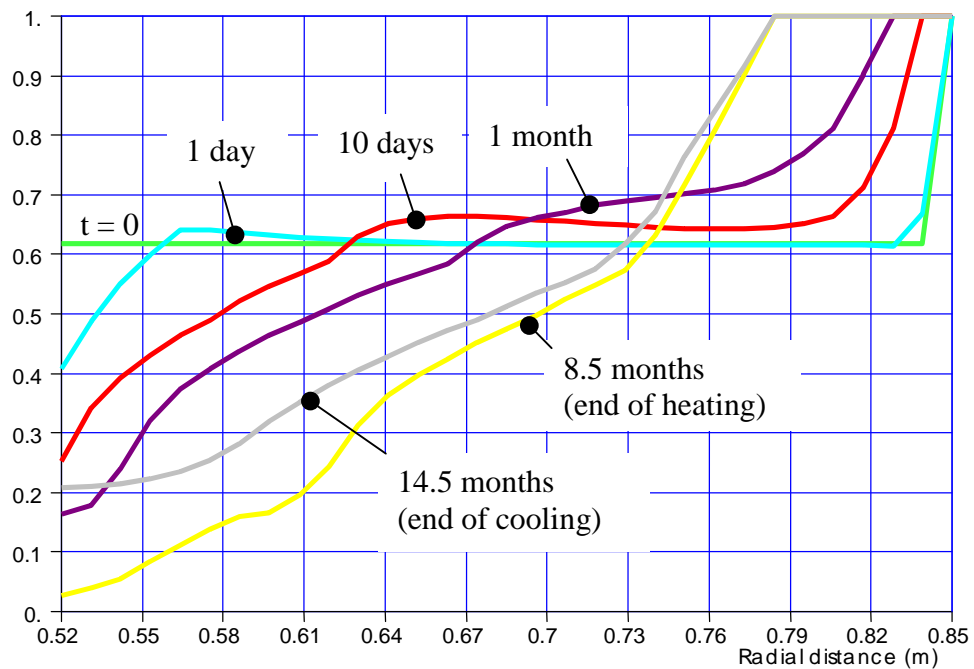


Figure 4.11: Calculated results of temperature and saturation across the bentonite buffer.

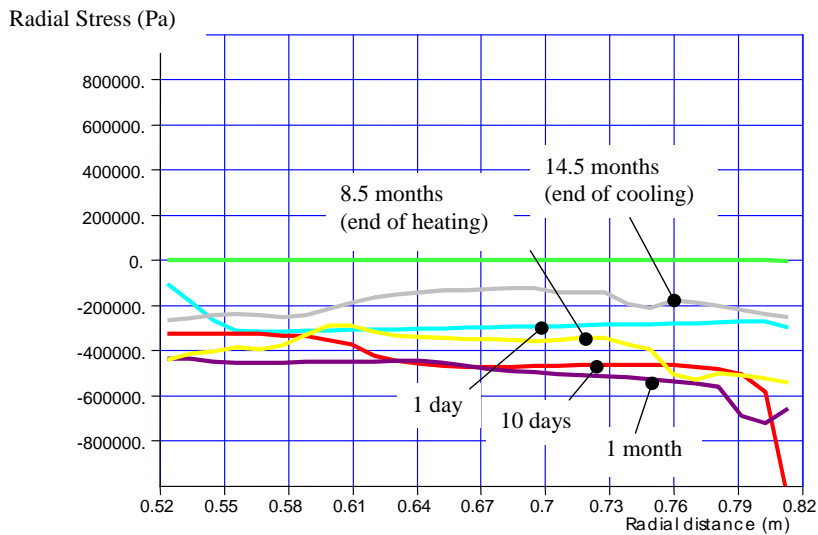
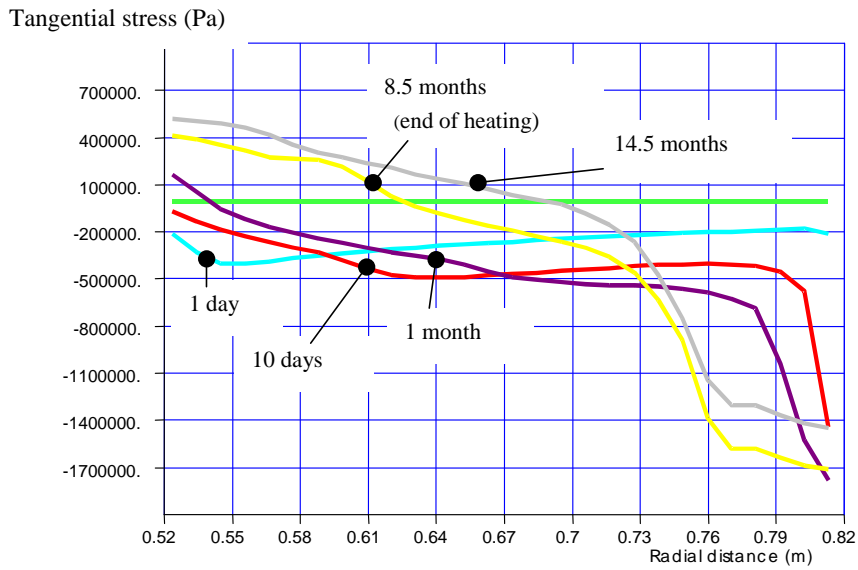


Figure 4.12: Calculated results of tangential and radial stress in the bentonite buffer.

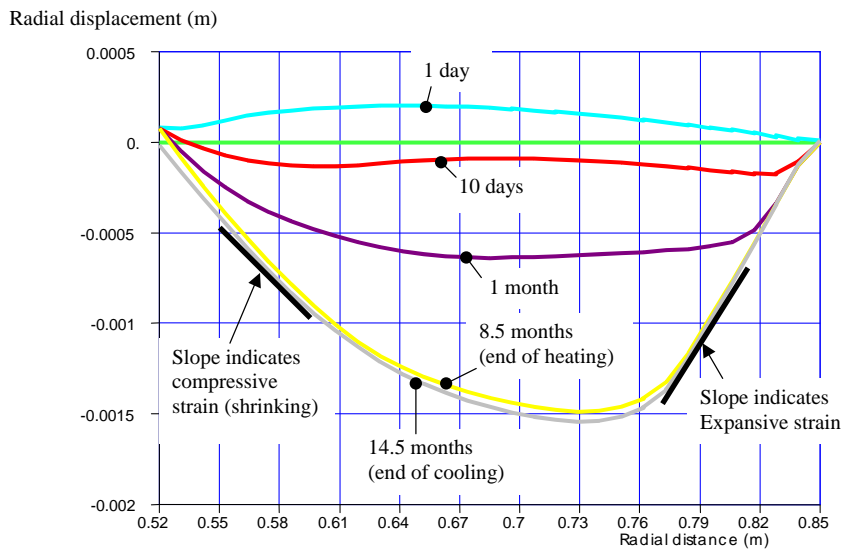


Figure 4.13: Radial displacement in the bentonite buffer. The radial strain is equivalent to the slope du/dr .

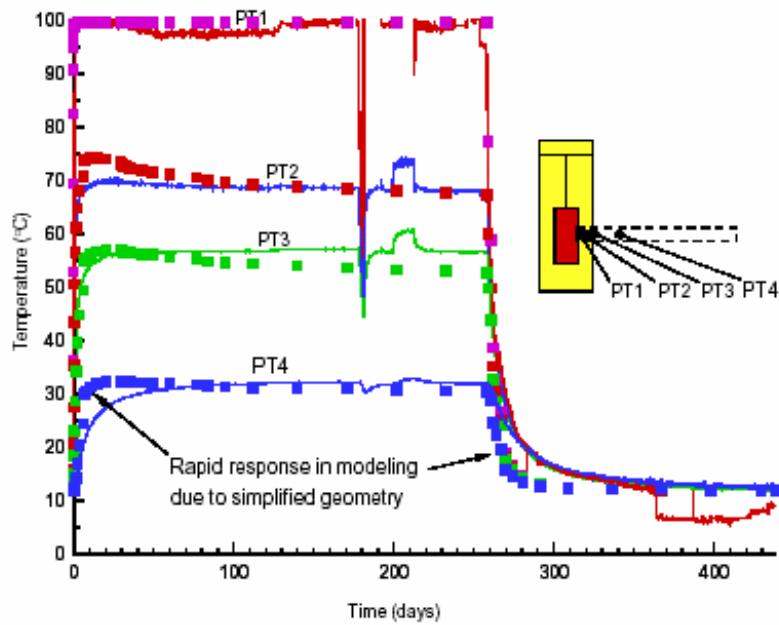


Figure 4.14: Temperature history at four selected points. Comparison of experimental results (lines) and axisymmetric modeling with ROCMAS (symbols).

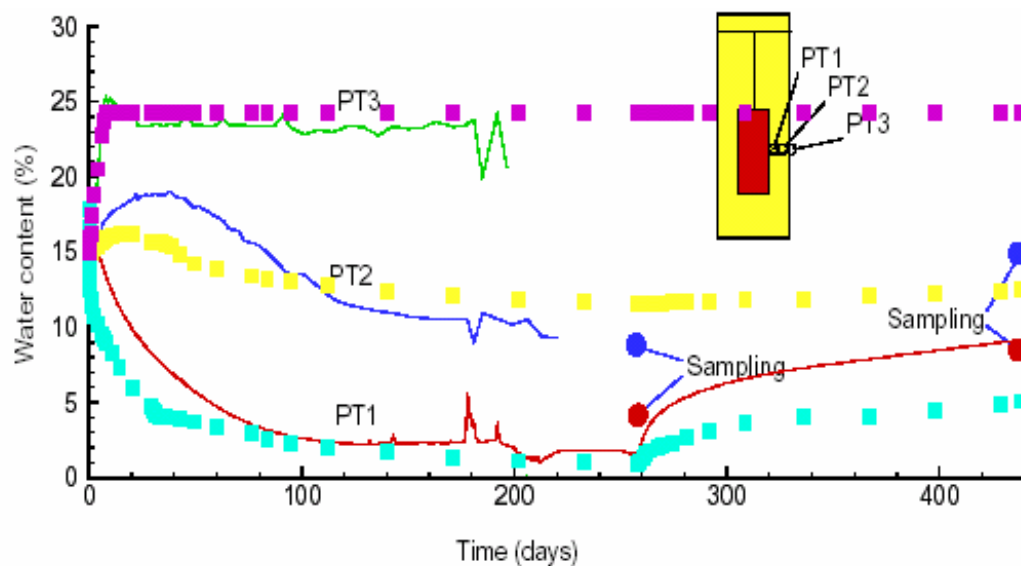


Figure 4.15: History of water content at 3 points. Comparison of experimental results (lines) and axisymmetric modeling with ROCMAS (symbols).

The mechanical behavior can be compared in two points in the buffer. In PT1, the radial stress was monitored with a pressure cell, and in PT2, the radial strain was measured with a strain gauge. Figures 4.16 and 4.17 shows that the simulation captures the general responses observed in the field. The stress initially increases almost immediately due to the thermal expansion of the heater, bentonite and rock (Fig. 4.16). Thereafter, the wetting and drying of the bentonite cause further stress increase. After the heater turn-off (258 days), the radial stress drops rapidly due to cooling shrinkage. At the end of the test (438 days) the stress is still compressive due to a net swelling stress in the buffer. The strain in the midsection of the buffer (PT2), is initially rapidly

compressed, then expanded during the first month, and finally compressed during the rest of the experiment (Fig. 4.17). The temporal wetting that can be seen in Fig. 4.15 causes the temporal expansion during the first month. However, it is a complex system because the strain is not only affected by the local water content, but also by the wetting and drying in other part of the buffer.

Figure 4.18 presents a comparison of the simulated radial stress evolution in PT1 with and without the consideration of the thermal expansion of the bentonite. It clearly shows that the thermal expansion rapidly develop thermal compressive stresses in the buffer which completely disappear after cooling. On the other hand, Fig. 4.19 shows that the local strain at PT2 is almost exclusively caused by moisture swelling and shrinkage while the thermal expansion have little effect.

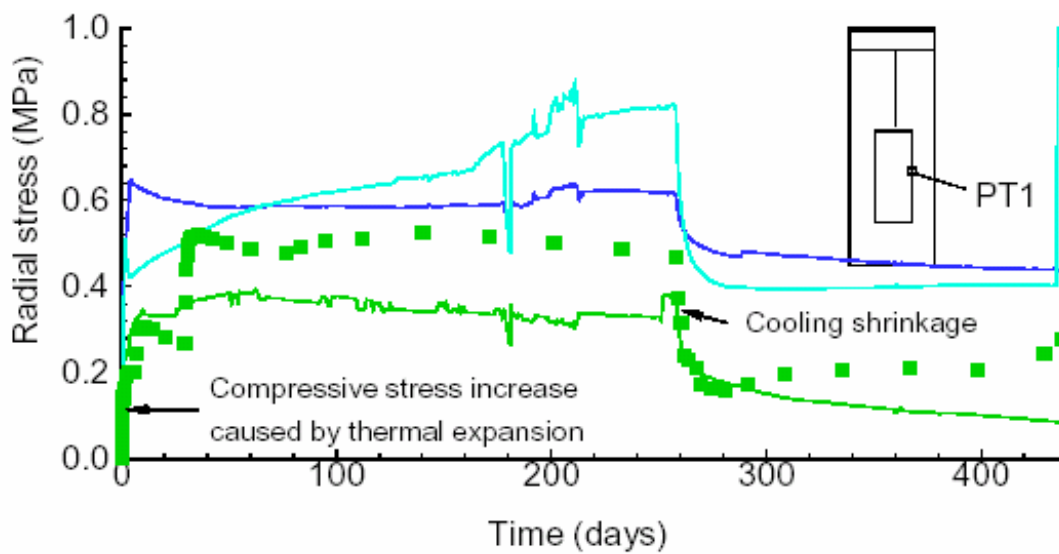


Figure 4.16: History of radial strain in the buffer at point pt2. Comparison of experimental results (lines) and axisymmetric modeling with ROCMAS (symbols).

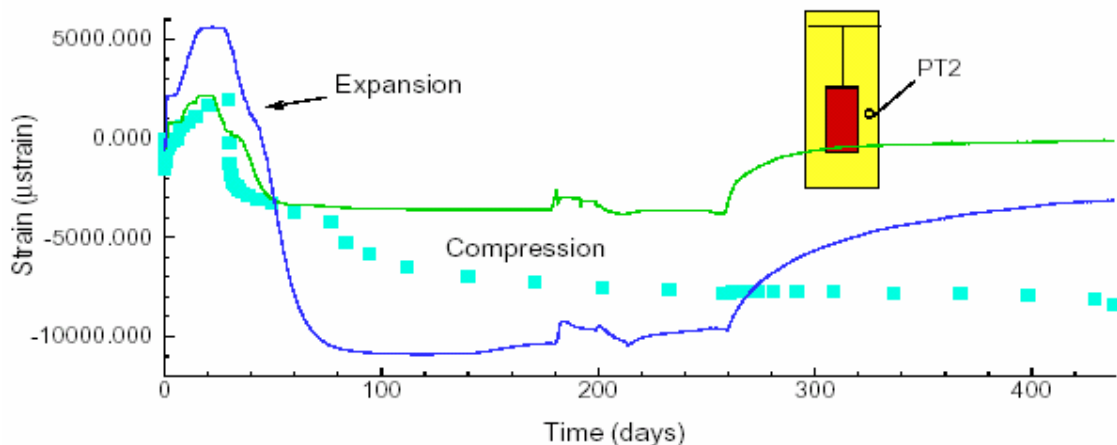


Figure 4.17: History of radial stress in the buffer at point pt1. Comparison of experimental results (lines) and axisymmetric modeling with ROCMAS (symbols).

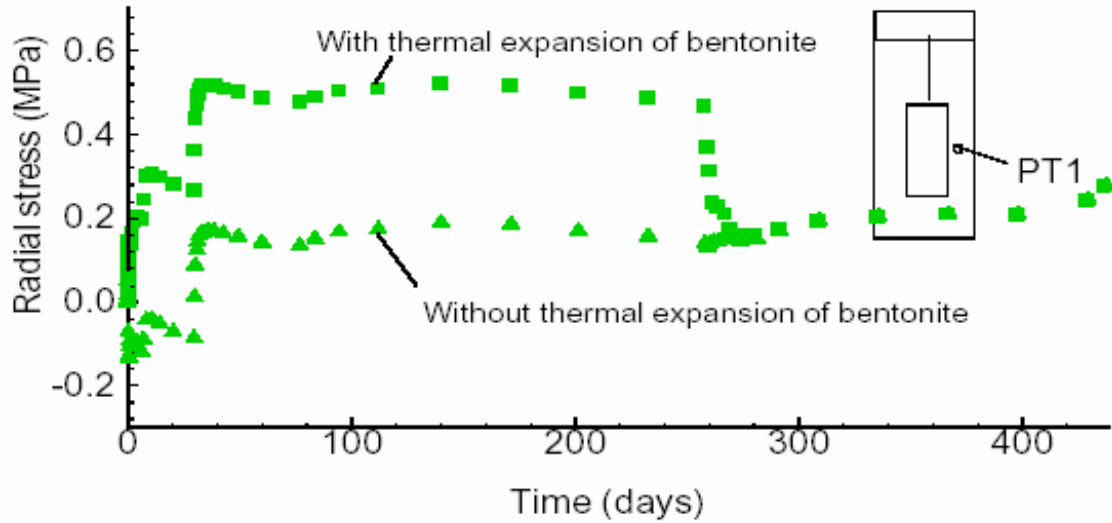


Figure 4.18: History of radial stress in the buffer at point PT1 for comparison of modeling results with and without thermal expansion of the bentonite.

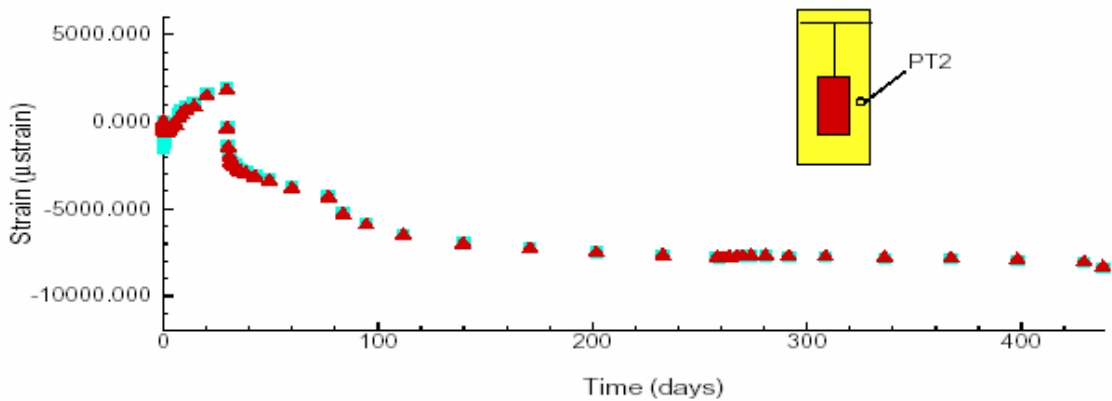


Figure 4.19: History of radial strain in the buffer at point pt2. Comparison of modeling results with and without thermal expansion of the bentonite.

In general, many contributing forces affect the mechanical behavior of the bentonite buffer. The thermal expansion of the bentonite appears to be important for the stress and also helps to prevent tensile stresses from developing. This is important because high tensile stresses may cause fracturing of the bentonite. It should also be pointed out that the simplified axisymmetric model used in this simulation prevents movement in the vertical direction. In the field, on the other hand, the bentonite expanded slightly (about 2000 μ s) in the vertical direction during the heating phase. This would also affect the stress and strain in the radial direction.

4.5 Summary and conclusions of KTH/SKI work

A number of improvements to the modeling of the Kamaishi Mine heater test were suggested and tested in this study. The suggested improvements were tested using a simplified axisymmetric model of the heater test. Although the model geometry is

much simplified to the field test environment, the observed general THM responses were well captured in the simulations. The following improvements were suggested and tested:

- A reduced rock mass permeability captures the delayed wetting of the bentonite near the rock wall. In addition the sealing of rock fractures by penetrating bentonite can explain the uniform (axisymmetric) wetting of the bentonite.
- A reduced rock mass thermal expansion coefficient (compared to its value for intact rock) will better match the thermal expansion of the rock mass.
- An improved swelling/shrinking strain function combined with an increased thermal expansion of the bentonite gave a good match of the mechanical (stress, strain) behavior of the buffer.

In general, the mechanical behavior of the buffer is complex with forces contributing from shrinking/swelling in all part of the bentonite, external stress from the thermal expansion of the heater and rock, and internal thermal expansion of the bentonite itself. However, a reasonable prediction of the mechanical behavior can be done if all relevant bentonite properties are known from laboratory test.

5. Evaluation of the Kamaishi mine modelling – The ANDRA/INERIS team studies

5.1 Introduction

In this study, the works performed by INERIS team on the first phase of BMT1, BMT1-A, is presented. Modelling was performed using the new two-phase flow option of FLAC. The objective is to evaluate the modelling of the Kamaishi Mine heater test, using FLAC.

In this first version of two-phase flow in FLAC code, unsaturated media with two pressures (liquid and gas) can be modelled. However, phase changes and axisymmetric configuration are not implemented. Summarized constitutive equations of the two-phase flow in FLAC will be presented.

Results presented herein consist of the first evaluation of the modelling of the Kamaishi Mine heater test performed with FLAC. The confidence on the modelling tool and results will be further examined.

5.2 Governing Equations

The two-phase flow option in *FLAC* allows numerical modelling of the flow of two immiscible fluids through porous media. A description of the concepts involved in the mathematical description of multi-phase flow may be found in reference books such as “Fundamentals of Numerical Reservoir Simulation” (Donald W. Peaceman 1977). Some of these concepts are addressed below.

In two-phase flow, the void space is completely filled by the two fluids. One of the fluids (the liquid fluid, identified by the subscript lq) wets the porous medium more than the other (the gas fluid, identified by subscript gz). As a result, the pressure in the non-wetting fluid will be higher than the pressure in the wetting fluid. The pressure difference $P_{gz} - P_{lq}$ is the capillary pressure P_c , which is a function of saturation S_{lq} . Darcy’s law is used to describe the flow of each fluid. The effective intrinsic permeability in the law is given as a fraction of the single-fluid (or saturated) intrinsic permeability. The fractions (or relative permeability) are functions of saturation, S_{lq} . In the *FLAC* implementation, the curves for capillary pressure and relative permeability are built-in empirical laws of the van Genuchten form (van Genuchten 1980).

In addition to the mechanical balance of momentum, the mechanical constitutive equations and compatibility equation, the additional equations are used for coupled calculations.

5.2.1 Transport equations

The transport equations of liquid and gas components are described by the Darcy’s law:

$$\begin{cases} q_i^{lq} = -k_{ij}^{lq} \kappa_r^{lq} \frac{\partial}{\partial x_j} (P_{lq} - \rho_{lq} g_k x_k) \\ q_i^{gz} = -k_{ij}^{lq} \kappa_r^{gz} \frac{\partial}{\partial x_j} (P_{gz} - \rho_{gz} g_k x_k) \end{cases} \quad (5.1)$$

where k_{ij} is saturated mobility coefficient, which is a tensor, κ_r is relative permeability for the fluid, which is a function of liquid saturation S_{lq} , μ is dynamic viscosity, P is pore pressure, ρ is fluid density, and g is gravity.

5.2.2 Relative permeability laws

Relative permeability are related to the liquid saturation S_{lq} by the empirical laws of the van Genuchten (van Genuchten 1980) and expressed as follows :

$$\begin{cases} k_r^{lq} = S_e^b \left[1 - (1 - S_e^{1/a})^a \right]^2 \\ k_r^{gz} = (1 - S_e)^c \left[1 - S_e^{1/a} \right]^{2a} \end{cases} \quad (5.2)$$

In these relations, a , b and c are material constants to be identified from the experimental curve of sorption, S_e is the effective saturation defined by :

$$S_e = \frac{S_{lq} - S_{lq}^r}{1 - S_{lq}^r} \quad (5.3)$$

where S_{lq}^r is residual liquid saturation (the residual liquid saturation, which remains in spite of high values of capillary pressure which is expressed by $P_c = P_{gz} - P_{lq}$). The evolution of capillary pressure with respect to the liquid saturation is based on the empirical law is of the van Genuchten :

$$P_c(S_{lq}) = P_0 \left[S_e^{-1/a} - 1 \right]^{1-a} \quad (5.4)$$

where P_0 is a parameter depending on the material properties.

5.2.3 Constitutive relations

For slightly compressible fluids, the balance relations are :

$$\begin{cases} \frac{\partial \zeta_{lq}}{\partial t} = -\frac{\partial q_i^{lq}}{\partial t} + q_v^{lq} \\ \frac{\partial \zeta_{gz}}{\partial t} = -\frac{\partial q_i^{gz}}{\partial t} + q_v^{gz} \end{cases} \quad (5.5)$$

where ζ is the variation of fluid content (variation of fluid volume per unit volume of porous material), and q_v is the volumetric fluid source intensity.

The constitutive equations of fluid components are :

$$\begin{cases} S_{lq} \frac{\partial P_{lq}}{\partial t} = -\frac{K_{lq}}{\phi} \left[\frac{\partial \zeta_{lq}}{\partial t} - \phi \frac{\partial S_{lq}}{\partial t} - S_{lq} \frac{\partial \varepsilon}{\partial t} \right] \\ S_{gz} \frac{\partial P_{gz}}{\partial t} = -\frac{K_{gz}}{\phi} \left[\frac{\partial \zeta_{gz}}{\partial t} - \phi \frac{\partial S_{gz}}{\partial t} - S_{lq} \frac{\partial \varepsilon}{\partial t} \right] \end{cases} \quad (5.6)$$

where K_{lq} , K_{gz} are liquid and gas bulk modules, and ε is volumetric strain.

Substituting (5.5) in (5.6), and some rearrangement of terms, leads to:

$$\begin{cases} S_{lq} \frac{\partial P_{lq}}{\partial t} = -\frac{K_{lq}}{\phi} \left[\frac{\partial \zeta_{lq}}{\partial t} - \phi \frac{\partial S_{lq}}{\partial t} - S_{lq} \frac{\partial \varepsilon}{\partial t} \right] \\ S_{gz} \frac{\partial P_{gz}}{\partial t} = -\frac{K_{gz}}{\phi} \left[\frac{\partial \zeta_{gz}}{\partial t} - \phi \frac{\partial S_{gz}}{\partial t} - S_{lq} \frac{\partial \varepsilon}{\partial t} \right] \end{cases} \quad (5.7)$$

In a fluid-only calculation, the term $\partial \square / \partial t$ is omitted, combination of (5.7), and saturation and capillary pressure equations (eq.5. 8) form a non-linear system of four equations which needs to be solved for the four unknowns, P_{lq} , P_{gz} , S_{lq} and S_{gz} .

$$\begin{cases} S_{lq} + S_{gz} = 1 \\ P_{gz} - P_{lq} = P_c(S_{lq}) \end{cases} \quad (5.8)$$

5.3 Results of 1D-Axisymmetric Model

Note that the two-phase flow calculation is not actually available in axisymmetry configuration. Then the two-dimensional plane strain geometry is used to model the problem.

5.3.1 Geometry and material properties

The geometry of the 2D-plane strain problem as well as the initial and boundary conditions are shown in Fig. 5.1, according to the general problem definition, except the outer boundary of the model concerning the temperature boundary condition. When we have turned out the model with the boundary conditions given in the general problem definition ($T=12^\circ\text{C}$ at 10 m), the temperature at the rock/bentonite interface becomes about 70 degrees at the steady state. This is higher than the 55 degrees obtained in the Kamaishi heater test or in the simulations of other teams (LNBL, etc.). In order to match the observed field temperature, the constant temperature boundary had been applied closer to the heat source. Then, we have adjusted the radius of the constant temperature boundary in order to correct thermal gradient over the bentonite.

The material properties for the rock mass, bentonite and steel used in this first prediction are given in Table 5.1. Additional parameters associated to the empirical laws of van Genuchten [eqs. 4] are summarized in Tables 5.2 and 5.3. The corresponding parameters of bentonite have been adjusted from the experimental water retention curve of bentonite (Kunigel OT-9607), whereas for rock mass, parameters

were adjusted based on Figure Fig. 52b [JNC report]. Figures. 5.3 and 5.4 show the van Genuchten models for the bentonite and rock mass used in this study. It was assumed that the water retention curve of steel is identical to the bentonite ones.

It should be noted that the intrinsic permeability of steel-heater in the problem definition is about $1\text{E-}24 \text{ m}^2$. Simulations performed based on this value leads to a significant under-estimation of bentonite desaturation in the vicinity of steel-heater/bentonite interface, and resaturation of bentonite in vicinity of heater during the cooling phase. Then for this simulation a value of $2\text{E-}20 \text{ m}^2$ is assumed.

Table 5.1: Material properties for modelling the Kamaishi Mine heater test

Material	Property	Value
Bentonite	Dry density (kg/m^3)	1650
	Porosity (-)	0.389
	Young modulus (Pa)	0.1E9
	Poisson's ratio	0.3
	Thermal expansion ($1/^\circ\text{C}$)	1E-6
	Thermal conductivity ($\text{W/m}^\circ\text{K}$)	1.263
	Specific heat capacity ($\text{J/kg}^\circ\text{C}$)	426
	Initial water content (%), \square	15
	Initial saturation,	0.6362
Intrinsic permeability (m^2)	2E-19	
Rock mass	Density (kg/m^3)	2746
	Porosity (-)	0.00379
	Young modulus (Pa)	61E9
	Poisson's ratio	0.303
	Uniaxial compressive strength (Pa)	123E6
	Tensile strength (Pa)	11E6
	Friction ($^\circ$)	51.84
	Cohesion (Pa)	21.89E6
	Hoek-Brown parameter, m	17.5
	Hoek-Brown parameter, s	0.19
	Thermal expansion ($1/^\circ\text{C}$)	8.21E-6
	Thermal conductivity ($\text{W/m}^\circ\text{C}$)	2.71
	Intrinsic permeability (m^2)	1.98E-18
Steel heater	Density (kg/m^3)	7800
	Porosity	1E-4
	Young modulus (Pa)	200E9
	Poisson's ratio	0.3
	Thermal expansion ($1/^\circ\text{C}$)	1.64E-6
	Thermal conductivity ($\text{W/m}^\circ\text{C}$)	53
	Specific heat capacity ($\text{J/kg}^\circ\text{C}$)	460
Intrinsic permeability (m^2)	2E-20	

Table 5.2: van Genuchten model parameters of bentonite and rock mass

van Genuchten parameter	Bentonite	Rock mass
P_0 (Pa)	6.54E6	1E6
A	0.444	0.546
b	0.5	0.3
c	0.5	0.5

Table 5.3: Additional parameters

Parameter	Value
-----------	-------

Water density (kg/m ³)	1000
Water bulk modulus (Pa)	2E9
Water dynamic viscosity (Pa s)	1.01E-3
Gas density (kg/m ³)	1
Gas bulk modulus (Pa)	2E6

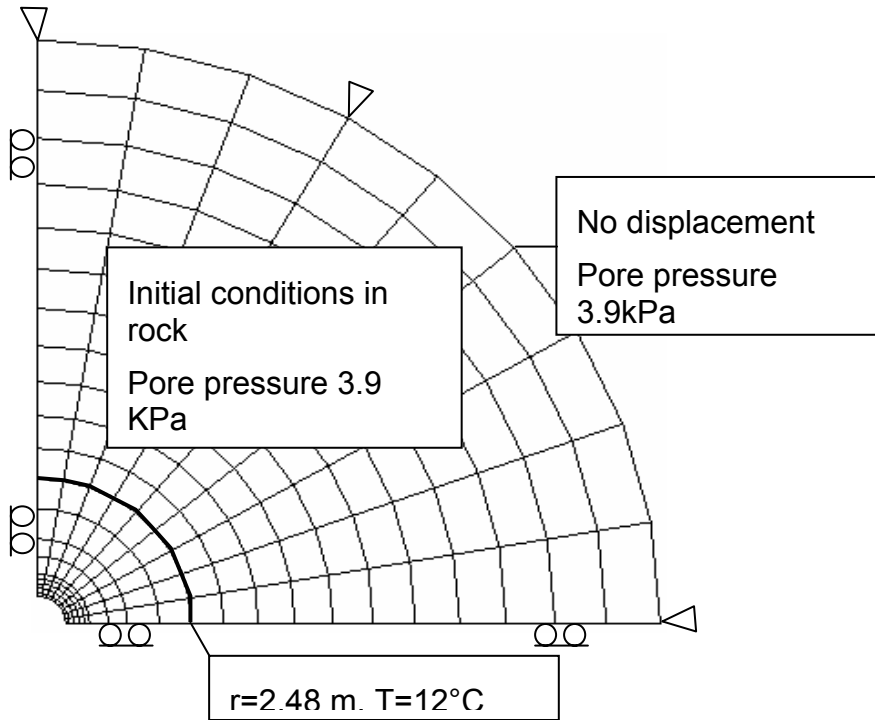


Figure 5.1: Geometry, boundary and initial conditions for the axis-symmetric model with FLAC code.

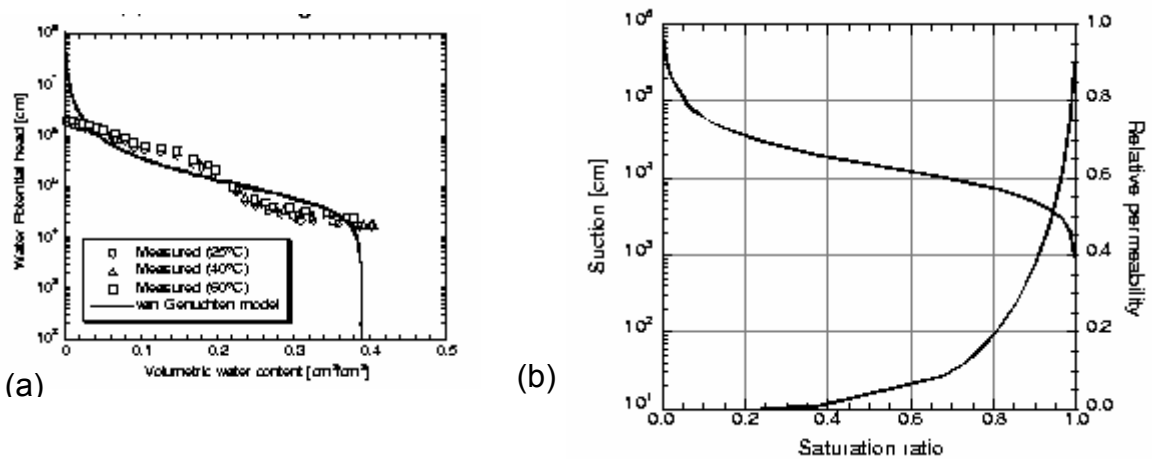


Figure 5.2: Water retention curves: a) Bentonite (Kunigel OT-9607); b) recommended rock mass water retention curve.

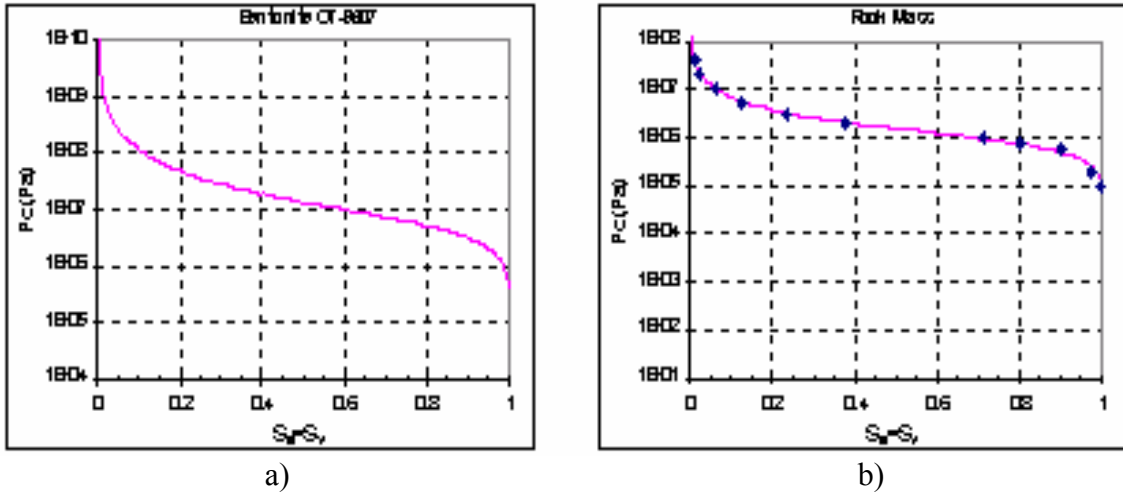


Figure 5.3: van Genuchten model of capillary pressure: a) Bentonite (Kunigel OT-9607); b) rock mass.

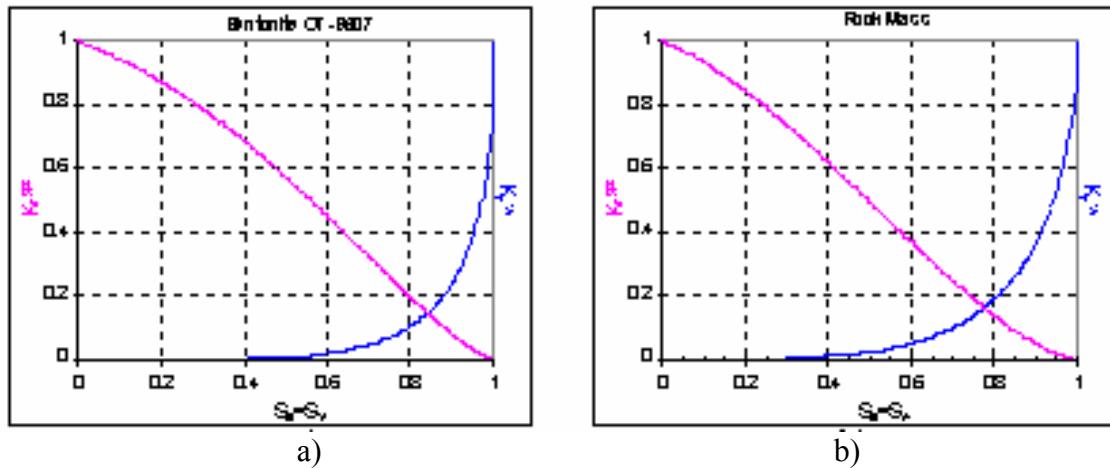


Figure 5.4: van Genuchten model of liquid and gas relative permeability: a) Bentonite (Kunigel OT-9607); b) rock mass.

5.3.2 Results of axisymmetric modelling of the heater test

The calculated results, plotted as time histories of temperature, water content, radial displacements and pore pressure in bentonite and rock, are shown in Figs. 5.5-5.8, respectively, at the corresponding monitoring points.

Figures 5.9 – 5.12 show the comparison between the calculated and measured results of temperature at the first four points. Calculated temperature agrees well with the measured ones. Figure 5.13 – 5.16 give the comparison between the calculated water content and the measured ones in the bentonite. The water content variation in rock is given in Fig. 5.17. The calculated values do not compare well with the measured values. Modelling significantly underestimates the resaturation and desaturation of bentonite in the vicinity of rock mass and heater, respectively. In addition to the fact that the two-phase flow option used in FLAC is unable to take into account the phase changes (condensation/evaporation processes) which can be one of reason of the these discrepancies, the high value of rock mass permeability contribute to un-accelerate the bentonite resaturation.

Furthermore, it seems that, initial values of saturation in the steel (equal 1%) as well as the initial values gas and water pressures in bentonite-steel (initial value of P_{gz} is taken equal to the atmospheric pressure, leading to significant values of initial water pressure in magnitude computed based on initial saturations and eq. 4) have a non-negligible effect on the behaviour of bentonite. Evolution of radial strain at points 2 and 4 is shown in Figure 8 and 9, as well as the measured ones. The calculations indicate the same tendency.

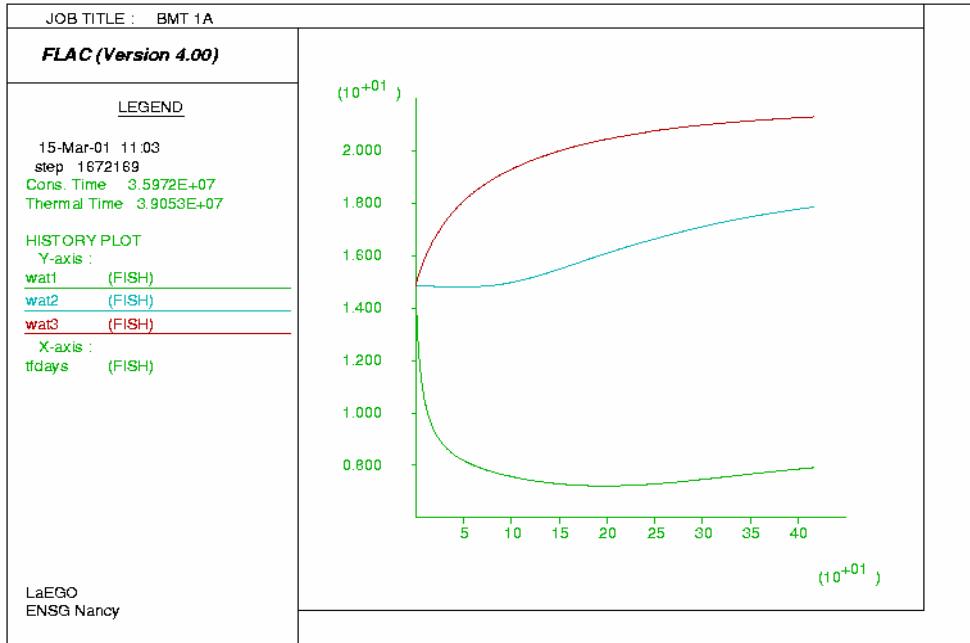


Figure 5.5 Time history of water content (%) at three points in bentonite and rock.

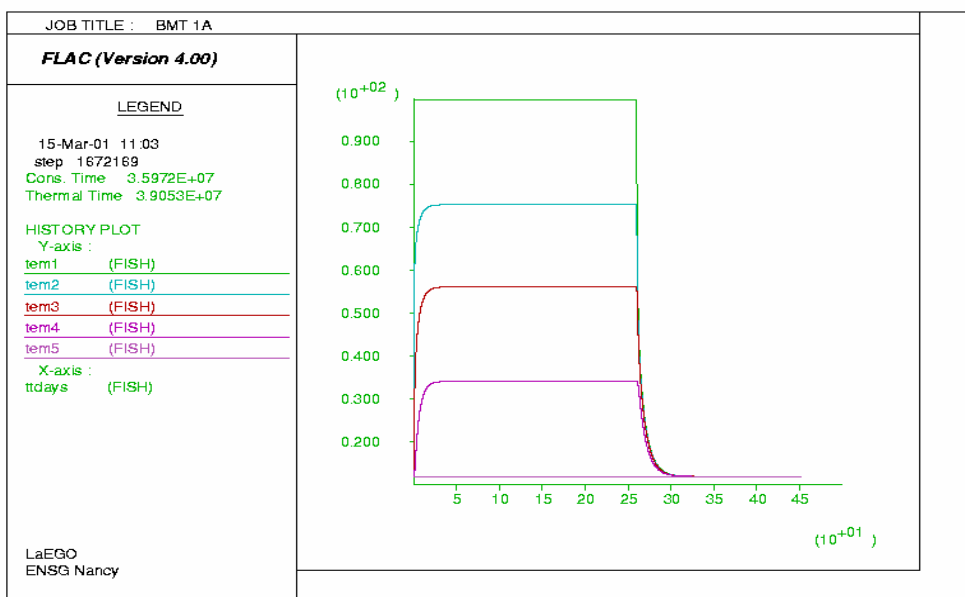


Figure 5.6: Time history of temperature ($^{\circ}\text{C}$) at five points in bentonite.

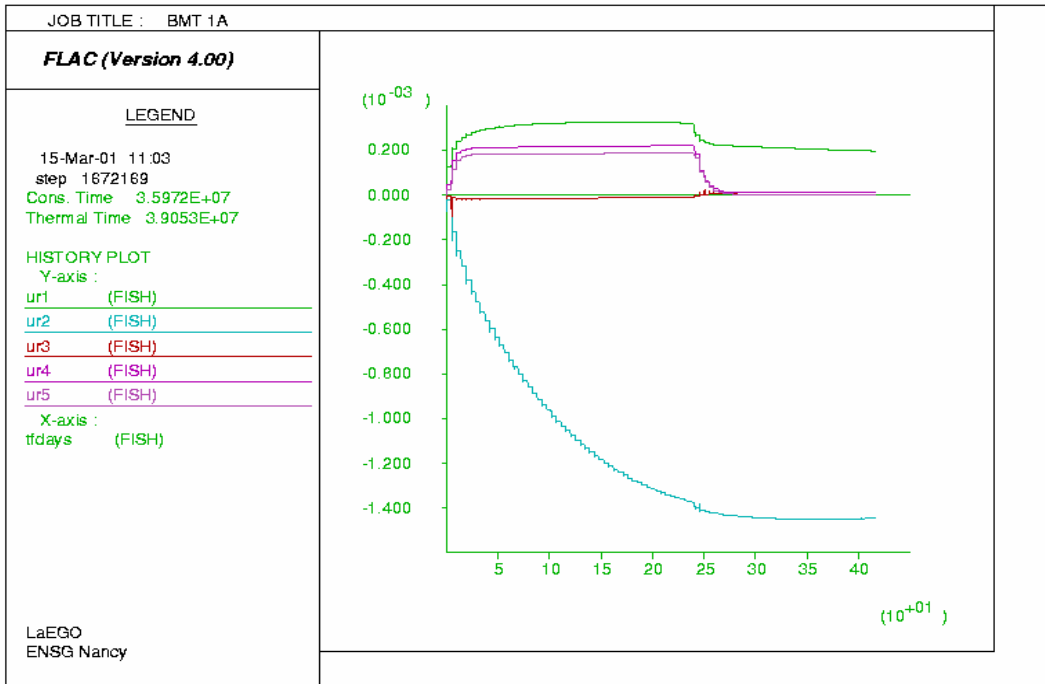


Figure 5.7: Time history of radial displacement at the five points in bentonite and rock.

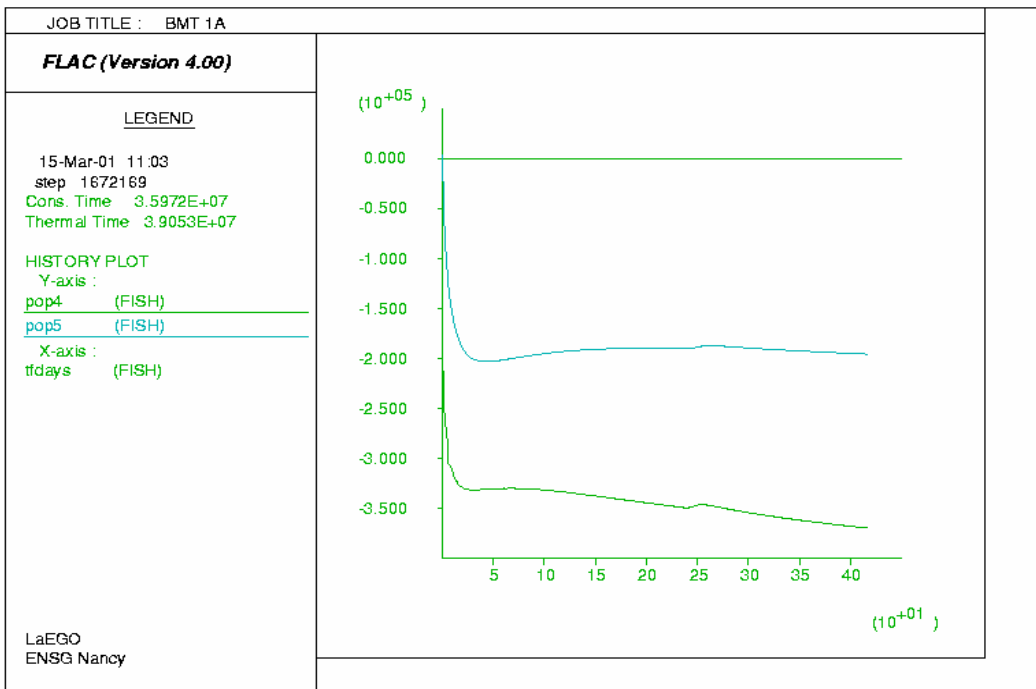


Figure 5.8: Time history of pore pressure at the two points in rock.

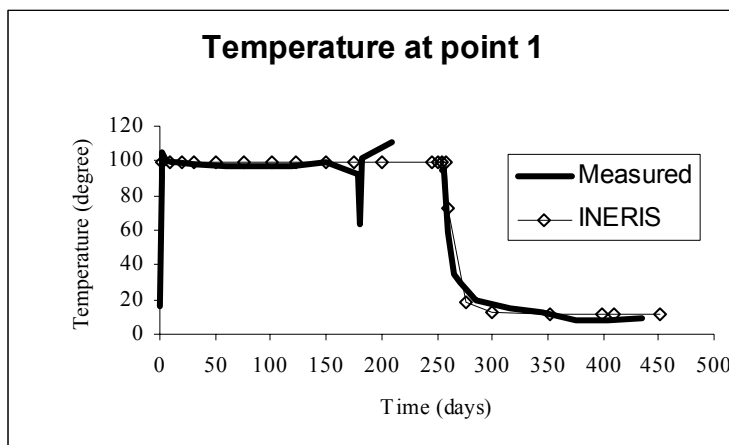


Figure 5.9: Temperature at point 1 in bentonite

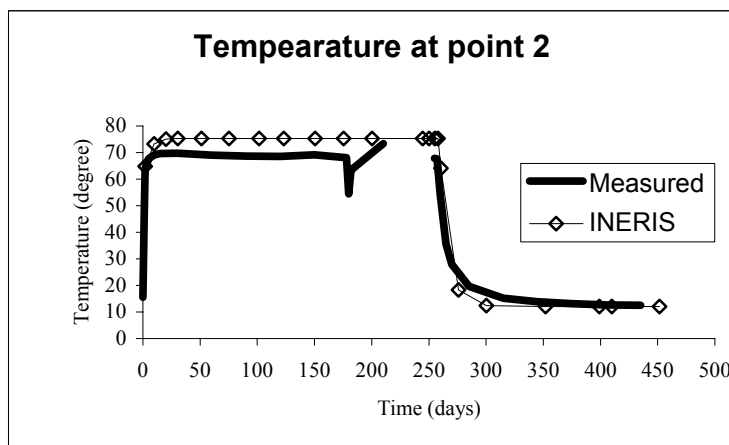


Figure 5.10: Temperature at point 2 in bentonite

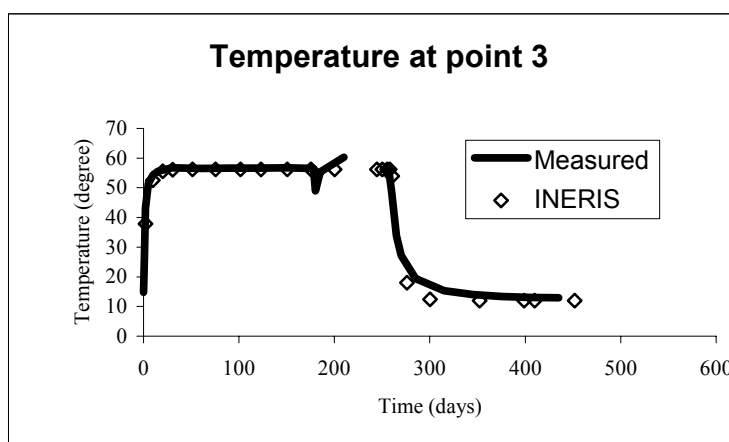


Figure 5.11: Temperature at point 3 in bentonite

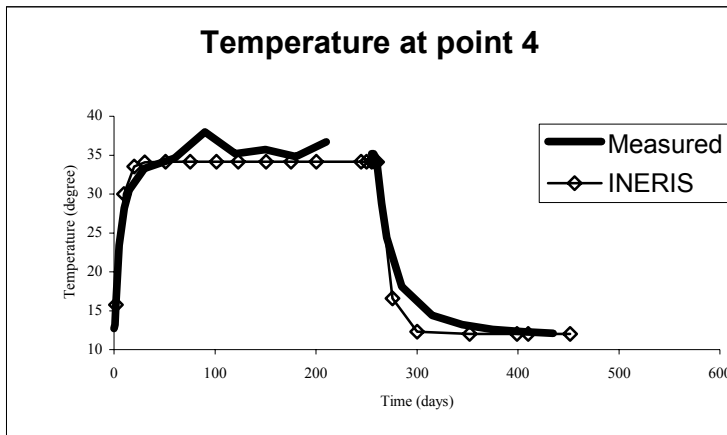


Figure 5.12: Temperature at point 4 in rock mass

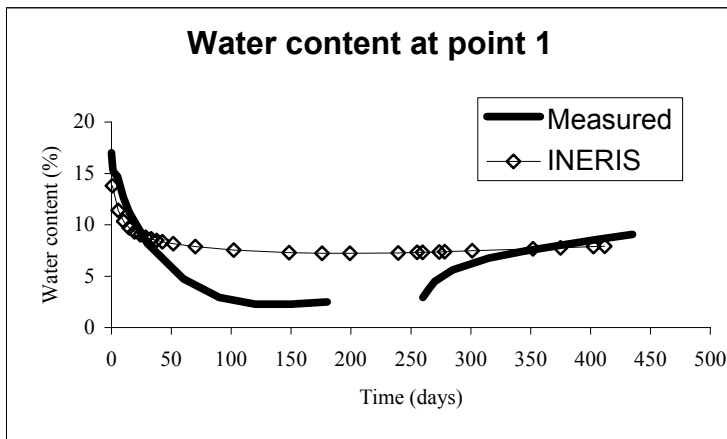


Figure 5.13: Water content at point 1 in bentonite

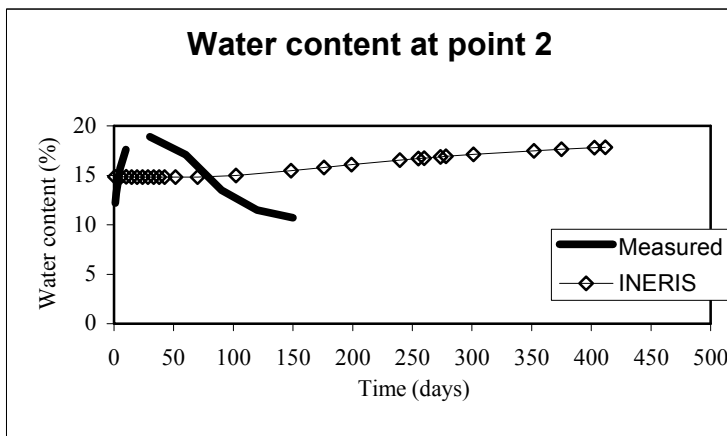


Figure 5.14: Water content at point 2 in bentonite

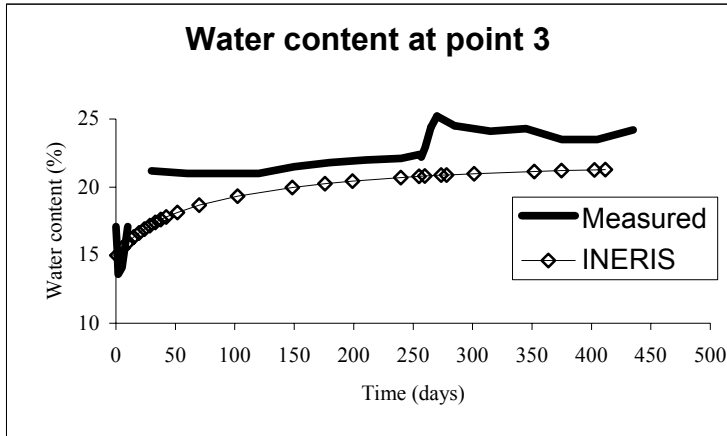


Figure 5.15: Water content at point 3 in bentonite

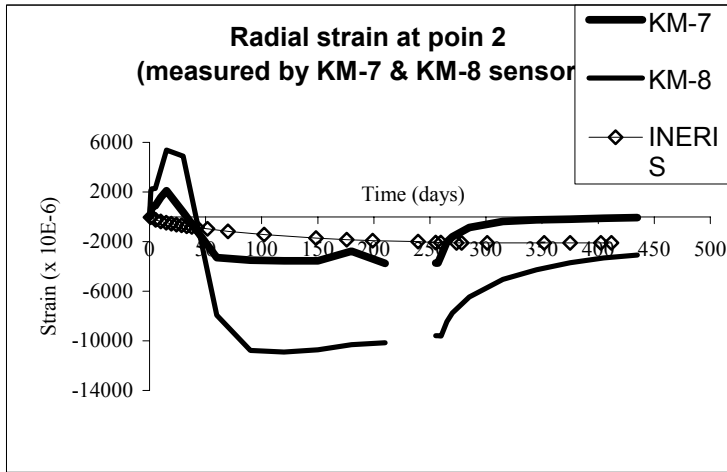


Figure 5.16: Radial strain at point 2 in bentonite

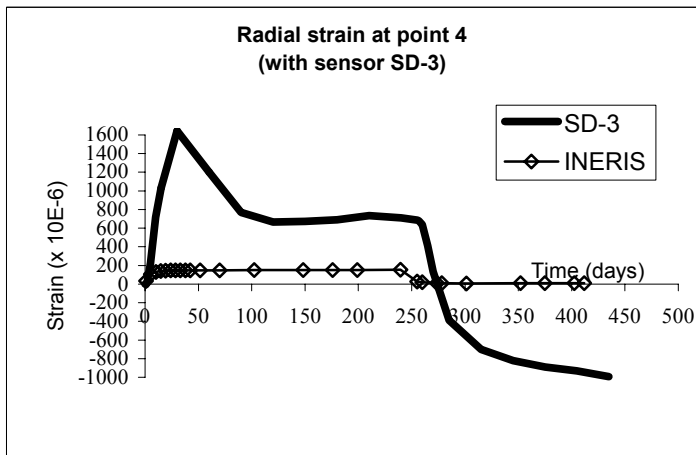


Figure 5.17: Radial strain at point 4 in rock mass

5.4 Conclusion and remarks

Results of this first evaluation of modelling of the Kamaishi mine heater experiment using the two-phase flow option of FLAC (where thermic and hydraulic are uncoupled) show that only the calculated values of temperature agree very well with the experimental values.

Then, due to the significant discrepancies in saturation/desaturation/resaturation of bentonite during the heating and cooling phases between our results and the measured ones (or the results of JNC, LBNL, CNSC teams), these results have to be quickly improved, by regarding the values of permeability in rock/bentonite, initial gas and water pressures in the steel/bentonite, and the re-evaluation of water retention curve of steel assumed here to be identical to the bentonite ones.

6. Re-evaluation of the Kamaishi mine modelling – the IRSN/CEA team studies

6.1 Introduction

This section presents the work performed by the IPSN/CEA team for the first phase of the BMT1 exercise, called BMT1-A. Contrary to some other teams, the IPSN/CEA team did not take part in the first modelling of the Kamaishi Mine, during the Decovalex II project.

Therefore, it has been first necessary to introduce some new developments in the computer Code Castem 2000, in order to be able to treat the BMT1-A problem. Of evidence, the IPSN/CEA had not the time to fully validate these new developments, which have been used first to calculate the BMT1-A case. Some further validation will be necessary in order to gain a full confidence in these new possibilities.

6.2 Governing Equations

The model which has been implemented in the computer code Castem 2000 (Verpeaux et al., 1989) for the treatment of THM responses of unsaturated soils is based on the following assumptions and governing equations.

The solid part medium is a porous medium composed of solid grains, assembled in a skeleton. The grains are assumed to be incompressible, whereas the skeleton may deform. Its displacements are chosen as primary variables.

The pores of the medium are assumed to be filled by a mixture of liquid water and gas. The gas itself is supposed to be an ideal mixture of air and vapour. In the model, the gas pressure, p_g is assumed to stay constant and equal to the atmospheric pressure. The liquid water pressure p_l is therefore used to characterize the evolution of the water in the porous medium.

The equations governing the evolution of the chosen primary variables, which are the displacements $\underline{\xi}$, the liquid water pressure p_l and the temperature T , are classically obtained from conservation equations together with state laws.

In the following equations, φ denotes the porosity, S_l the saturation degree ($S_l \in [0, 1]$) and ρ_l the liquid water density.

The conservation of the total mass of water (liquid and gas) is simplified, based on the following considerations:

- the mass of vapour is negligible compared to the mass of liquid water,
- the flux of liquid water is given by a generalized Darcy's law:

$$q_l = \frac{K k_{rl}}{\eta_l} \rho_l \left(- \underline{\text{grad}} p_l + \rho_l \underline{F} \right) \quad (6.1)$$

where K is the intrinsic permeability, k_{rl} the permeability relative to liquid water and η_l the dynamic viscosity of water. \underline{F} stands for body forces such as gravity.

- The flux of vapour is mainly due to the temperature gradient, such as:

$$\underline{q}_v = - D_{T_v} \underline{\text{grad}} T \quad (6.2)$$

where D_{T_v} is the coefficient of thermal diffusivity of water vapour.

Therefore, the water mass conservation equation can be written:

$$\begin{aligned} \frac{\partial}{\partial t} (\rho_l S_l \varphi) &= - \text{div} \underline{q}_l - \text{div} \underline{q}_v \\ &= + \text{div} \left[\frac{K k_{rl} \rho_l}{\eta_l} (\underline{\text{grad}} p_l - \rho_l \underline{F}) \right] \\ &\quad + \text{div} (D_{T_v} \underline{\text{grad}} T) \end{aligned} \quad (6.3)$$

The conservation of momentum is written classically as:

$$\text{div} \underline{\underline{\sigma}} + \rho \underline{F} = 0 \quad (6.4)$$

where $\underline{\underline{\sigma}}$ stands for the total stress in the porous medium, and ρ its equivalent density, given by:

$$\rho = (1 - \varphi) \rho_s + \varphi S_l \rho_l \quad (6.5)$$

In equation (6.5), ρ_s denotes the density of the skeleton. The material behaviour law is of Biot's poroelastic type, such as:

$$d\underline{\underline{\sigma}} = \underline{\underline{C}} (d \underline{\underline{\varepsilon}} - \alpha_s dT \underline{\underline{\delta}}) - b dp_l \quad (6.6)$$

In the above equations, $\underline{\underline{C}}$ is the drained elastic property tensor, α_s the skeleton thermal expansion coefficient, $\underline{\underline{\delta}}$ the Kronecker symbol, and b the Biot's coefficient, which, in the unsaturated case, is assumed to depend on the capillary pressure p_c ($p_c = p_g - p_l$).

The degree of saturation is related to the capillary pressure p_c through the function:

$$S_l = S_l(p_c) \quad (6.7)$$

which is assumed to be independent of the temperature, in view of the considered bentonite experimental results. Finally, the conservation of energy is simply taken in the simplified following form:

$$\rho C \frac{\partial T}{\partial t} - \text{div} (\underline{K}_T \cdot \underline{\text{grad}} T) = q \quad (6.8)$$

where ρC stands for the equivalent porous medium heat capacity, \underline{K}_T is the heat conductivity and q represents a heat source.

In the model, we have assumed the following dependencies:

$$\rho C = (1 - \varphi) \rho_s C_s + \varphi S_l \rho_l C_l \quad (6.9)$$

and

$$K_T = K_T(S_l) \quad (6.10)$$

In equation (6.9), C_s and C_l denote respectively the specific heat of the skeleton and of the liquid water.

In the code Castem 2000, the above equations are solved using a classical finite element method. The temperature equation is solved separately, whereas the water mass conservation and momentum conservation equations are solved together. Because of the strong non-linearity that are present in these equations, a fully implicit time integration scheme is used.

6.3 Modelling Data For The Bmt1-A Exercise

In this paragraph, we give in detail all the data that have been used for the calculation of the BMT1-A exercise.

6.3.1 Geometrical data

The domain considered for the BMT1-A being a radial line from the centre of the heater, an axisymmetric model has been chosen for the calculation. The model is made of an assembly of three different zones, comprising first the heater, from $r = 0.47$ m to $r = 0.52$ m, then the bentonite from $r = 0.52$ m to $r = 0.85$ m and finally the rock mass, from $r = 0.85$ m to $r = 10$ m. The connections between these zones are assumed to be perfect, which means that no special interface element has been used.

The axisymmetric mesh adopted is shown on Fig. 6.1, together with a zoom of the interface zone between the bentonite and the rock-mass. It comprises 63 quadratic elements with eight nodes each.



a) Mesh used for the calculation



b) Zoom on the interface between bentonite and rock mass

Figure 6.1: Mesh used for the calculation

6.3.2 Material properties

In the calculation, only the bentonite has been modelled as a partially saturated medium. The rock mass has been treated as a saturated poroelastic material, according to Biot's approach, while the heater has been considered as a classical linearly elastic continuum.

The material properties have been derived either from the available data or from calibration tests such as those used in the previous Kamaishi Mine modelling exercise, during the Decovalex II project, as summarized in Table 6.1.

Table 6.1: Material properties used for the different zones

Material	Property	Value
Bentonite	Dry density (kg/m ³)	1650
	Porosity	0.389
	Young's modulus (Pa)	1.5 10 ⁸
	Poisson's ratio	0.3
	Thermal expansion (1/°C)	1.10 ⁻⁵
	Thermal diffusivity of water vapour (m ² /s)	1.10 ⁻¹¹
	Intrinsic permeability (m ²)	1.6 10 ⁻²⁰
	Skeleton density (kg/m ³)	1600
	Skeleton specific heat (J/kg/°C)	426
	Water density (kg/m ³)	1000
	Water specific heat (J/kg/°C)	4180
Water bulk modulus (Pa)	2.27 10 ⁹	
Rock Mass	Density (kg/m ³)	2300
	Porosity	0.03
	Young's modulus (Pa)	3.10 ¹⁰
	Poisson's ratio	0.3
	Thermal expansion (1/°C)	8.21 10 ⁻⁶
	Intrinsic permeability (m ²)	1.10 ⁻¹⁸
	Biot's coefficient (-)	1
	Thermal conductivity (W/m/°C)	2.7
	Specific heat (J/kg/°C) ^(*)	833
Heater	Density (kg/m ³)	7800
	Young's modulus (Pa)	2.10 ¹¹
	Poisson's ratio	0.3
	Thermal expansion (1/°C)	1.64 10 ⁻⁶
	Thermal conductivity (W/m/°C)	53
	Specific heat (J/kg/°C)	460

In particular, the capillary pressure curve has been taken from the laboratory tests (Jing et al., 1999) as shown on Fig. 6.2. The relative permeability has been obtained from the water diffusivity measurements. Here, since we have neglected the vapour flux due to the pressure gradient, we have identified a relative permeability on the whole range of saturation, which includes the vapour flux at low degree of saturation. Its variation is plotted on Fig. 6.3. The curves $S_l(p_c)$ as well as $k_{rl}(S_l)$ have been introduced

^(*) Remark: Since the rock mass has been considered as saturated, the specific heat corresponds to the equivalent porous medium.

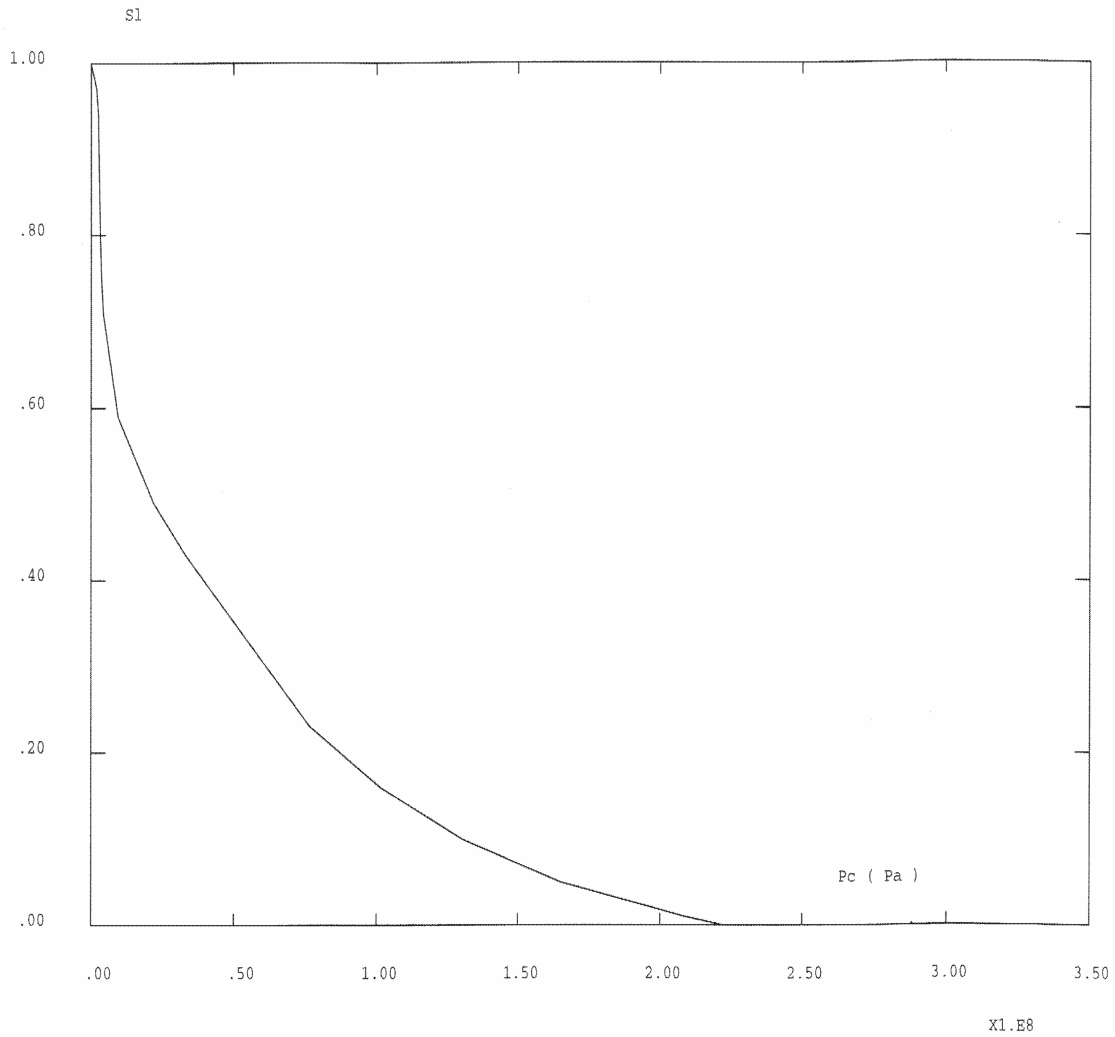


Figure 6.2: The capillary pressure curve.

directly in the computer code Castem 2000. The dynamic viscosity variation with temperature has been taken as:

$$\eta_l(T) = 661.2 \cdot 10^{-3} + (T + 44.15)^{-1.562} \quad (6.11)$$

where T is in °C and $\eta_l(T)$ is in Pa x s.

The Biot's coefficient b varies with the capillary pressure according to (Lassabatère et al., 1998):

$$b(p_c) = \frac{p_r}{p_r + p_c} \quad (6.12)$$

where p_r has been identified from the results of the swelling test as:

$$p_r = 0.25 \text{ MPa} \quad (6.13)$$

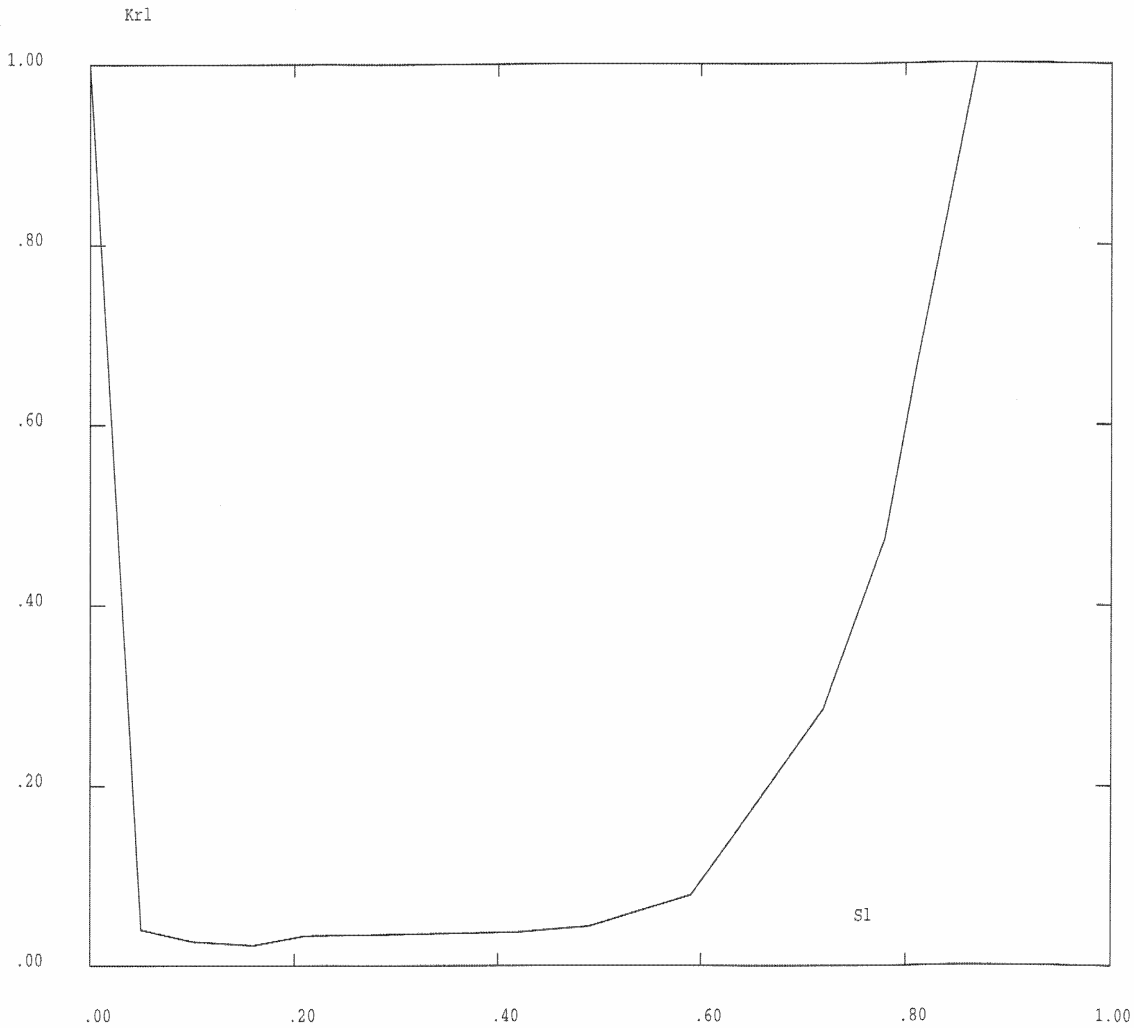


Figure 6.3: Relative permeability versus degree of saturation.

The variation of the thermal conductivity with the degree of saturation has been taken as:

$$K_T(S_1) = 0.5 + 1.5 \times S_1 \quad (6.14)$$

where K_T is in $W/m/^\circ C$.

6.3.3 Initial and boundary conditions

Initially, the heater, the bentonite and the rock mass are supposed to be at a uniform temperature of $12^\circ C$. In this state, displacements and stresses are taken as zero everywhere. In the bentonite, the gravimetric water content is equal to 15%, which according to the value of the porosity, corresponds to an initial degree of saturation of 65.6% and a capillary pressure of 6.6 MPa. In the rock mass, the initial liquid pressure is set equal to 3.9 KPa.

The heating is simulated by prescribing a 100°C temperature at the inner radius ($r = 0.47$ m) of the heater during the 258 days heating period. Then, this boundary condition is replaced by a zero heat flux during the 180 days cooling period. On the same boundary, the radial displacements are free. The vertical displacements are prescribed to zero on the two horizontal surfaces of the model. A radial displacement is prescribed to zero at the limit of the domain ($r = 10$ m) in order to account for the extension of the rock mass. There, the liquid pressure is supposed to remain constant, and equal to 3.9 KPa. The interface between the heater and the bentonite ($r = 0.52$ m) is supposed to be impervious.

It must be noticed that in the original problem definition, the impervious condition was set at the inner radius of the heater. However, since we considered a purely mechanical heater, this condition was translated to the inner radius of the bentonite. In order to obtain, with this axisymmetric model, temperatures close to the ones measured in the real experiment, it was agreed to prescribe a constant 12°C temperature at a radius closer to the bentonite, than the initially foreseen radius $r = 10$ m. We have obtained satisfactory temperature by prescribing this condition at a radius $r = 2.3$ m.

6.4 Results of the Axisymmetric modelling of the heater Test

In this paragraph, we present some of the results obtained, at the specified locations.

First, the temperature histories at the first four points, are presented on Fig. 6.4. The results obtained are fairly close to those obtained either experimentally or by the other teams.

Figure 6.5 shows the histories of the water content at points 1 to 3. Comparison with experimental results indicate that the shape and intensity calculated at point 1, where the bentonite first dries out and then wets again after the heating is turned off, is fairly well reproduced. This is mostly linked to the value of the thermal diffusivity of water vapour, which controls the drying process of the bentonite under the thermal gradient.

The discrepancy between experimental and calculated values is more important on points 2 and 3. In particular, although a low intrinsic permeability has been assumed for the rock mass (10^{-18} m²), assuming that cracks present in the rock had been sealed by the bentonite during its compaction, the hypothesis of a constantly saturated rock mass may contribute to the fact that the buffer is rewetting too quickly at the interface with the rock mass (point 3).

On the Fig. 6.6 are presented the radial stresses at points 1 to 3. Here, negative stresses correspond to compression. As can be intuitively expected, the compression develops in all the buffer during the heating and decreases when the heating is turned off. The level of the radial stresses reached in the bentonite is similar to the one measured in the experiment at point BBC. This may partly be attributed to the value of the thermal expansion coefficient (10^{-5}) which has been used in this analysis.

Finally, Figs. 6.7 and 6.8 show respectively the radial strains at points 2 and 4. On these figures, a positive value corresponds to an extension. Here, the level of the strains reached is much lower than the one obtained in the experiments.

The tendency of the stresses and strains in the buffer is also different, during the cooling phase, since the calculation predicts a non monotonous behaviour, whilst the experimental curves show a monotonous one. This might be an effect of the discrepancy of the rewetting of the buffer which is too quick at points 2 and 3.

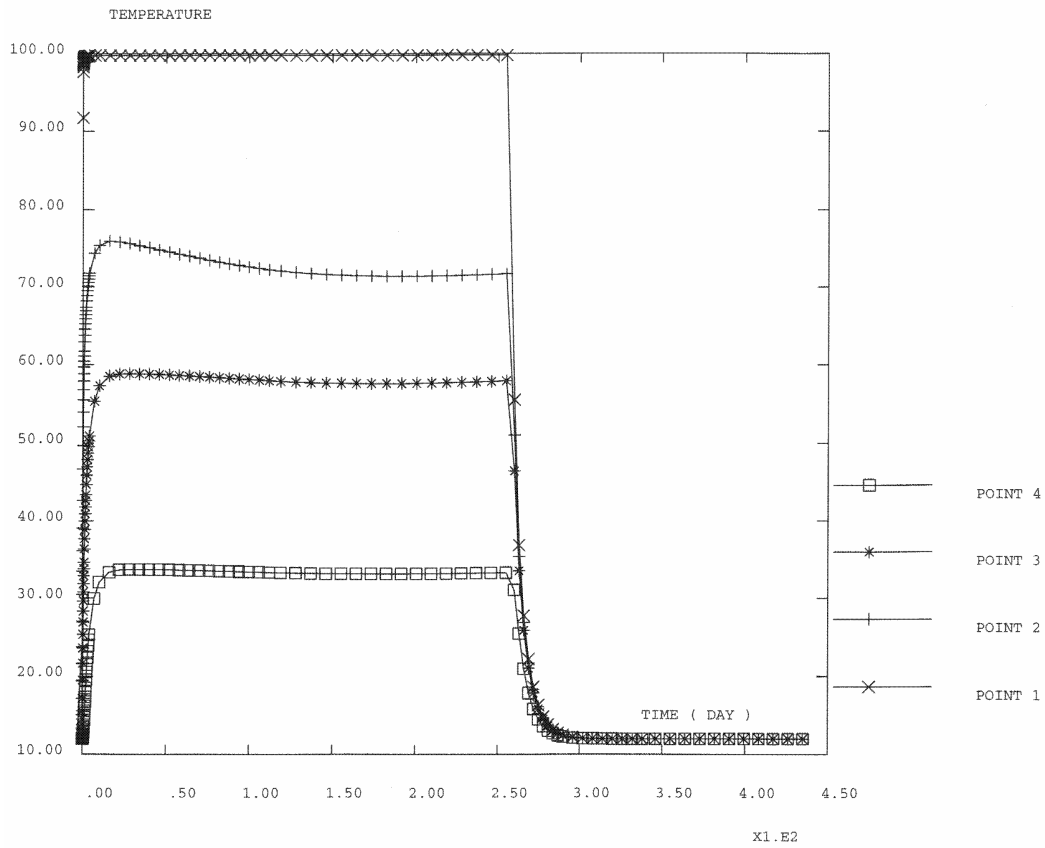


Figure 6.4: Temperature at points 1 to 4.

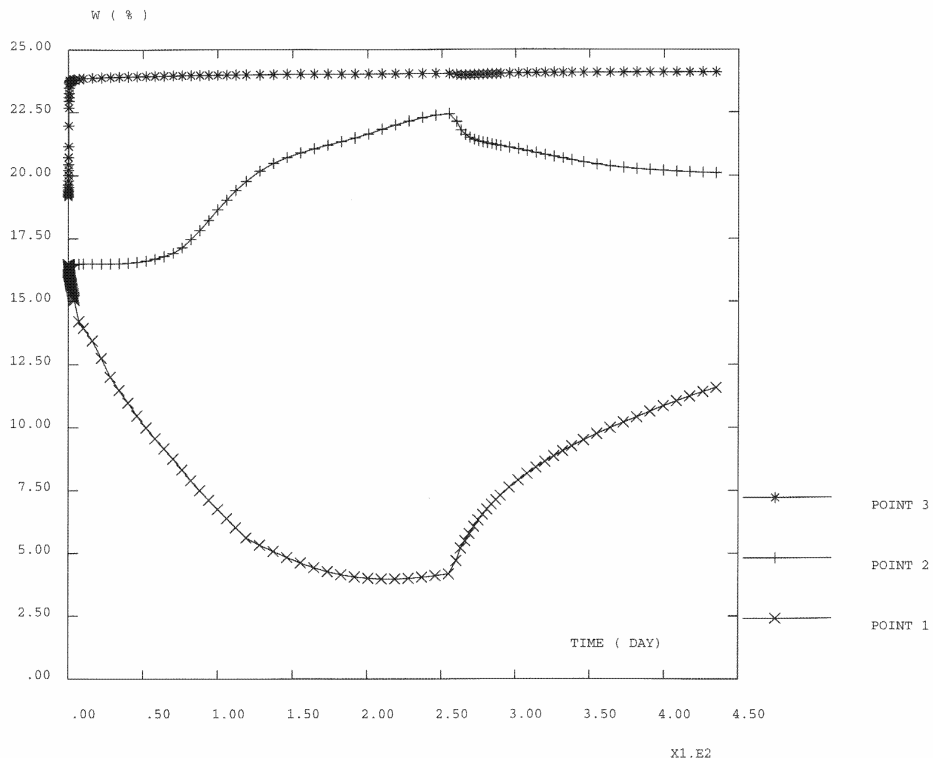


Figure 6.5: Water content at points 1 to 3.

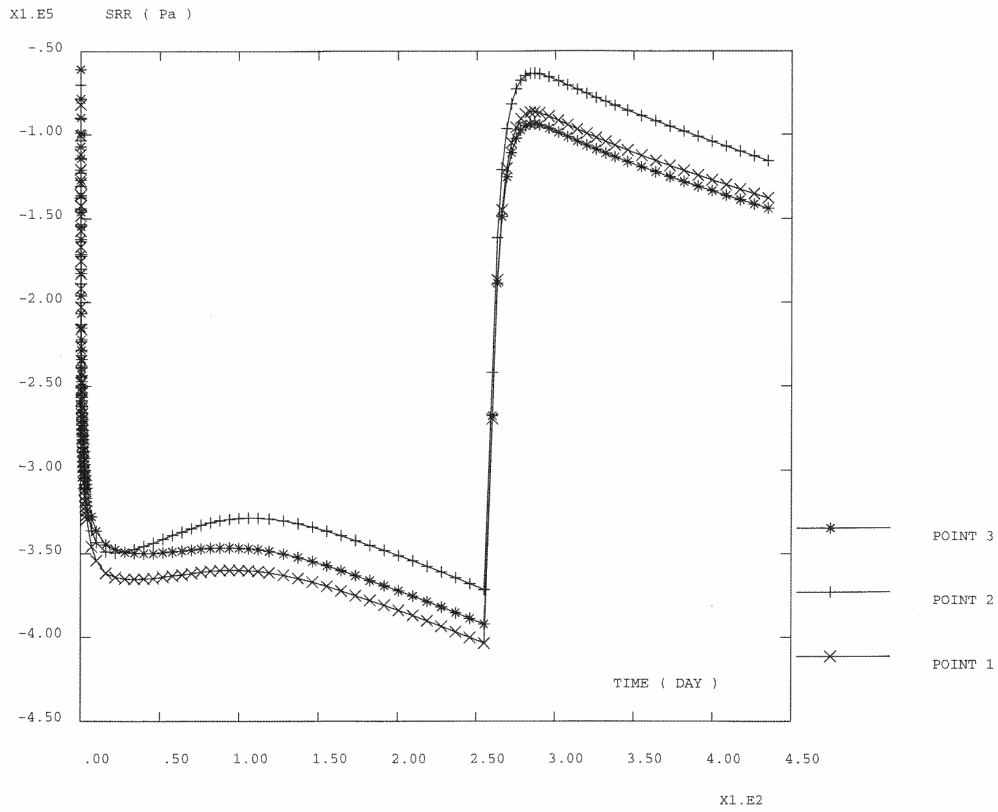


Figure 6.6: Radial stress at points 1 to 3.

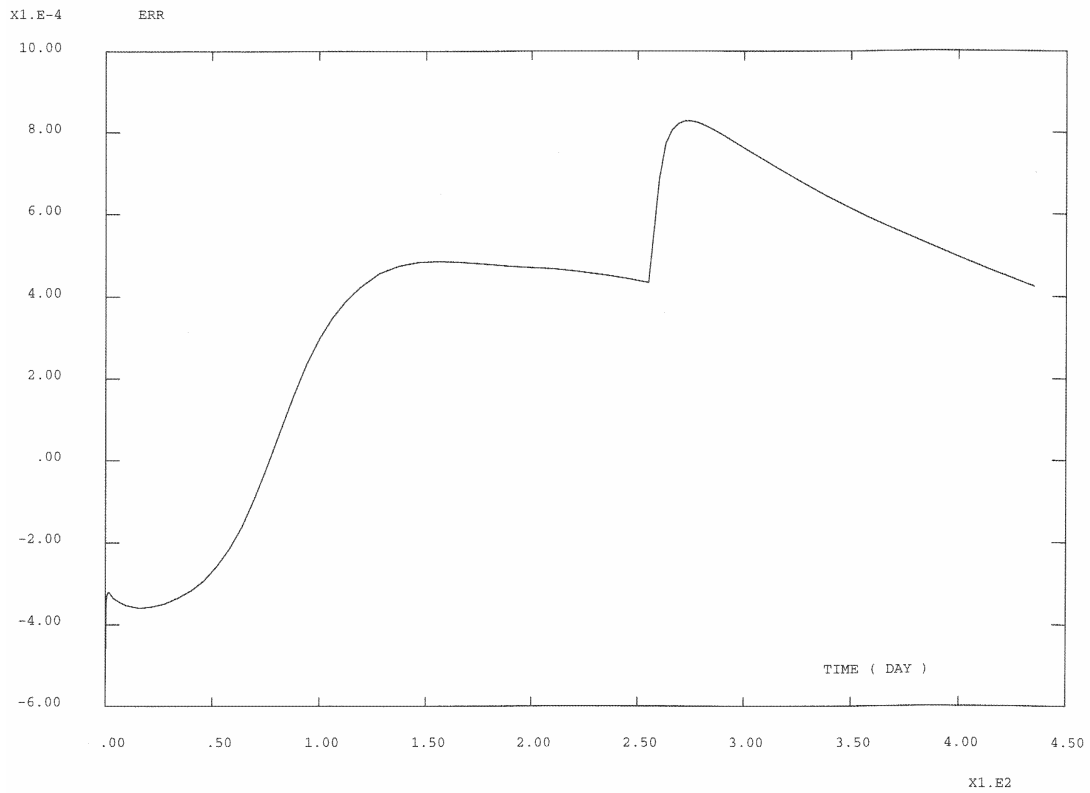


Figure 6.7: Radial strain at point 2.

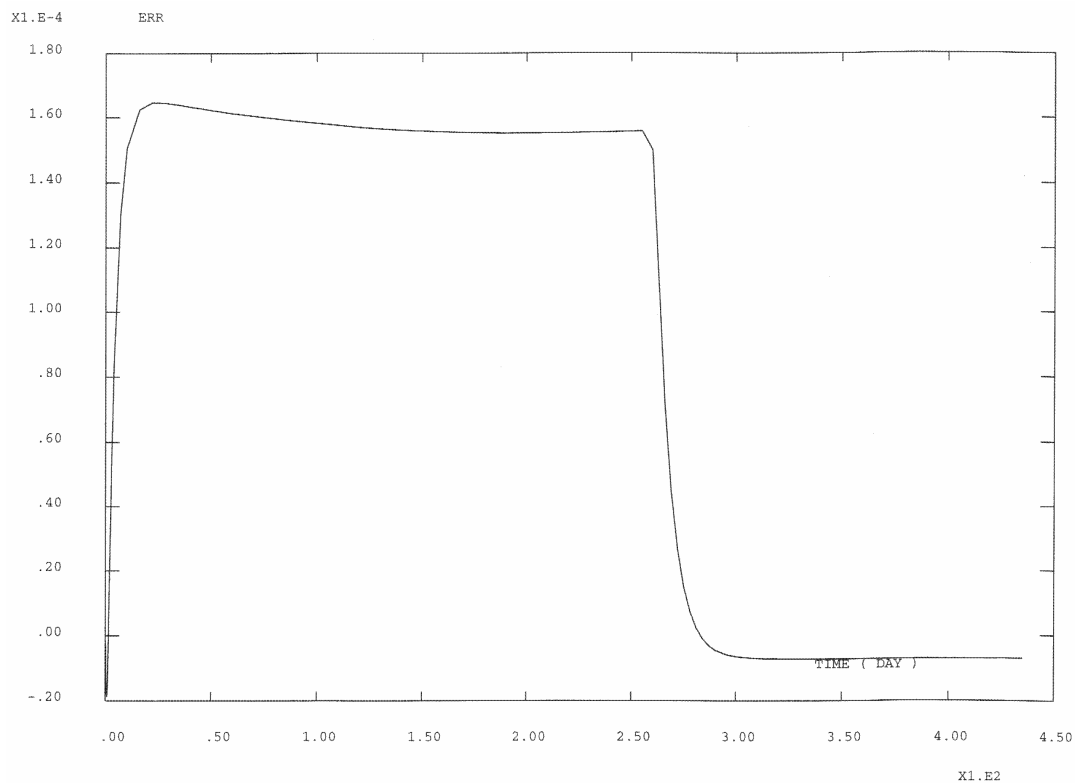


Figure 6.8: Radial strain at point 4.

6.5 Conclusion

This modelling of the simplified case of the Kamaishi Mine heater test is the first application of the new developments introduced in the computer code Castem 2000, in order to be able to treat the THM response of unsaturated rock-masses. The first results obtained are encouraging. The temperatures are well reproduced, and the water contents in the buffer are satisfactory except at point 2. However, it must be noted that most of the teams participating in the BMT1-A exercise have difficulties to predict this curve.

Concerning the mechanical results, even if some tendencies could be reproduced, there are some large discrepancies either on the stress and strain levels predicted, or even on the shapes of the curves, in particular in the cooling period.

One of the key factors in these results is the function $b(p_c)$, in our model, which involves some reference pressure, as parameter, which has been simply adjusted from the swelling test result. This modelling should be further investigated.

7. Comparison and concluding remarks

This chapter summarizes and compares the results. The further calibration of individual models against the Kamaishi in-situ THM test was based on the work performed during DECOVALEX II for Task 2C (Jing et al., 1999), can be found in chapters 2, 3 and 4, and will not be repeated here. In this chapter, the focus is placed on the summary and comparison of the results of the simplified axisymmetric models.

7.1 Comparison of results

Figures 7.1 and 7.2 compares the temperature results by JNC, CSNC, KTH/SKI and INERIS/ANDRA models, at point 1, 2, 3 and 4, respectively. The calculated and measured values agree well and demonstrate that conductive heat transfer is the main heat transport mechanism. All models reproduced correctly the temperature behaviour during the complete heating-cooling phases, and the reasons for the discrepancies are perhaps the model geometry, mesh size, moisture-heat interaction models with different thermal diffusion laws and values of thermal diffusivities.

Figure 7.3 compares the radial stress at point 1 as a function of time, where experimental data are available. For the CEA/IPSN, CSNC, KTH/SKI and JNC models, although large discrepancies still exist, especially among calculated results, but the general trend among the models agrees fairly well with the measured data at this point. This indicates that the thermal expansion phenomenon is modelled fairly well by these teams, but not the swelling process, which may be the reason for the discrepancies.

Figure 7.4 compares the water contents at points 1, 2 and 3, respectively, as functions of time. The calculated results agree well with the measured ones at points 1 and 3, both qualitatively and quantitatively, for all teams except the INERIS/ANDRA model during both heating and cooling periods, which may be caused mainly by the treatment of steel as porous medium and the fact that the thermally driven water transport was ignored in the INERIS/ANDRA model. The major discrepancies exist at point 2 in all models except for the KTH/SKI model. The possible causes for such major discrepancies at point 2 could be many, especially coupled porosity-permeability, which was ignored in all models, and condensation-evaporation, which was ignored in CEA/IPSN, CNSC, JNC and INERIS/ANDRA models. At point 3, the CNSC and KTH/SKI models indicate faster re-saturation. It is possible that the rock around bentonite was initially unsaturated, leading to the observed delay in the advances of the saturation front.

Figures 7.5 compares radial strains at points 2 and 4, respectively. Like stresses, large discrepancies still exists among the models, but compared with measured data, a consistent trend in the strain data can still be detected between the measured and calculated results at points 2. For point 4 in the rock, the JNC model results of the strain is consistent with the experimental data in trend, and CNSC model results were under-predicted, due to the fixed outside boundary that is too close to the center (radial distance of 3 m).

One of the reasons for the discrepancies may be the lack of more realistic constitutive models for the unsaturated expansive bentonite in the computer codes applied for this study, which are important for more realistic simulation of the mechanical effects.

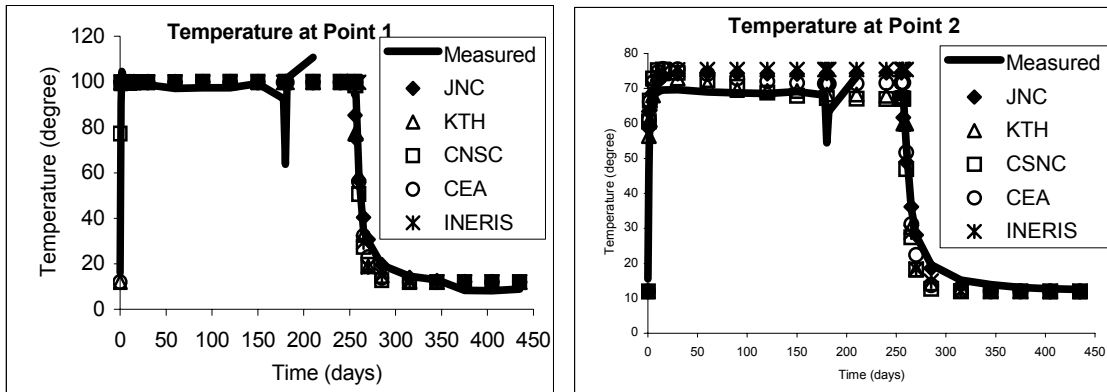


Figure 7.1: Time histories of temperature at Points 1 and 2.

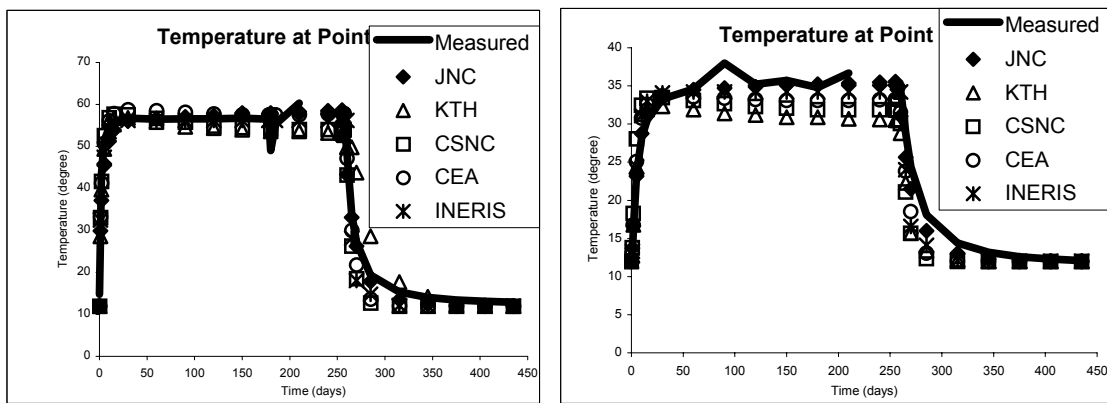


Figure 7.2: Time histories of temperature at points 3 and 4.

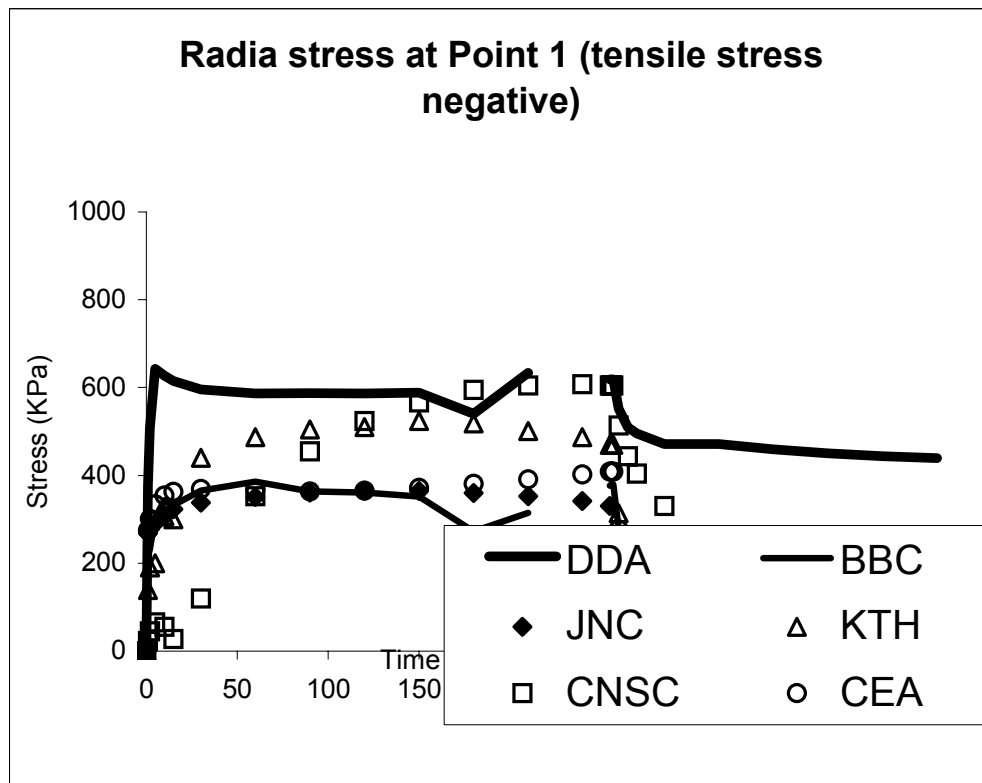


Figure 7.3: Radial stress at points 1.

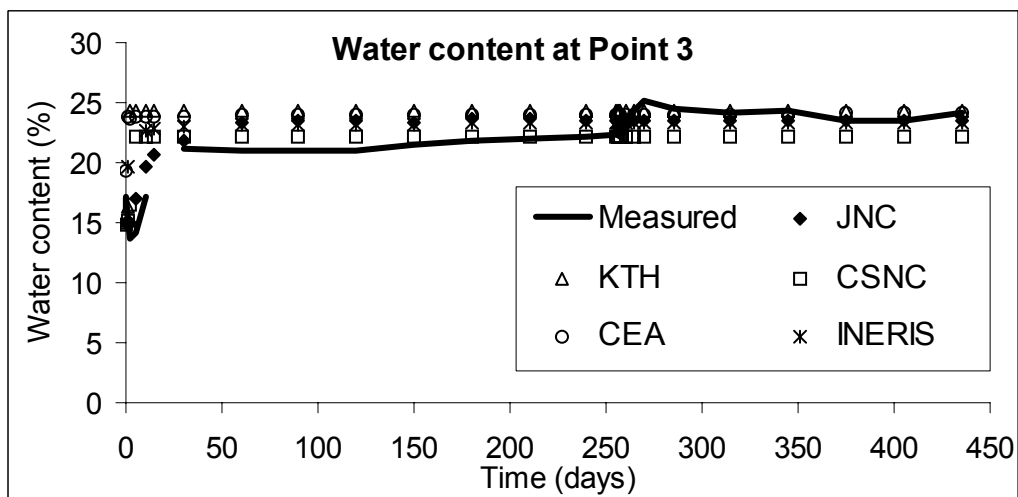
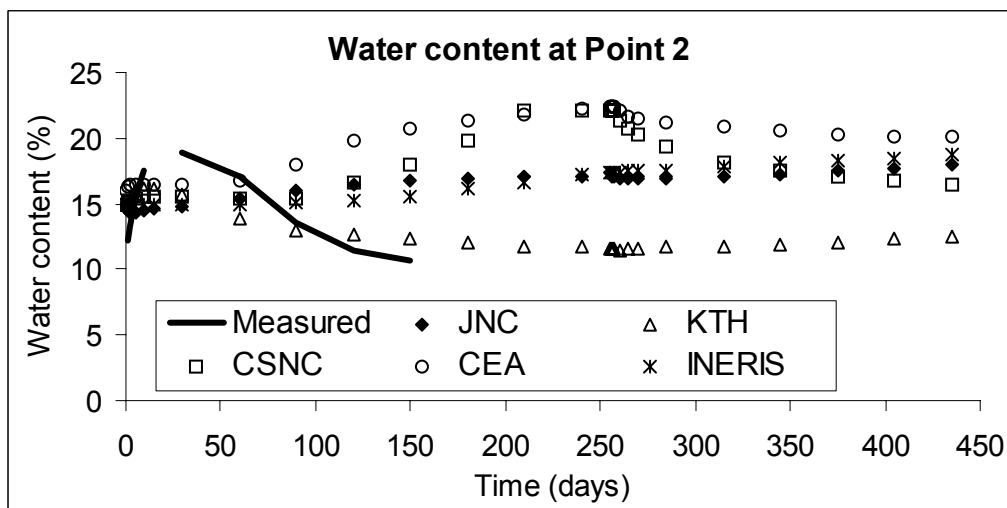
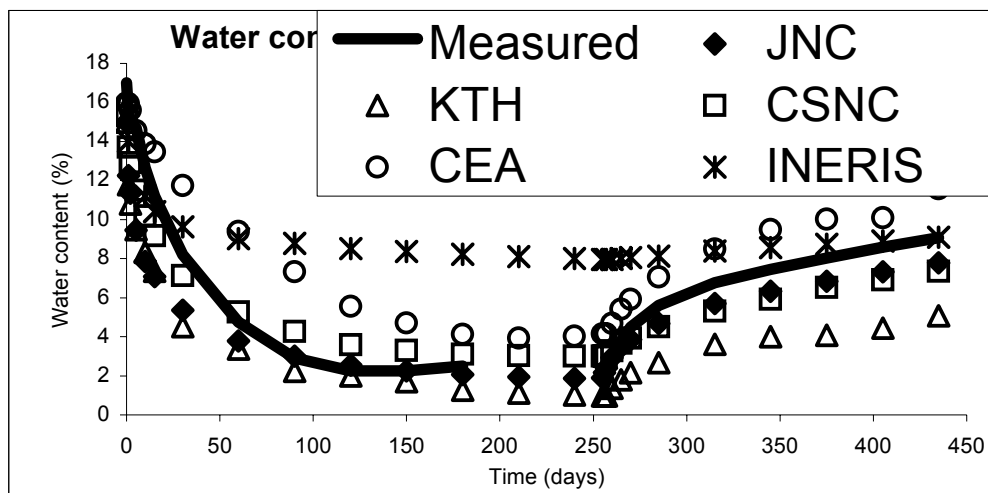


Figure 7.4: Water contents at points 1, 2 and 3, during heating and cooling periods.

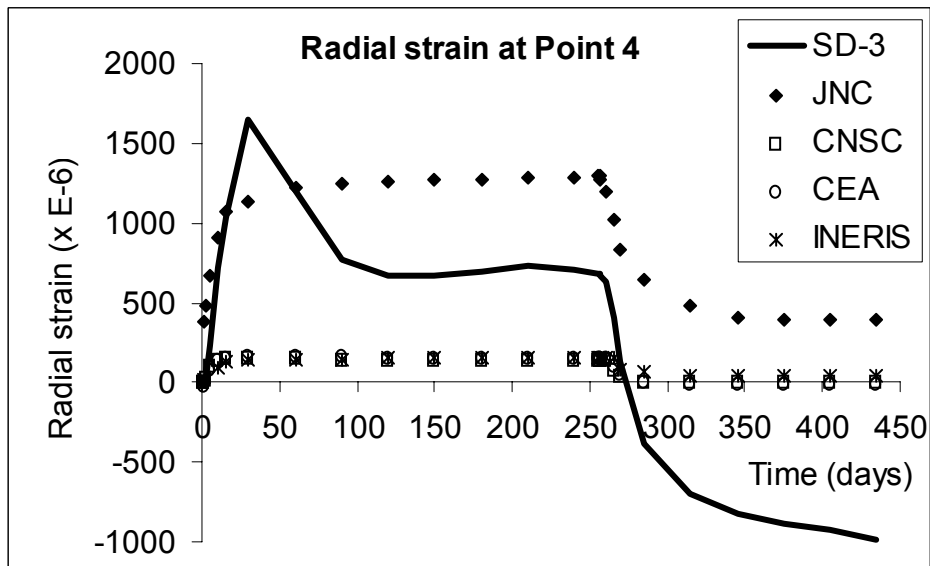
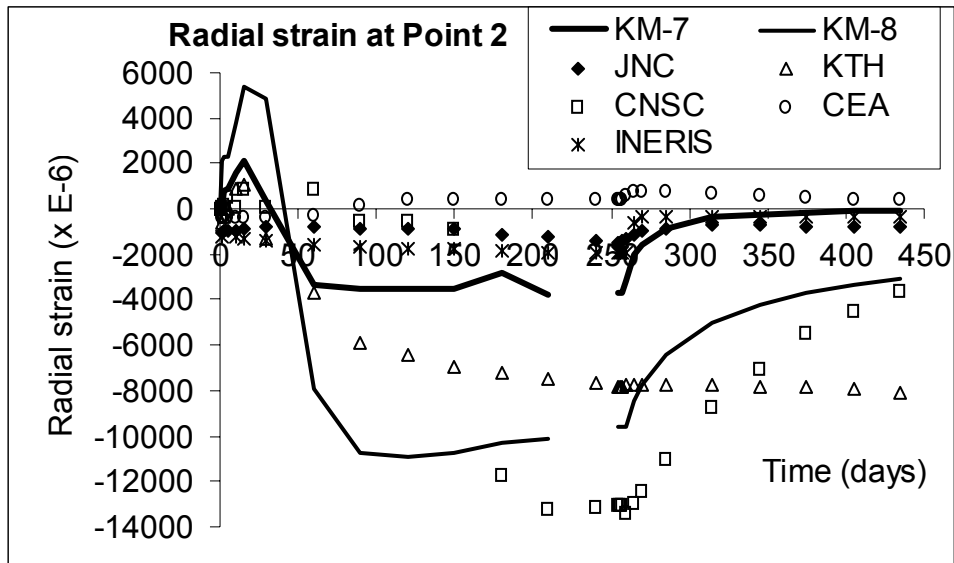


Figure 7.5: Radial strains at points 2 and 4.

7.2 Summary and conclusion

A number of improvements to the modelling of the Kamaishi Mine heater test were suggested and tested in this study. The suggested improvements were tested using a simplified axisymmetric model of the heater test. Although the model geometry is much simplified compared to the field test conditions, improved simulation of the general THM responses were obtained, as compared with the Task 2C results of DECOVAEX II. The measures taken for improvement were:

- Parameter changes (reduced rock mass permeability and rock mass thermal expansion by the KTH/SKI team, and increased thermal expansion coefficient and reduced swelling pressure constant of the buffer by JNC team)

- Inclusion of the sealing of rock fractures by penetrating bentonite by the KTH/SKI team, which can explain the uniform (axisymmetric) wetting of the bentonite.
- An improved swelling/shrinking strain function combined with an increased thermal expansion of the bentonite giving a good match of the mechanical (stress, strain) behavior of the buffer by the KTH/SKI team.
- Use of higher E (Young's modulus) and ν (Poisson's ratio) of the bentonite near the heater, and use of a "sealed" layer of rock around the bentonite by the CNSC team.

As a results of the above measures, the results from the simplified axisymmetric model used in the re-evaluation of the Kamaishi mine experiment showed general improvement over the original models used in the prediction phase during the DECOVALEX II project, especially in the following aspects:

- Calculated values of temperature agree very well with the experimental values, for all teams.
- Generally improved stress and strain behaviour in the bentonite, at least qualitatively though, with the measured results.
- The water content near the heater (at point 1) is relatively well predicted by all teams, although the saturation front at the bentonite/rock interface are still predicted to advance much faster than in reality.

In general, the mechanical behaviour of the buffer is complex with forces contributing from shrinking/swelling in all part of the bentonite, external stress from the thermal expansion of the heater and rock, and internal thermal expansion of the bentonite itself. However, a reasonable prediction of the mechanical behaviour can be done if all relevant bentonite properties are known from laboratory tests.

References

- Berchenko I., C. Detournay and E. Detournay. *Solution of thermoporoelastic problems using FLAC*. In: *FLAC and Numerical Modeling in Geomechanics*, eds Detournay C. and Hart R., Balkema Rotterdam, ISBN 90 5809 074 4, pp. 133-140, 1999.
- Chijimatsu M., Sugita Y., Fujita T. and Amemiya K., *Coupled thermo-hydro-mechanical experiment at Kamaishi mine, Technical note 15-99-02, Experimental result.*, Japan Nuclear Cycle Development Institute, JNC TN8400 99-034. 1999.
- Chijimatsu M., Fujita T., Sugita Y. and Ishikawa H. *Coupled thermo-hydro-mechanical experiment at Kamaishi mine. Laboratory rock property tests*. Power reactor and nuclear fuel development corporation (PNC). TN8410 96-060. 1996.
- Dangla, P. *Approches Energetique et Numerique des Milieux Poreux Non Satures*“. *Mémoire d’habilitation à diriger des recherches*. Ecole Nationale des Ponts et Chaussées. Ecole Normale Supérieure de Cachan. Université de Marne-la-Valée, 1999.
- Fujita T., Sugita Y., Chijimatsu M. and Ishikawa H. *Coupled thermo-hydro-mechanical experiment at Kamaishi mine. Fracture characteristics*. Power reactor and nuclear fuel development corporation (PNC). TN8410 96-061. 1996.
- Fujita T., Chijimatsu M., Ishikawa H., Suzuki H. and Matsumoto K. *Coupled thermo-hydro-mechanical experiment at Kamaishi mine. Fundamental properties of bentonite OT-9607*. Power reactor and nuclear fuel development corporation (PNC). TN8410 97-071. 1997.
- Fujita, T., M. Chijimatsu, H. Ishikawa, H. Suzuki and K. Matsumoto. *Fundamental Properties of Bentonite OT-9607*. PNC TN8410 97-0701. 1997.
- van Genuchten, M. Th., *A Closed Form Equation for Predicting the hydraulic conductivity of unsaturated soils*. In: *Soil Sc. Soc. Am. J.*, Vol. 44, pp. 892-898. 1980.
- Hutter, K., L. Laloui, and L. Vulliet, *Thermodynamically based mixture models of saturated and unsaturated soils*. in *Mechanics of Cohesive-Frictional Materials*, Vol. 4, Issue no 4, pp. 295-338. F. Darve and R. de Borst, Eds. Wiley. 1999.
- Israelsson, J.I., *Short description of FLAC Version 3.2*. In: *Coupled Thermo-Hydro-Mechanical Processes of Fractured Media*, eds Stephansson O., Jing L. and C.F. Tsang. 1996.
- ITASCA Consulting Group Ltd., *FLAC Version 4.0.260 : User’s guide*. 2001.
- Japan Nuclear Cycle development Institute. *Evaluation of coupled thermo-hydro-mechanical phenomena in the near field for geological disposal of high-level radioactive wastes*. 2000.
- Japan Nuclear Cycle Development Institute. *Second progress report on research and development for the geological disposal of HLW in Japan, H12: project to establish the scientific and technical basis for HLW disposal in Japan*. JNC TN1410, 2000-001. 2001.
- Jing, L., O. Stephansson, L. Borgesson, M. Chijimatsu, F. Kautsky, and C-F. Tsang. *DECOVALEX II Project - Technical Report - Task 2C*. SKI 99:23. 1999.
- Lassabatère, T., C. Imbert, M. A. Etilé. *Biot modelling of unsaturated porous media and resaturation of clay barriers*. Proc. Of Biot’s conf. Louvain la Neuve, Belgium. 1998.
- Peaceman, D. W., 1977. “Fundamentals of Numerical Reservoir Simulation“. *Developments in Petroleum Science*, 6. Elsevier.
- Rutqvist J., Börgesson L., Chijimatsu M., Nguyen T. S., Jing L., Noorishad J. and Tsang C.-F., *Coupled thermo-hydro-mechanical analysis of a heater test in fractured rock and bentonite at Kamaishi Mine – comparison of field results to*

- predictions of four finite element codes. Int. J. Rock mech. Min. Sci.* 38 (1), 129-142, 2001a.
- Rutqvist J., Börgesson L., Chijimatsu M., Kobayashi A., Nguyen T. S., Jing L., Noorishad J., and Tsang C.-F. *Thermohydromechanics of partially saturated geological media – governing equations and formulation of four finite element models. Int. J. Rock mech. Min. Sci.*, 38(19), 105-127, 2001b.
- Rutqvist J., Noorishad J. and Tsang C.-F. *Coupled Analysis of a Thermohydro-mechanical Experiment in Rock at Kamaishi Mine-Final Report. Swedish Nuclear Power Inspectorate (SKI) Technical Report 99:50. Also a Lawrence Berkeley National Laboratory Technical Report, LBNL-44203. p. 103. 1999.*
- Sugita, Y. and T. Fujita. *Experimental Results*, JNC TN8400 99-034. 1999.
- Suzuki H. and Fujita T., *Swelling characteristics of buffer material*, Japan Nuclear Cycle Development Institute, JNC TN8400 99-038. 1999. (in Japanese).
- Suzuki H., Chijimatsu M. and Fujita T., *Measurement of water movement under a thermal gradient and swelling pressure of buffer material*, Japan Nuclear Cycle Development Institute, JNC TN8400 99-020. 1999. (in Japanese).
- Verpeaux, P., A. Millard, T. Charras, A. Combescure. *A modern approach of large computer codes for structural analysis. Proc. SMIRT 10 Conf. Los Angeles, USA. 1989.*

www.ski.se

STATENS KÄRNKRAFTINSPEKTION
Swedish Nuclear Power Inspectorate

POST/POSTAL ADDRESS SE-106 58 Stockholm

BESÖK/OFFICE Klarabergsviadukten 90

TELEFON/TELEPHONE +46 (0)8 698 84 00

TELEFAX +46 (0)8 661 90 86

E-POST/E-MAIL ski@ski.se

WEBBPLATS/WEB SITE www.ski.se